e-ISSN: 2148-4171

11 volume 2 issue 2024 june

HITTITE JOURNAL OF SCIENCE AND ENGINEERING

HİTİT
ÜNİVERSİTESİ
YAYINLARI

HITTITE JOURNAL OF SCIENCE AND ENGINEERING

e-ISSN: 2148-4171
Volume: 11
June 2024
Issue 2

LANGUAGE OF PUBLICATION

English

CONTACT ADDRESS

Hitit Üniversitesi Mühendislik Fakültesi, ÇORUM, TÜRKİYE
Tel: 0090 364 2274533 Fax: 0090 364 2274533
hjse@hitit.edu.tr | https://www.hjse.hitit.edu.tr

PUBLISHER

Hitit University Press

EDITOR-IN-CHIEF

Ali KILIÇARSLAN, Prof. Dr.
Hitit University, TR

ASSOCIATE EDITORS

Dursun Ali KÖSE, Prof. Dr.
Hitit University, TR

Öncü AKYILDIZ, Assoc. Prof. Dr.
Hitit University, TR

SECTION EDITORS

Murat HOŞÖZ, Prof. Dr.
Kocaeli University, TR

Dursun Ali KÖSE, Prof. Dr.
Hitit University, TR

Kazım Savaş BAHÇECİ, Prof. Dr.
Hitit University, TR

Cengiz BAYKASOĞLU, Prof. Dr.
Hitit University, TR

Akif AKGÜL, Prof. Dr.
Hitit University, TR

Öncü AKYILDIZ, Assoc. Prof. Dr.
Hitit University, TR

BOARD OF EDITORS

Iftikhar AHMAD, Prof. Dr.
University of Malakand, PK

Mike BECKETT, Prof. Dr.
Bangor University, UK

İbrahim DİNÇER, Prof. Dr.
University of Ontario Institute of Technology, CA

Ali El KAMEL, Prof. Dr.
University of Waterloo, CA

Mohamad S QATU, Prof. Dr.
Eastern Michigan University, USA

Saffa RIFFAT, Prof. Dr.
University of Nottingham, UK

Thanos SALIFOGLOU, Prof. Dr.
Aristotle University of Thessaloniki, GR

Yuehong SU, Prof. Dr.
University of Nottingham, UK

Wojciech NOGALA, Dr.
Polish Academy of Sciences, POL

Yusuf AYVAZ, Prof. Dr.
Suleyman Demirel University, TR

Adil DENİZLİ, Prof. Dr.
Hacettepe University, TR

Ali GENCER, Prof. Dr.
Ankara University, TR

Metin GÜRÜ, Prof. Dr.
Gazi University, TR

Murat HOŞÖZ, Prof. Dr.
Kocaeli University, TR

Sadık KAKAÇ, Prof. Dr.
TOBB University of Economics and Technology, TR

Tarık Ömer OĞURTANI, Prof. Dr.
Middle East Technical University, TR

Ender SUVACI, Prof. Dr.
Eskişehir Technical University, TR

Ali TOPÇU, Prof. Dr.
Hacettepe University, TR

Kazım Savaş BAHÇECİ, Prof. Dr.
Hitit University, TR

Cengiz BAYKASOĞLU, Prof. Dr.
Hitit University, TR

Naki ÇOLAK, Prof. Dr.
Hitit University, TR

Vedat DENİZ, Prof. Dr.
Hitit University, TR

Hakan GÜNGÜNEŞ, Prof. Dr.
Hitit University, TR

Bülent KABAK, Prof. Dr.
Hitit University, TR

Ali KILIÇARSLAN, Prof. Dr.
Hitit University, TR

Dursun Ali KÖSE, Prof. Dr.
Hitit University, TR

İrfan KURTBAŞ, Prof. Dr.
Hitit University, TR

İbrahim SÖNMEZ, Prof. Dr.
Hitit University, TR

Seyfi ŞEVİK, Assoc. Prof. Dr.
Hitit University, TR

Dilber Esra YILDIZ, Prof. Dr.
Hitit University, TR

REFEREE BOARD

Hittite Journal of Science and Engineering uses a single-blind review. Referee names are kept strictly confidential.

Layout Editors

Ömer Faruk TOZLU, Res. Asst.
Hitit University, TR

Harun Emre KIRAN, Res. Asst.
Hitit University, TR

Hayati TÖRE, Res. Asst.
Hitit University, TR

LOCKSS: http://dergipark.org.tr/hjse/lockss-manifest

OAI: https://dergipark.org.tr/api/public/oai/hjse/?verb=ListRecords&metadataPrefix=oai_dc

Dear Readers,

After a very disciplined team work of HJSE and a rigorous refereeing process, the new issue of Hittite Journal of Science and Engineering (2024-Volume 11, Issue 2) was published. During publishing stages of this issue, HJSE Team and Hitit University Publishing Office worked together. I would like to express my gratitude to HJSE team members, Hitit University Publishing Office, all our authors and contributing reviewers of this issue.

As Editor in Chief, I also would like to thank to the President of Hitit University, Prof. Dr. Ali Osman Öztürk, for his support and interest in HJSE and to the Associate Editors of HJSE, namely Prof. Dr. Dursun Ali Kose and Assoc. Prof. Dr. Öncü Akyıldız and also the Section Editors of HJSE, namely Prof. Dr. Murat Hoşöz, Prof. Dr. Kazım Savaş Bahçeci, Prof. Dr. Cengiz Baykasoğlu and Prof. Dr. Akif Akgül as well as our Production Editors, Ömer Faruk Tozlu, Harun Emre Kıran and Hayati Töre for their invaluable efforts in making of the journal.

This new issue of Hittite Journal of Science and Engineering contains five papers from the engineering disciplines including mechanical engineering (3 papers), textile science and engineering and computer engineering. Most of the papers published in this issue is related to the applications of energy including heating, cooling, refrigeration and fluid mechanics. One of the other papers except the energy applications proposes a methodology for verification of contact pressure and pressure distribution via numeric and analytic methods to be used in wear calculations and the last paper is based on the preparation and successful application of unmodified lignin/water-based polyurethane (WPU) composite coating formulations. I believe that each article will contribute to the emergence of a rich literature on the subject.

I am pleased to invite researchers and scientists from all engineering disciplines to join us by submitting their best articles to be published in the Hittite Journal of Science and Engineering.

Dr. Ali Kılıçarslan

Editor-in-Chief

CONTENTS

HITTITE JOURNAL OF SCIENCE AND ENGINEERING

e-ISSN: 2148-4171
Volume: 11 • Number: 2
June 2024

Experimentally Performance Evaluation of a Dual Evaporator Ejector Refrigeration System with Diffuser Outlet Split Configuration under Varied Compressor Inlet Pressures

Gizem Çetin[1] | Ümit İşkan[3] | Mehmet Direk[2,*] | Mahmut Cüneyt Kahraman[2] |
Cüneyt Tunçkal[3]

[1]Yalova University, Graduate Studies Institute, Energy Systems Engineering Department, 77200, Yalova, Türkiye.
[2]Department of Energy System Engineering, Yalova University, 77200, Yalova, Türkiye.
[3]Department of Electric and Energy, Yalova University, 77200, Yalova, Türkiye.

Corresponding Author

Mehmet Direk
E-mail: mehmet.direk@yalova.edu.tr Phone: +0226 815 53 86
RORID: https://ror.org/01x18ax09

Article Information

Article Type: Research Article
Doi: https://doi.org/10.17350/HJSE19030000331
Received: 05.03.2024
Accepted: 05.04.2024
Published: 30.06.2024

Cite As

Direk M, et al. Experimentally Performance Evaluation of a Dual Evaporator Ejector Refrigeration System with Diffuser Outlet Split Configuration under Varied Compressor Inlet Pressures. Hittite J Sci Eng. 2024;11(2):49-56.

Peer Review: Evaluated by independent reviewers working in at least two different institutions appointed by the field editor.
Ethical Statement: Not available.
Plagiarism Checks: Yes - iThenticate
Conflict of Interest: Authors approve that to the best of their knowledge, there is not any conflict of interest or common interest with an institution/organization or a person that may affect the review process of the paper.

CRediT Author Statement
Gizem Çetin: Conceptualization, Methodology, Carrying out the Tests. **Ümit İşkan:** Investigation, Carrying out the Tests, Formal Analysis. **Mehmet Direk:** Supervision, Writing- review and editing. **Mahmut Cüneyt Kahraman:** Conceptualization, Visualization, Writing – Original Draft **Cüneyt Tunçkal:** Investigation, Carrying out the Tests, Formal Analysis

Experimentally Performance Evaluation of a Dual Evaporator Ejector Refrigeration System with Diffuser Outlet Split Configuration under Varied Compressor Inlet Pressures

Gizem Çetin[1] | Ümit İşkan[3] | Mehmet Direk[2,*] | Mahmut Cüneyt Kahraman[2] | Cüneyt Tunçkal[3]

[1]Yalova University, Graduate Studies Institute, Energy Systems Engineering Department, 77200, Yalova, Türkiye.
[2]Yalova University, Energy Systems Engineering Department, 77200 Yalova, Türkiye.
[3]Yalova University, Electric and Energy Department, 77200 Yalova, Türkiye.

Abstract

In this research, an experimental investigation was conducted on a dual-evaporator ejector system (DEES). The experiments were conducted under two distinct configurations, known as condenser outlet split (COS) and diffuser outlet split (DOS), across varying compressor inlet pres-sures. The system was initially operated in accordance with the COS configuration followed by operation under the DOS configuration. The comparison revealed a 9% reduction in the compressor work within the DOS configuration relative to the COS configuration. Evaporator#2 cooling capacity was 14% higher in the DOS compared to the COS. Moreover, the total cooling capacity achieved in the COS mode exhibited a 16% increase in comparison to the DOS mode. Furthermore, research findings indicate that by operating the DEES in the DOS configuration, full refrigerant separation can be achieved, leading to enhanced operational efficiency.

Keywords: Ejector, diffuser, dual evaporator, refrigeration system

INTRODUCTION

In recent years, research on the utilization of ejectors in refrigeration systems has seen a surge in interest due to their straightforward design, cost-effectiveness, and durability. By integrating ejectors, the efficiency of vapor compression refrigeration systems can be enhanced (1). Since the liquid-vapor separator, used in standard ejector refrigeration systems, has a maximum efficiency of 85%, it reduces the efficiency of the system. To mitigate these losses, researchers suggest replacing the separator with a second evaporator in vapor compression refrigeration systems employing ejectors (2) This modification not only enhances cooling capacity but also minimizes efficiency losses. Determining the separation of refrigerant in refrigeration systems with dual evaporators is crucial (3). Literature on systems with dual evaporators and an ejector typically recommends splitting the refrigerant flow at the condenser outlet to optimize performance (4). In dual evaporators (dual temperatures) refrigeration systems, it is observed that the ejector provides a beneficial impact on performance (5). Recent studies, such as Fan et al. (6), have investigated the performance of solar-assisted ejector compression heat pump cycles using R290/R600a refrigerants for water heating. These studies have demonstrated significant enhancements in coefficient of performance (COP) and heating capacity - up to 33% and 47%, respectively - compared to traditional vapor compression heat pump cycles. Śmierciew et al. (7) experimentally evaluated an ejector-based refrigeration system using isobutene. Their findings indicated that a higher quality at the nozzle inlet led to improved agreement between the proposed model's mass flow rates and the experimental data. Similarly, Tahir Erdinç et al., (8) evaluated the performance of an ejector heat pump system. They found a 22.6% increase in COP with ejector utilization. Çalışkan and Ersoy (9) found that incorporating an ejector in a dual evaporator CO2 system increases the COP value by up to 47%. In the investigation conducted by Işkan et al. (10), the comparative analysis of the performance of R134a and the alternative refrigerant R516A within a DEES was examined. The experimental results revealed that R134a exhibited superior cooling capacity compared to R516A, leading to an elevation in the COP ranging between 1% and 5% when R134a was adopted in the system. Furthermore, it was deduced that there existed a positive correlation between the performance parameters and increasing air velocities. However, air velocities exceeding 2.2 m/s exhibited a diminishing effect on system performance. Vaibhav Jain et al. (4) conducted an analysis on a DEES operating under the COS configuration whereby varying condenser water temperatures were employed. Their study revealed an escalating trend in the entrainment ratio, rising from 0.396 to 0.701 as the condenser water temperature decreased. In a separate study, Fingas et al. (11) performed an experimental assessment on the efficiency of an ejector within a bi-evaporator ejector heat pump system utilizing R290 as the refrigerant, with experiments being conducted according to the COS mode. The results of their investigations indicated a notable enhancement in the heating COP of the system by up to 38% when compared to a direct expansion system. Ünal et al. (12) examined the performance of R1234yf, R1234ze(E), and R600a refrigerants in a DEES refrigeration system. It was observed that the type of refrigerant had a significant effect on the size of the ejector. In the COS configuration, the refrigerant undergoes division prior to its arrival at the ejector. This partitioning serves to diminish the quantity of refrigerant that enters the primary inlet of the ejector. With a reduction in mass flow rate at the primary inlet of the ejector, there is a corresponding decline in the velocity increase. Lower refrigerant velocity leads to a reduction in mass flow rate at the ejector outlet. An alternative approach to address this issue involves separating the refrigerant after the diffuser outlet, as proposed by Lawrance and Elbel (13). By implementing this separation, all refrigerant leaving the condenser is directed to the primary inlet of the ejector, with the objective of elevating the rate of velocity enhancement resulting from the pressure drop. Consequently, the strategy entails the operation of a system featuring dual evaporators, wherein the refrigerant is divided into two streams subsequent to the diffuser outlet and distributed to the first and second evaporators. This approach is designed to optimize the efficiency of the ejector system.

Prior research has primarily focused on the COS configuration, while theoretical investigations on the DOS layout have been limited. To address this research gap, the present study examines the performance of DEES operating in both COS and DOS configurations. Experimental tests were conducted using R134a as the refrigerant, with results compared through graphical analysis. The experiments were repeated at varying compressor inlet pressures to evaluate the influence of compressor inlet pressure on system performance.

EXPERIMENTAL SETUP

The experimental setup has been implemented in two distinct configurations, namely the condenser outlet split (COS) and diffuser outlet split (DOS). The evaporators within the system have been positioned according to the DOS and COS configurations. The system incorporates two plate heat exchangers identified as Evaporator#1 and Evaporator#2, in addition to a tubular welded heat exchanger denoted as Evaporator#3. Moreover, there is integration of a hermetic type compressor, condenser, ejector, and various auxiliary components. As illustrated in Figure 1, the experimental setup comprises a single refrigeration cycle along with two water cycles. The water utilized in Evaporator#1 and Evaporator#2 functions to initiate the evaporation of the refrigerant. Within the water cycles, pumps have been installed to elevate the water pressure within the tanks. In the DOS configuration, the separator component positioned downstream of the ejector has been employed to segregate the refrigerant into dual streams. The connection between all elements within the system has been established through insulated copper piping. The COS configuration encompasses evaporators, with the schematic representation of the refrigerant flow paths elucidated in Figure 1a. Similarly, the DOS configuration entails evaporators, with a visual depiction of the refrigerant pathways demonstrated in Figure 1b. Subsequent to this, Figure 2 indicates the complete experimental setup, whereas Figure 3a illustrates the configuration of the ejector and the subsequent separation process. Additionally, Figure 3b showcases the position of the evaporators in the DOS mode. The designated points in Fig. 1 and Fig. 2 are introduced in Table 1.

Table 1 The designated points in Fig. 1 and Fig. 2

No	COS / DOS configurations
1	Inlet of compressor
2	Outlet of compressor
3	Outlet of condenser
4	Inlet of ejector/Outlet of ejector's nozzle
5	Second inlet of ejector/ Suction chambers of ejector
6	Mixing chamber
7	Inlet of evaporator#3/ Inlet of evaporator#1
8	Outlet of evaporator#3/ Outlet of evaporator#1
9	Outlet of diffuser

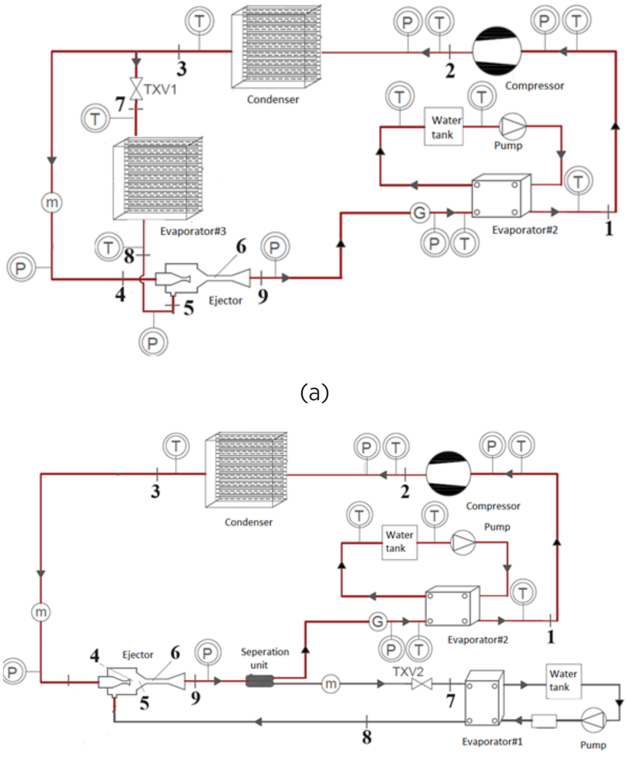

(a)

(b)

Figure 1 a) COS and b) DOS configurations flow diagram

In the DOS configuration, the refrigerant from the condenser is directed to the primary inlet of the ejector. Upon entry at the first inlet of the ejector, the fluid undergoes an increase in velocity as a result of nozzle constriction, leading to a pressure reduction and subsequent intake into the suction chamber of the ejector. Subsequently, the refrigerant passing through the TXV undergoes isenthalpic throttling at the ejector outlet. This process culminates in a pressure reduction prior to the entry into evaporator#1, initiating the initial stage of evaporation within evaporator#1. The refrigerant is then sucked into the secondary inlet of the ejector under a vacuum, where it commingles with the refrigerant from the primary inlet. Subsequently, the blended streams within the suction chamber are propelled into the mixing chamber under consistent pressure. As the refrigerant, existing in a liquid-gas phase with elevated velocity, decelerates within the divergent diffuser, the pressure is boosted owing to the diverging geometry of the diffuser. The refrigerant, present in the liquid-gas phase upon exiting the diffuser, fully transitions into the gaseous phase within evaporator#2. It subsequently proceeds into the compressor for pressurization, before being routed to the condenser, thereby concluding the operational cycle.

Figure 2 Experimental setup and measurement devices

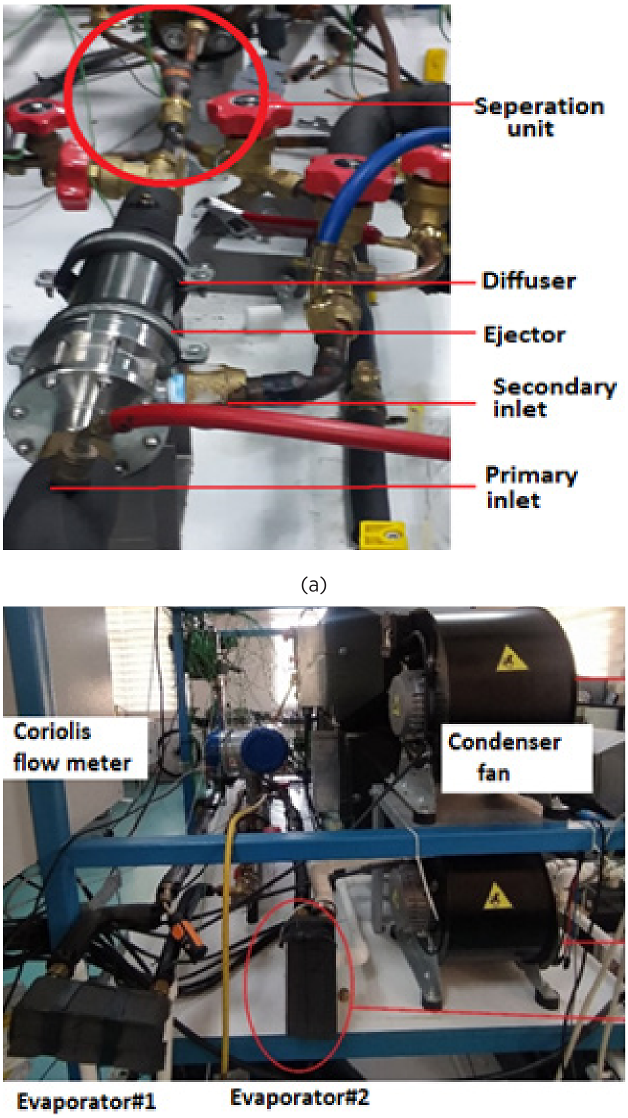

(a)

(b)

Figure 3 a) Diffusor and separation process b) The position of the evaporators in the DOS mode

Thermodynamic Equations and Diagrams

Figure 4 illustrates the pressure-enthalpy (P-h) diagrams for the DOS and COS configurations. Equations have been derived based on designated points and are provided in Table 2.

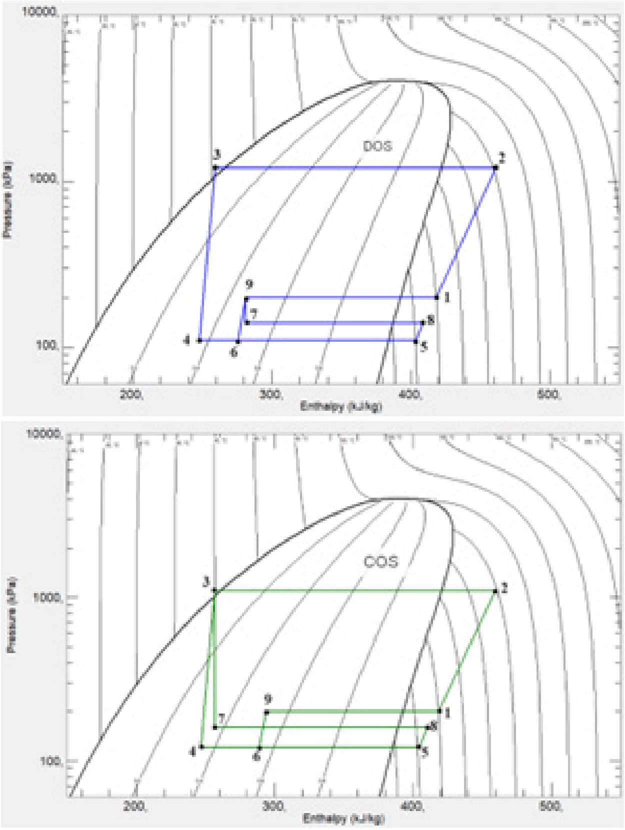

Figure 4 P-h diagrams of DOS and COS configurations

Table 2 Thermodynamic Equations

	COS	DOS
Compressor power	$\dot{W}_{comp} = (h_2 - h_1).\dot{m}_1$	$\dot{W}_{comp} = (h_2 - h_1).\dot{m}_{total}$
Condenser capacity	$\dot{Q}_{cond} = (h_2 - h_3).\dot{m}_1$	$\dot{Q}_{cond} = (h_2 - h_3).\dot{m}_{total}$
Evaporator#1 cooling capacity	$\dot{Q}_{evap\#1} = (h_2 - h_3).\dot{m}_1$	-
Mass flow rate	$\dot{m}_{total} = (\dot{m}_1 + \dot{m}_2)$	$\dot{m}_{total} = (\dot{m}_1 + \dot{m}_2)$
Evaporator#2 cooling capacity (water)	$\dot{Q}_{evap\#2(water)} = \dot{m}_{water}.c_{p(water)}.\Delta T$	$\dot{Q}_{evap\#2(water)} = \dot{m}_{water}.c_{p(water)}.\Delta T$
Evaporator#3 cooling capacity	-	$\dot{Q}_{evap\#3} = (h_8 - h_7).\dot{m}_2$
H evap1 inlet	$h_9 = h_7$	-
H evap2 inlet	$h_9 = h_1 - (\dot{Q}_{evap\#2(water)} / \dot{m}_1)$	$h_9 = h_1 - (\dot{Q}_{evap\#2(water)} / \dot{m}_1)$
H evap3 inlet	-	$h_3 = h_7$
Total cooling capacity	$\dot{Q}_{total} = \dot{Q}_{evap\#1} + \dot{Q}_{evap\#2}$	$\dot{Q}_{total} = \dot{Q}_{evap\#1} + \dot{Q}_{evap\#2}$

The setup utilizes two distinct types of flow meters: a turbine-type flow meter installed at the outlet of the condenser, and a Coriolis-type flow meter installed between evaporator#1 and the separation unit at the diffuser outlet. In conventional ejector refrigeration cycles, a distinct separator is employed for the separation of liquid and vapor phases. However, in this particular system, the task of liquid-vapor separation is undertaken by the second evaporator. As depicted in Figure 1b, the refrigerant pathways and system components are delineated during the operation of the ejector refrigeration system in the DOS configuration. Furthermore, Table 3 details the specifications of the experimental equipment, while Table 4 outlines the specifications of the measurement devices utilized.

Table 3 The component characteristics of experimental setup

Component	Type	Characteristics
Evaporator#1	Air	Heat Transfer Coefficient: 52 Wm^2K^{-1}, Sensible Heat Rate: 1
Evaporator#2	Water	Heat transfer surface: 0,5m^2 # of plate: 24
Evaporator#3	Water	Heat transfer surface: 0,216m^2 , # of plate 50
Compressor	Hermetic, variable speed drive	Danfoss MTZ 022-4 b 2.9 kW, 380-400 V, 50 Hz, 2900 rpm
TXV 1-2	Externally equalized	

Table 4 Specifications of the measurement devices utilized in experimental setup

Parameters	Component	Accuracy	Measurement Range
Temperature	K-type thermocouple	± % 0.8	-100 – 1370 ºC
Pressure	Electromagnetic manifold	± % 0.5	-1 – 60 bar
Pressure	Pressure transmitter	± % 0.5	4 – 20 mA
Pressure	Bourdon manometer	± % 0.5	-1 – 55 bar
Air Velocity	Anemometer	± % 2	0 – 30 m s^{-1}
Water volumetric flow rate	Electromagnetic flowmeter	± % 0.3	0 – 1 m^3s^{-1}
Refrigerant mass flow rate	Coriolis mass flow rate	± % 0.1	0 – 5 kg m s^{-1}
Compressor Frequency	Frequency inverter	± % 0.2	10-50 Hz

Throughout the experiment, certain parameters were held constant, including the compressor inlet pressure, water inlet temperature, condenser air velocity, and compressor frequency. The specific values of these parameters are delineated in Table 5.

Table 5 Constant values of test while varying the compressor inlet pressures

Compressor inlet pressure (kPa)	170 – 230 (by 10 kPa steps)
Evaporator#2 – water inlet temperature (°C)	20-21
Evaporator#1 -air inlet temperature(°C)	25-26
Evaporator#2 water mass flow rate (kg/s)	0,2
Compressor frequency (Hz)	50

RESULTS AND DISCUSSIONS

This section examines the results achieved during the operation of the system in both COS and DOS configurations, while varying the compressor inlet pressures. Pressure and temperature values obtained from the experiments are presented in Table 6. An examination of Table 6 reveals higher compressor outlet pressure and condenser outlet temperatures in the DOS configuration compared to the COS configuration.

Figure 5 illustrates the changes in compressor compression ratios while varying compressor inlet pressures. The analysis of Figure 5 reveals a negative correlation between compression ratios and increasing compressor inlet pressures. Through experimental observations, it was noted that the compression ratios for both configurations exhibited a decrease of approximately 20% as the compressor inlet pressures increased from 170 kPa to 230 kPa. This trend can be attributed to the maintenance of consistent condensing temperatures as the compressor inlet pressures elevate. Consequently, the compression ratio exhibited an inversely proportional relationship with the compressor inlet pressure due to the constant nature of condenser water temperature and condensing pressure.

Furthermore, the compression ratio was found to be higher in the DOS configuration compared to the COS configuration. Specifically, at a compressor inlet pressure of 190 kPa, the compression ratio was calculated to be 4.13 for COS and 5.03 for DOS configuration, indicating a 22% increase. This disparity was linked to varying refrigerant mass flow rates in the two configurations. The DOS configuration, characterized by lower mass flow rates, yielded a higher compression ratio compared to the COS configuration. Even the total refrigerant volume remained constant in both configurations, a greater mass flow rate of refrigerant passed through the compressor in the COS configuration. This discrepancy stemmed from the separation of refrigerant leaving the ejector in DOS configuration, where some refrigerant was directed to evaporator #1.

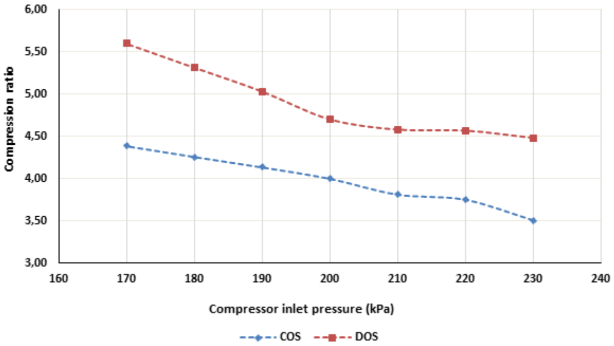

Figure 5 The change of compression ratio depending on compressor inlet pressure

yielded lower compressor power values compared to the COS configuration. For instance, at a compressor inlet pressure of 180 kPa, the calculated compressor power was 0.57 kW for COS and 0.52 kW for DOS, marking a 9% reduction. Upon an assessment of Figures 5 and 6, it is apparent that decreasing compressor inlet pressures resulted in higher

Table 6 Experimental results for DOS and COS configurations

Compressor inlet pressure (kPa)	Configuration	Compressor outlet pressure (kPa)	Condenser outlet temperature (ºC)	Evaporator#2 outlet temperature (ºC)
170	DOS	985	27.9	25.1
	COS	779	26.4	22
180	DOS	967	29.4	25.1
	COS	786	26.6	22.2
190	DOS	986	31.1	25
	COS	793	26.7	22
200	DOS	940	33.2	24
	COS	800	26.7	22.1
210	DOS	943	34.3	26
	COS	812	26.2	22.1
220	DOS	1001	36.5	24.9
	COS	829	26.6	22
230	DOS	1008	36.3	24.6
	COS	800	29	22.2

compression ratios but lower compressor power values in the DOS configuration. This phenomenon indicates that the DOS configuration achieved elevated condenser temperatures with reduced compressor power values. This feature can be leveraged for greater heating capacity when the system operates as a heat pump, as the DOS system functions at elevated condenser water temperatures while consuming lower compressor power values.

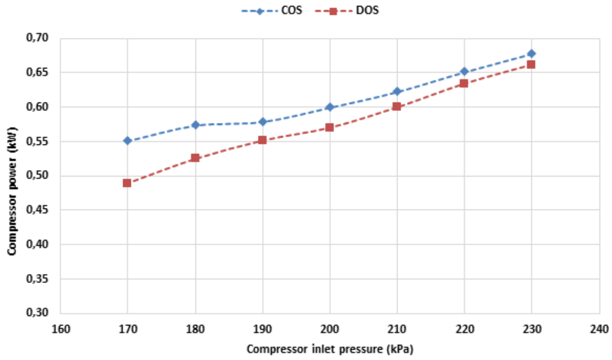

Figure 6 The change of compressor work depending on compressor inlet pressure

Figure 7 illustrates the variations in cooling capacity of evaporator#2 in relation to the compressor inlet pressure. The data presented in Figure 7 indicates that the DOS configuration exhibited higher cooling capacity for evaporator#2 compared to the COS configuration. For instance, at a compressor inlet pressure of 180 kPa, the cooling capacity for evaporator#2 was measured at 0.59 kW for COS and 0.67 kW for DOS, showcasing a 14% increase.

The enhanced cooling capacity in the DOS configuration can be attributed to the lower quality of the refrigerant leaving the ejector. In the DOS configuration, due to the ejector (diffuser) outlet split, the refrigerant enters both evaporators with an equivalent quality, resulting in a notable boost in the cooling capacity of evaporator#2. Conversely, in the COS configuration, the degree of quality at the inlet of evaporator#2 is primarily influenced by the separation rates of the refrigerant following condenser (14).

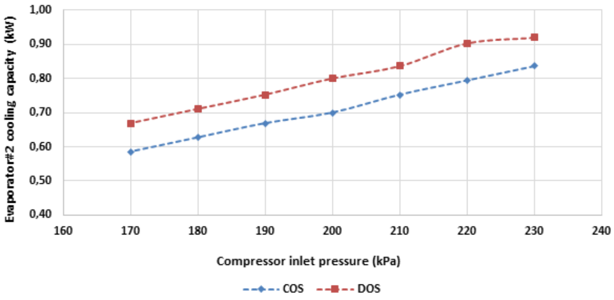

Figure 7 The change of evaporator#2 cooling capacity depending on compressor inlet pressure

Figure 8 illustrates the variations in cooling capacity of evaporator #1 (Qevap#1) in relation to compressor inlet pressures. In COS configuration, the refrigerant fluid underwent splitting at the condenser outlet, resulting in higher measured mass flow rates in comparison to that observed in DOS configuration. Consequently, the Qevap#1 value exhibited an elevation in COS configuration owing to the increased mass flow rates. Notably, at a compressor inlet pressure of 220 kPa, Qevap#1 was recorded as 0.49 kW and 0.19 kW in COS and DOS modes, respectively. It was observed that mass flow rates were lower in DOS mode, primarily attributed to the reduced pressure of mixture within suction chamber of the ejector, consequently resulting in diminished quantities of entrained refrigerant.

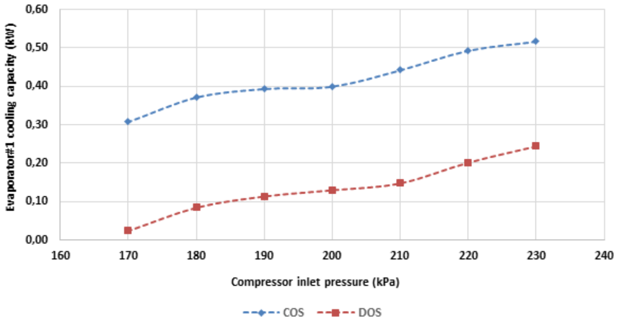

Figure 8 The change of evaporator#1 cooling capacity depending on compressor inlet pressure

Figure 9 depicts the variations in evaporator#2 superheat degrees with respect to compressor inlet pressures. The data reveals a downward trend in evaporator#2 superheat values for both configurations as compressor inlet pressures rise. Additionally, the superheat degrees recorded in DOS configuration were consistently lower than those in the COS configuration. This observation aligns with the previously established higher cooling capacity of evaporator#2 (Figure 7) in the DOS configuration compared to COS. The lower superheat degrees affirm that the refrigerant entering evaporator#2 in the DOS configuration maintained a lower quality, highlighting the performance advantages associated with this system configuration. Furthermore, examination of the figure revealed that the superheat degree of evaporator #2 in the COS configuration ranged between 29°C and 35°C. These values are consistent with those reported in the study by İşkan and Direk (15).

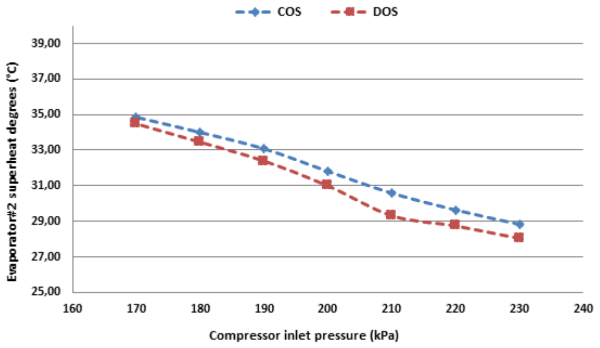

Figure 9 The change of evaporator#2 superheat value depending on compressor inlet pressure

Figure 10 illustrates the variations in total cooling capacity relative to compressor inlet pressures. Upon analysis, it becomes apparent that the COS configuration achieved a higher total cooling capacity at the specified pressures compared to the DOS configuration. This disparity can be attributed to the lower energy difference per unit mass of refrigerant at the evaporators in the COS configuration as opposed to the DOS configuration. For instance, at a pressure of 230 kPa, the DOS configuration provided a total cooling capacity of 1.16 kW, while the COS configuration delivered a total cooling capacity of 1.35 kW, presenting a 16% increase. Similar patterns are observed at other inlet pressures, reinforcing the trend of higher total cooling capacity in the COS mode.

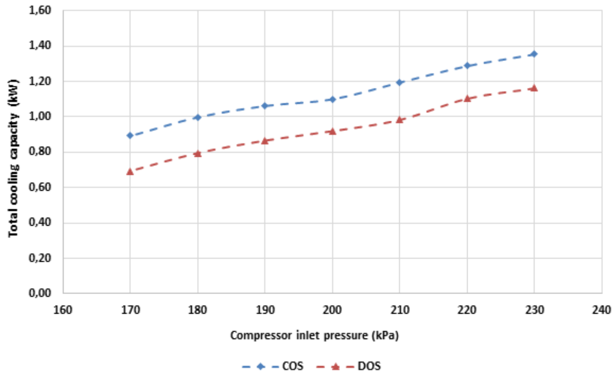

Figure 10 The change of total cooling capacity depending on compressor inlet pressure

CONCLUSION

This study presents an experimental comparison of the performance of an ejector refrigeration system operating in COS and DOS configurations under varying compressor inlet pressures. The experimental investigation yielded significant findings, as outlined below:

-The DOS configuration demonstrated a higher compression ratio than the COS configuration when operating at lower mass flow rates.

-Compressor power was observed to be 9% lower in the DOS configuration compared to the COS configuration.

-Evaporator#2 cooling capacity was approximately 14% higher in the DOS configuration compared to the COS configuration across different compressor inlet pressures.

-Notably, the COS configuration exhibited approximately 16% higher total cooling capacity than the DOS configuration at varying compressor inlet pressures.

These results highlighted the operational efficiency and refrigerant separation capabilities of the dual evaporator ejector system when operated in the DOS configuration. A key recommendation for future research involves the implementation of a constant area ejector model in the DOS configuration, as this adjustment has the potential to alleviate issues related to inadequate cooling due to low ER at decreased compressor inlet pressures.

Acknowledgment

We are grateful to Yalova University due to financial support (Project no: 2022/AP/0010 and 2023/YL/0002)

References

1. Ünal Ş, Cihan E, Erdinç MT, Bilgili M. Influence of mixing section inlet and diffuser outlet velocities on the performance of ejector-expansion refrigeration system using zeotropic mixture. Therm Sci Eng Prog. 2022 Aug 1;33:101338.
2. Kim S, Jeon Y, Chung HJ, Kim Y. Performance optimization of an R410A air-conditioner with a dual evaporator ejector cycle based on cooling seasonal performance factor. Appl Therm Eng. 2018 Feb 25;131:988–97.
3. Üğüdür B, İşkan Ü, Direk M. Performance analysis of dual-evaporator ejector refrigeration system in different

configurations: Experimental investigation. Int J Energy Stud. 2023 Sep 22;8(3):315–30.

4. Jain V, Khurana S, Parinam A, Sachdeva G, Goel A, Mudgil K. Experimental analysis of an ejector assisted dual-evaporator vapor compression system. Energy Convers Manag. 2024 Jan 15;300:117966.
5. Liang Y, Ye K, Zhu Y, Lu J. Thermodynamic analysis of two-stage and dual-temperature ejector refrigeration cycles driven by the waste heat of exhaust gas. Energy. 2023 Sep 1;278:127862.
6. Fan C, Yan G, Yu J. Thermodynamic analysis of a modified solar assisted ejector-compression heat pump cycle with zeotropic mixture R290/R600a. Appl Therm Eng. 2019 Mar 5;150:42–9.
7. Śmierciew K, Dudar A, Butrymowicz D, Gagan J, Jakończuk P, Zou H. Experimental Assessment of the Efficiency of Two-Phase Ejector Components for Isobutane. Sustainability. 2022 Jan;14(20):13356.
8. Tahir Erdinc M, Kutlu C, Unal S, Aydin O, Su Y, Riffat S. Performance improvement potential of a PV/T integrated dual-source heat pump unit with a pressure booster ejector. Therm Sci Eng Prog. 2023 Jan 1;37:101534.
9. Caliskan O, Ersoy HK. Energy analysis and performance comparison of transcritical CO2 supermarket refrigeration cycles. J Supercrit Fluids. 2022 Oct 1;189:105698.
10. İşkan Ü, Kahraman MC, Direk M. Comparison of R134a and R516A's Performance at Different Air Velocities in Two Evaporator Ejector Cooling System. Hittite J Sci Eng. 2023 Mar 31;10(1):69–76.
11. Fingas R, Haida M, Smolka J, Besagni G, Bodys J, Palacz M, et al. Experimental analysis of the air-to-water ejector-based R290 heat pump system for domestic application. Appl Therm Eng. 2024 Jan 10;236:121800.
12. Ünal Ş, Erdinç MT, Akgün H, Bilgili M. Effects of alternative refrigerants on the ejector dimensions for single and dual ejectors enhanced bus air conditioning system. Int Commun Heat Mass Transf. 2023 Apr 1;143:106685.
13. Lawrence N, Elbel S. Experimental and Analytical Investigation of Automotive Ejector Air-Conditioning Cycles Using Low-Pressure Refrigerants. Int Refrig Air Cond Conf [Internet]. 2012 Jan 1; Available from: https://docs.lib.purdue.edu/iracc/1169
14. Direk M, İşkan Ü, Tunçkal C, Mert MS, Yüksel F. An experimental investigation of ejector employed a dual-evaporator vapor compression refrigeration system under various entrainment ratios using R134a as the refrigerant. Sustain Energy Technol Assess. 2022 Aug 1;52:102293.
15. İşkan Ü, Direk M. Experimental performance evaluation of the dual-evaporator ejector refrigeration system using environmentally friendly refrigerants of R1234ze(E), ND, R515a, R456a, and R516a as a replacement for R134a. J Clean Prod. 2022 Jun 10;352:131612.

HITTITE JOURNAL OF SCIENCE AND ENGINEERING

e-ISSN: 2148-4171
Volume: 11 • Number: 2
June 2024

Sensitivity Analysis of Wear on Metal-On-Metal Bearing Couples via Verification of Numeric and Analytic Methods

Alican Tuncay Alpkaya | Senay Mihcin

Department of Mechanical Engineering, İzmir Institute of Technology, 35433, İzmir, Türkiye.

Corresponding Author

Senay Mihcin
E-mail: senaymihcin@iyte.edu.tr Phone: +00 (232) 750 67 07
RORID: https://ror.org/03stptj97

Article Information

Article Type: Research Article
Doi: https://doi.org/10.17350/10.17350/HJSE19030000332
Received: 19.01.2024
Accepted: 07.05.2024
Published: 30.06.2024

Cite As

Alpkaya AT, Mihcin S. Sensitivity Analysis of Wear on Metal-On-Metal Bearing Couples via Verification of Numeric and Analytic Methods. Hittite J Sci Eng. 2024;11(2):57-67.

Peer Review: Evaluated by independent reviewers working in at least two different institutions appointed by the field editor.
Ethical Statement: Not available.
Plagiarism Checks: Yes - iThenticate
Conflict of Interest: Authors approve that to the best of their knowledge, there is not any conflict of interest or common interest with an institution/organization or a person that may affect this study.

CRediT Author Statement:
Alican Tuncay Alpkaya: Author: Conceptualization, Methodology, Software, Validation, Writing- original draft. **Senay Mihcin:** Author: Data curation, Visualization, Investigation, Validation, Supervision, Writing-review and editing.

Sensitivity Analysis of Wear On Metal-On-Metal Bearing Couples Via Verification of Numeric and Analytic Methods

Alican Tuncay Alpkaya | Senay Mihcin*

Department of Mechanical Engineering, İzmir Institute of Technology, 35433, İzmir, Türkiye.

Abstract

Wear mechanism is important since it leads to revisions in Total Hip Replacement (THR) surgeries. Contact pressure plays an important role in wear mechanisms and needs to be investigated in detail to obtain more accurate wear predictions to understand the wear performance of the implant in the design stage. This study proposes a methodology for verification of contact pressure and pressure distribution via numeric and analytic methods to be used in wear calculations. Based on Hertz's contact theory, the contact pressure and the contact area are calculated in the analytical method. The results are compared to the numeric method's results obtained from the finite element method. The linear and volumetric wear rates of bearing couples' surfaces were estimated by Archard's wear equation. The effect of design parameters on pressure such as head radius, cup thickness, material combination of bearing couples, coating film material, and film thickness are investigated in this study using the proposed methodology. The minimum error between the analytical and numerical results was 0.24% for 28 mm of head diameter, while the maximum error was 11.79 % for 48- mm of head diameter. The minimum contact pressure values were obtained from 48- mm of head radius at a half contact angle of 190 (degrees) in FEM and Hertz calculations, respectively. The maximum linear wear rate was calculated at 0.0026 mm/Mc at a 1- mm cup thickness, while minimum linear wear rate was 0.0022 mm/Mc at a 10- mm cup thickness in the numeric method. The maximum survival cycles of coating materials rate were 31847 cycles for the Stainless-steel coated cup with 500 µm of coating thickness, while the minimum cycles was 2359 cycles for the Ti64 coated cup surface with 100 µm of coating thickness. It is concluded that the most important design parameters are the cup thickness and the material combinations since they have a significant effect on the contact pressure and the contact area. This study provides a verification methodology for the parametric sensitivity analysis before experimental validations. The methodology utilized in this study could be utilized by designers while optimizing the design parameters to minimize the wear.

Keywords: Hertz contact theory, Archard's wear law, linear and volumetric wear rates, finite element analysis, parametric design of hip implants

INTRODUCTION

Total Joint Replacement (TJR) applications started with Sir John Charney in 1958, using metal-on-polymer implants for hip joints (1). Polytetrafluoroethylene (PTFE) was chosen as the acetabular cup material and stainless steel was used as the femoral head material. However, this bearing combination produced excessive wear of PTFE, resulting in a lifespan of two-years (2). This problem led to the research for more durable bearing combinations so that the first metal-on-metal (MoM) bearing couple was introduced by Haboush (US), McKee, and Watson-Farrar (UK) in 1951 (3). Since then, metal-on-metal (MoM) bearing couple has been in use frequently in hip implant applications, due to their outstanding mechanical properties such as higher corrosion resistance, toughness, strength, ease of machinability, cost-effectiveness, and lower surface roughness (4,5). Although the volumetric wear rate of metals in million cycles is higher than that of ceramic materials, the wear rates of ceramics in long term might induce osteolysis (6).

According to the results of National Joint Registry (NJR) (7), 1,091,892 total hip replacements have been performed in the UK, out of which resulted in 31,410 (2.9%) first revision surgeries. These first revision surgeries were due to aseptic loosening, (7,644) adverse soft tissue reaction to debris (5,114), dislocation/subluxation (5,383), pain (4,705), and infection (4,555). To avoid high levels of debris, reduction of coefficient of friction was aimed for longer-lasting joints. To overcome these encountered revision problems, the coating of the bearing surfaces was considered. Thin film coatings on bearing surfaces were investigated for the effects of contact pressure, wear rate, and damage (7). Reinforced hydroxyapatite (HA) coating was used over titanium alloy for orthopedic applications using the plasma spraying technique (7). The HA-based coating film thickness was approximately 100-125 um demonstrating enhanced mechanical properties of wear and corrosion resistance, and bioactivity (7). However, so far there has been no consensus over the optimum film thickness parameters.

Ceramic on ceramic bearing couple contact mechanics of hip implants has been investigated for the effects of changing the head diameter, radial clearance, and loading magnitude (8,9). In another study, the effects of changing the stem geometries and the neck length on wear estimation of the bearing surfaces were investigated in MoM(10,11). Similarly, the contact mechanics of hard-on-hard bearing couples in THR have been investigated in the literature However, in these studies, only a small range of parameters was covered for the investigation of head diameter, clearance, and material combination of ceramics on ceramics, and coating materials were chosen as ceramics (8–13). Previously, the researchers have studied the optimization of design parameters and the material selection for hip implants (14–16). Although there are many studies on investigating the effect of changing the clearance, loading values, and head radius of THR in literature (8–13,17), the parameters of cup thickness for MoM hip implants, coating material, and its thickness, and also material combinations of head-on-cup bearing couple thickness have not been investigated so far in this level. Since computational methods could be costly, it is very important to provide a verification method before moving on to the simulator simulations where experimental validations are compared against the computational results.

Hertz's contact theory (18) is chosen as the analytical model to be utilized for the contact pressure calculations in the prototypes. This theory is mostly used in calculating the contact pressure values, especially on spherical contact surface models. In this study, contact pressure, pressure distribution, and contact area of all bearing prototypes are calculated by using both analytical and numerical methods. An analytical method makes use of the mathematical equations to predict the contact pressure and its distribution, while the numerical method makes use of the Finite Element Modelling (FEM) technique. The comparison of these two methods and their errors are calculated by changing the design parameters of MoM-bearing couples. These results were used for predicting the linear and volumetric wear rates of bearing surfaces. Estimating the linear and volumetric wear rates could lead the way to calculate the lifespan of hip implants. Since the wear rate has direct effect on overall longevity of hip prosthesis, to quantify this effect, Archard wear equation is utilized to calculate the linear and volumetric wear rates based on the previous empirical relations of the bearing surfaces (19–21). Then, these results are compared with the literature data to enhance the reliability of our study. Consequently, this study provides a broader view for the effects of different design parameters on contact mechanics and wear rates of MoM hip implants.

MATERIAL AND METHODS

To understand the effect of parameters on the wear mechanism, a sensitivity analysis is required. The parameters chosen for the sensitivity analysis in this study are as follows: head diameters, cup thicknesses, material combinations, coating materials, and coating thicknesses. Since the wear rate has a direct effect on the overall lifespan of the prosthesis, to quantify these effects, Archard wear equation is utilized to calculate linear and volumetric wear rates based on the previous empirical relations of bearing surfaces (22). The comprehensive investigation of these parameters affecting the contact pressure and its distribution are head radius, cup thickness, material combinations, coating material, and its thickness, respectively. The maximum hip joint contact force in terms of body weight (BW) % during a gait cycle was determined as 368±78 %- BW (23). The hip contact force of a 70-kg person is approximately 2500 N. Therefore, the nominal load of 2500 N is applied at the center of the femoral head, which is approximately 3.5 times the body weight of a 70-kg per person in all prototypes (24). This load is selected as the maximum hip contact force during normal gait cycles (25). Then, the obtained results were compared to the numeric method used by the finite element method.

Analytical Methods

The load *(P)* is calculated by multiplying the contact area relating to the contact radius (a_h) with the contact pressure *(p)* in Eq. 1.

$$P = \pi {a_h}^2 p \qquad (1)$$

Equivalent modulus E is replaced by E' as following Eq. 2

$$1/E' \; = \; (1 - {\upsilon_h}^2)/E \; + (1 - {\upsilon_c}^2)/E_c \qquad (2)$$

In this equation υ_h is the head material's Poisson ratio and υ_c is the cup material's Poisson ratio, E_h is the elastic moduli of the head material and E_c is the cup material elastic moduli. The equivalent ball radii (R_{eq}) are related to the head (R_h) and the cup (R_c) surfaces. The equivalent ball radius is determined by Eq. 3:

$$R_{eq} = (R_c \, R_h)/c \qquad (3)$$

where, R_c is a cup radius, R_h is the femoral head radius and c is the radial clearance (Figure 1a). The half contact radius a_h between the head and the cup is calculated by Eq. 4:

$$a_h = (3PR_{eq} \frac{(1 - {\upsilon_h}^2)\mathrm{Ec} + (1 - {\upsilon_c}^2)\mathrm{Eh}}{E_h E_c})^{\frac{1}{3}} \qquad (4)$$

At the same material combination, we can simplify Eq. 5:

$${a_h}^3 = (3PR_{eq}(1 - \upsilon^2)/2E) = 0.75(PR_{eq}/E') \qquad (5)$$

The maximum contact pressure in Eq. 1 can be simplified in terms of contact radius and load in Eq. 6:

$$p_{max} = (3\mathrm{P}/2\pi {a_h}^2) \qquad (6)$$

And the formula based on the horizontal distance (x) for the calculation of the pressure distribution from the contact center is given in Eq. 7:

$$p = p_{max} \, [1 - (\frac{x}{a_h})^2 \,]^{1/2} \qquad (7)$$

The horizontal distance (x) and the contact radius (a_h) are transformed into the polar coordinate system. In the numerical calculations, x values in the Cartesian coordinate are found using the probe command in ANSYS/Workbench over the acetabular cup surface while the contact half-angle and the angle values are calculated by using the transformation of the horizontal axis (x) and the contact radius into the polar coordinate.

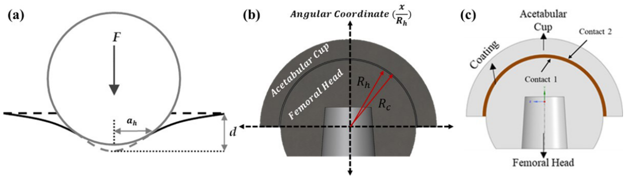

Figure 1 Schematic illustrations of (a) half angle of contact mechanics, (b) uncoated and (c) coated prototypes of the ball-in-socket model.

Numerical Methods

The Finite Element Model (FEM) prototypes are performed as a static model under a constant load of 2500N varying the effect of some parameters such as cup thickness, femoral head radius, material combinations, coating film material combinations and thickness. To understand the effects of contact pressure and pressure distribution on the wear rates in MoM-bearing couples, the sensitivity analysis was performed. Therefore, two different prototypes were modeled and named as coated and uncoated prototypes. The femoral head had a diameter of 36 mm while the clearance between the femoral head and acetabular cup was 50 µm. The acetabular cup thickness was kept constant at 5 mm to minimize the additional effects on contact pressure (8). Additionally, coated prototypes had three different coating thicknesses such as 100, 250, and 500 µm. These prototypes were meshed with Solid186 (26), a quadratic element type with 20 nodes per unit element (27), and each node having 3 different degrees of freedom in ANSYS Inc. 2021

R2 (Canonsburg, PA, USA). The mesh convergence test was performed to determine the number of elements that affect the results of the system analysis the least. For this purpose, the investigated value (contact pressure) was controlled by increasing the number of elements. The prototype with 1-mm mesh size had 42978 elements, 160180 nodes, and 1856 contact elements while the prototype with 2-mm mesh size had 7881 elements, 26890 nodes and 594 contact elements. The detailed mesh convergence tests are shown in Figure 2. The contact pressure was checked by changing the number of contact elements, and the mesh sensitivity analysis was completed when the variation between the previous pressure and the next value was less than 2% (26). Therefore, the optimum mesh size for the two prototypes was selected as 1 mm shown in Figure 2.

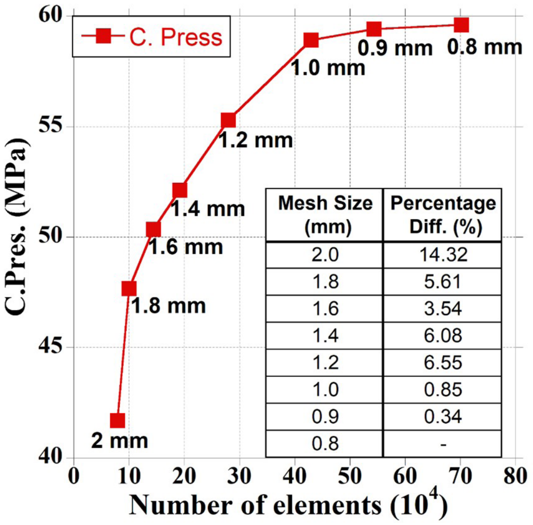

Mesh Size (mm)	Percentage Diff. (%)
2.0	14.32
1.8	5.61
1.6	3.54
1.4	6.08
1.2	6.55
1.0	0.85
0.9	0.34
0.8	-

Figure 2 The mesh convergence test result of 36 mm femoral head with 5 mm liner thickness

In uncoated prototypes, Figure 3b, the acetabular cup and femoral head were positioned at $45°$ on the flexion/extension (FE) axis to mimic the neutral position of the acetabular cup with respect to the pelvic bone. In coated prototypes, (Figure 1b) the coating film inserted between the acetabular cup and femoral head was positioned on the flexion/extension (FE) axis to mimic the neutral position of the acetabular cup with respect to the pelvic bone Figure 3b (20,26). The acetabular cup with coating film was rotated $45°$ on the flexion/extension (FE) axis to mimic the neutral position of the acetabular cup with respect to the pelvic bone Figure 3b. In the coated and the uncoated prototypes, acetabular cups were fixed on the outer surface allowing no rotation and translation movement (Figure 3a), while the femoral head was free to move and rotate in each direction (28–30). The load was applied at the bottom side of the femoral head as shown in Figure 3a. The hard-on-hard bearing materials of hip implant materials of the model are available in

Table 1. The prototype simulations were performed under a constant load of 2500N. The acetabular cup and femoral head were positioned at 45° on the flexion/extension (FE) axis to mimic the neutral position of the acetabular cup with respect to the pelvic bone shown in Figure 4.

Table 1 Mechanical properties of hip implant bearing materials.

	Elastic Modulus (GPa)	Poisson Ratio
Stainless Steel (SS) (31)	196	0.30
Ti-6Al-4V (32)	110	0.30
CoCr (26)	220	0.29
Ti12Mo6Zr2Fe (TMZF) (33)	79.5	0.33

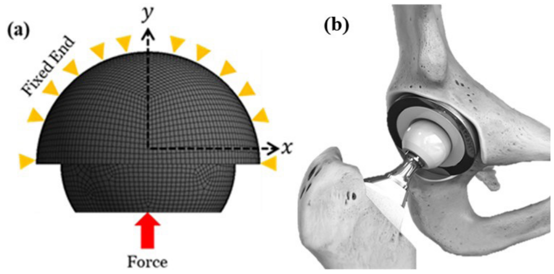

Figure 3 (a) The loading and boundary conditions and (b) total hip replacement of bearing couples

Computational And Analytical Wear

Archard wear equation (22) was used to predict the wear rates of all bearing components in THR. The linear wear depth (W_L) could be described as in Eq. 8

$$W_L = KxPxS \tag{8}$$

It was assumed that linear wear depth (W_L) is accumulated in proportion to the contact pressure (P) and the wear sliding distance (S). K is the dimensionless wear coefficient factor obtained from in vitro studies listed in Table 2 [14]. Similarly, the volumetric wear (W_V) is predicted by multiplying the linear wear depth (W_L) with the contact area (A_{ci}) (Eq. 9).

$$\mathrm{W}_w = W_L \; x \; A_{c_i} \tag{9}$$

In this study, linear and volumetric wear rates of bearing surfaces have been analyzed using analytical and numeric methods. Hip joint contact force (HJCF) and sliding distance (S) of normal gait cycles were obtained from a multibody simulation. The multibody simulations were performed using AnyBody Modeling System, and HJCF was calculated by using inverse dynamic and muscle recruitment optimization algorithms (23). The maximum sliding distance for one gait cycle was determined as a 7.77 mm in the literature (23). Also, it is assumed that an average human gait reaches to one million cycle in a year (11). Therefore, the linear and volumetric wear rates were calculated under this assumption (11,26,27). The coefficients of friction values are listed in Table 2.

In this study, linear and volumetric wear rates of bearing surfaces have been analyzed using analytical and numeric methods. Hip joint contact force (HJCF) and sliding distance

(S) of normal gait cycles were obtained from a multibody simulation. The multibody simulations were performed using AnyBody Modeling System, and HJCF was calculated by using inverse dynamic and muscle recruitment optimization algorithms (23). The maximum sliding distance for one gait cycle was determined as a 7.77 mm in the literature (23). Also, it is assumed that an average human gait reaches to one million cycle in a year (11). Therefore, the linear and volumetric wear rates were calculated under this assumption (11,26,27). The coefficients of friction values are listed in Table 2.

Table 2 The Archard wear factor and coefficient of friction properties of hip implant bearing materials.

	Archard Wear Factor (K) ***(mm^3/Nmm)***	**CoF**
CoCr/CoCr (26)	5×10^{-12}	0.20
CoCr/SS (34)	4.5×10^{-8}	0.15
CoCr/Ti-6Al-4V (35)	1.03×10^{-7}	0.58
CoCr/TMZF (35)	1.03×10^{-8}	0.58

RESULTS AND DISCUSSION

The contact pressure values were estimated as 59.418 *MPa* by the numeric method using FEM and it was calculated as 54.905 *MPa* using Hertz theory as an analytical method as shown in mathematical equations (Figure 4a). The percentage error formulation is used to compare the numerical and analytical results. The percentage error formulation is as follows:

$$Percentage\ error\ (\%) = \frac{Numerical\ result(FEM) - Analytical\ result(Hertz\ Theory)}{Analytical\ result(Hertz\ Theory)} \times 100 \qquad (10)$$

The minimum error using Eq. 10 between the analytical and the numerical calculation was 0.24% for 28 *mm* of the head diameter, while the maximum error was 11.79 % for 48-*mm* of head diameter as shown in Figure 4b. The effects of changing head radius, cup thickness, material combination, and coating thickness are provided in the following part in detail.

Head Radius Effects

The femoral head radius, from 28 to 48-mm, was investigated under 2500 N, whilst the clearance value of 0.05-mm and cup thickness of 5-mm were kept constant to investigate the effect of change of radius on contact pressure and total deformation on the cup bearing surface. The numerical maximum contact pressure value was obtained from the 28-mm head radius at a half contact angle of 150^{0} and also its contact area and linear wear were calculated as 53.61 mm^2 and 0.00294mm/Mc respectively, while the analytical maximum result was calculated at a half contact angle of 100^{0} and its contact area and linear wear were, 48.89 mm^2 and 0.00298 mm/Mc, respectively. The minimum contact pressure values were obtained from 48-mm of head radius at a half contact angle of 190^{0} (contact area of 92.52 mm^2 and volumetric wear of 0.1571 mm^3/Mc and 150 (contact area of 100.25 mm^2 and 0.1454 mm^3/Mc) in FEM and Hertz calculations, respectively. Additionally, the numerical and analytical results are shown in Figure 5 and are listed in Table 3.

Cup Thickness Effects

The effect of cup thickness is investigated in ten prototypes under a constant loading of 2500 N. All prototypes had the same head diameter of 36 mm with a 50 µm clearance. The cup thicknesses varied from 1 to 10 *mm*. The maximum contact pressure was determined as 67.127 *MPa* with 2 *mm* thickness, while the minimum contact pressure was obtained as 56.264 *MPa* with 10 *mm* thickness in the numerical analysis. In analytical results, the contact pressure was affected by changing the cup thickness. So, the percentage error was obtained as 21.6% with a cup thickness of 2-*mm* prototype, while the error in the prototype with a 10- *mm* thickness was only 1.9%. The prototypes with 10 *mm* of cup thickness produced similar contact pressure numerically and analytically. Additionally, pressures calculated analytically

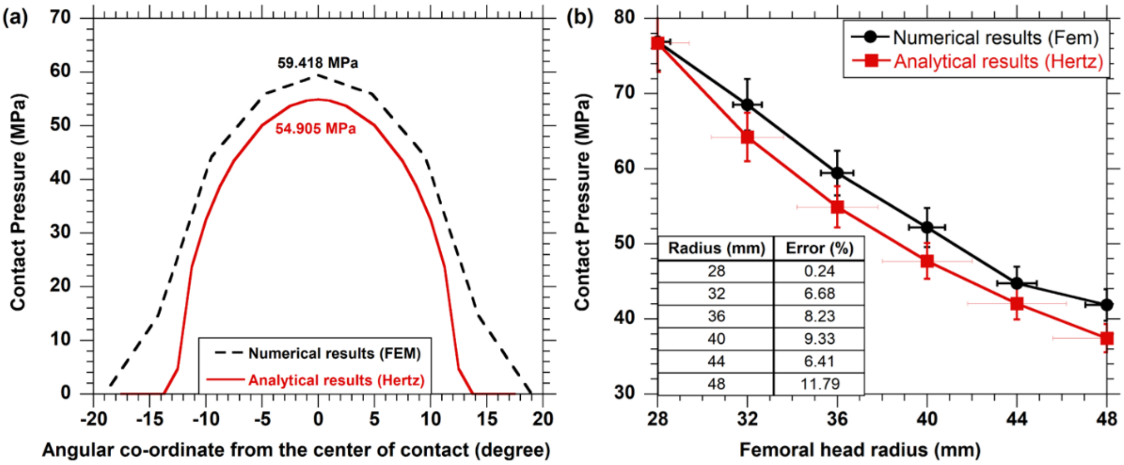

Figure 4 Comparison of numerical and analytical contact pressure of (a) 36 *mm* head radius, and (b) head radius varying from 28 *mm* to 48 *mm*.

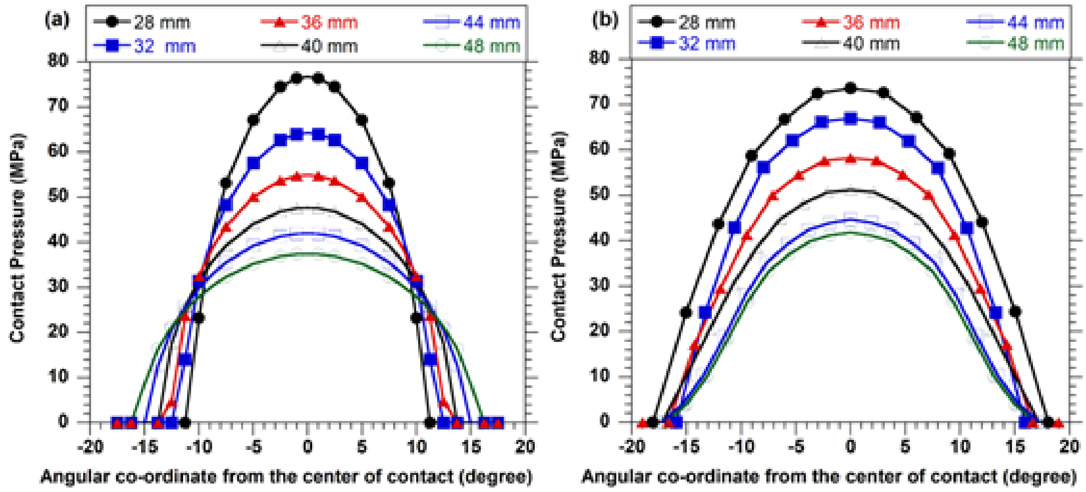

Figure 5 The effect of head radius changes on contact pressure analytical results (Hertz), and (b) numerical results (FEM) (under 2500 N with 0.05 mm clearance and 5 mm cup thickness)

Table 3 Comparison between numerical and analytical results of the femoral head effect,

Head Diameters *(mm)*	Numerical C. Pres. *(mPa)*	Analytical C. Pres. *(mPa)*	Error *(%)*	Numerical Linear wear *(µm/Mc)*	Analytical Linear wear *(µm/Mc)*	Error L.w. *(%)*	Numerical Vol. wear *(mm³/Mc m)*	Analytical Vol. wear *(mm³/Mc m)*	Error V.w. *(%)*
28	75.73	76.71	1.27	2.94	2.98	1.27	0.15771	0.14571	8.24
32	68.51	64.22	6.68	2.66	2.49	6.68	0.15097	0.14574	3.59
36	59.42	54.88	8.23	2.31	2.13	8.23	0.15666	0.14576	7.48
40	52.16	47.71	9.33	2.03	1.85	9.33	0.15753	0.14575	8.08
44	44.72	42.03	6.41	1.74	1.63	6.41	0.14720	0.14578	0.97
48	40.45	37.43	8.06	1.57	1.45	8.06	0.14539	0.14578	0.27

were kept constant, while contact pressures calculated by numeric methods were changed with the varying cup thicknesses (Figure 6a). The pressure distribution with respect to the predicted contact half-angle is shown in Figure 6b. The maximum linear wear rate was calculated at 0.0026 mm/Mc at a 1- *mm* cup thickness, while the minimum linear wear rate was 0.0022 mm/Mc at a 10- *mm* cup thickness in numeric methods. The difference between the maximum and minimum linear wear rates was 18.7 %. Also, the maximum and the minimum errors between numerical and analytical methods were 21% and 1.9%, respectively. Similarly, the maximum volumetric wear rate was calculated as 0.17618 mm^3/year at a 1 *mm* cup thickness, while the minimum linear wear rate was 0.0014834 mm^3/Mc at a 10 *mm* cup thickness. The maximum and minimum error of volumetric wear rates between numerical and analytical methods were 20.2% and 1.19%, respectively. The detailed information on the contact pressure and wear rates varying cup thicknesses are listed in Table 4.

The Effects Of Material Combination In Bearing Couples

CoCr material was mostly used in THR applications due to superior mechanical properties and excellent wear performances (36,37). So, all metal-bearing materials mostly used in THR applications were analyzed numerically and analytically in this study. The selected materials were SS, Ti64, and TMZF. Therefore, the effects of material combination with respect to CoCr material were investigated under constant loading of 2500 N. All prototypes had the same head diameter of 36 mm with and 50 µm clearance. The cup thickness was kept constant at 5 *mm* to minimize the effect of cup thickness. These analyzes are examined in two groups by changing the head and cup materials.

The maximum contact pressure was calculated as 57.65 *MPa* using the numerical and 52.87 *MPa* using the analytical methods for CoCr-on-SS, while contact pressures were 43.10 *MPa* in the numerical and 36.46 *MPa* in the analytical methods for CoCr-on-TMZF bearing couple. The maximum linear wear rates were obtained as 45.602 mm/year in the numerical and 33.613 mm/Mc in the analytical methods for CoCr-on-Ti64, the minimum linear wear rates were 20.157 mm/year in the numerical and 18.486 mm/Mc in the analytical methods for CoCr-on-SS. The maximum and minimum errors of linear wear rates between the numerical and analytical methods were 35.67 % and 9.04%, respectively. Similarly, the maximum volumetric wear rates were 3094.76 mm^3/Mc in the numerical and 2297.07 mm^3/Mc in the analytical methods for CoCr-on-Ti64, the minimum volumetric wear rates were as 1367.98

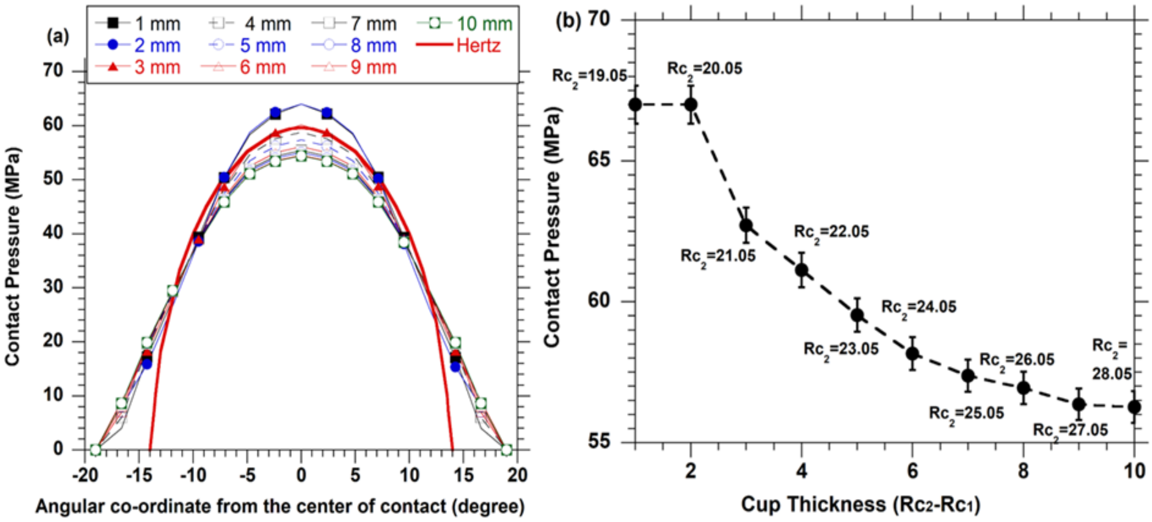

Figure 6 Contact pressure vs (a) half contact angle, and (b) cup thickness.

mm^3/Mc in the numerical and 1263.31 mm^3/Mc in the analytical methods for CoCr-on-SS. The maximum and minimum errors of volumetric wear rates between the numerical and the analytical methods were 34.73 % and 8.29%, respectively. The detailed information on the contact pressure and wear rates of varying material combinations are listed in Table 5.

Coating Film Material Combinations And Thickness

The effects of the coating material and optimum coating thickness were examined using the prototypes which had a femoral head diameter of 36 *mm*, clearance of 0.05 *mm*, under the loading of 2500 N. Using three different coating materials, SS, Ti6Al4V, and TMZF, respectively CoCr acetabular cup surfaces were coated by varying coating thicknesses of 100 µm, 250 µm, and 500 µm. In total, 9 prototypes were designed. After running the simulations with nine prototypes using finite element method (FEM), the contact areas were 68.33 mm^2 for CoCr/CoCr, 70.94 mm^2 for CoCr/SS, 89.29 mm^2 for CoCr/Ti64 and 102.84 mm^2 for CoCr/TMZF for all coating thicknesses, respectively. The highest contact pressure on cup surfaces with SS coating material was 53.6 *MPa* with a coating thickness of 100 µm as listed in Table 6, while the minimum contact pressure on cup surfaces with TMZF coating material was 39.6 MPa with a coating thickness of 500 µm. The maximum number of cycles required to remove for each coating material on cup surfaces are given in Table 6. The maximum survival cycles of coating material is obtained approximately as 32000 cycles at the SS coated cup with 500 µm coating thickness. However, the minimum survival cycles of coating material is obtained as 2532 cycles at the TMZF

Table 4 The effect of cup thicknesses on contact pressures

Cup Thick *(mm)*	Num. C.Pres. *(MPa)*	Ana. C. Pres. *(MPa)*	Error *(%)*	Numerical Linear wear *(µm/Mc)*	Analytical Linear wear *(mm/Mc)*	Error L.w. *(%)*	Numerical Vol. wear *(mm³/Mc)*	Analytical Vol. wear *(mm³/Mc)*	Error V.w. *(%)*
1	66.823	54.88	21.023	2.60	2.15	21.023	0.17618	0.14659	20.18
2	67.127		21.574	2.61		21.574	0.17698		20.73
3	62.714		13.581	2.44		13.581	0.16535		12.79
4	61.124		10.702	2.37		10.702	0.16116		9.93
5	59.521		7.799	2.31		7.799	0.15693		7.05
6	58.159		5.332	2.26		5.332	0.15334		4.60
7	57.375		3.912	2.23		3.912	0.15127		3.19
8	56.939		3.122	2.21		3.122	0.15012		2.41
9	56.355		2.065	2.19		2.065	0.14858		1.36
10	56.264		1.900	2.19		1.900	0.14834		1.19

Table 5 The effects of the material combinations on contact pressures (analytical (Hertz), and (b) numerical results (FEM))

Bearing Couple		Num. C. P.	Ana. C. P.	Num. L.w	Ana. L.w	Error L.w.	Num. V.w.	Ana. V.w.	Error V.w.
Head	**Cup**	*(MPa)*	*(MPa)*	$\left(\frac{\mu m}{Mc}\right)$ X1000	$\left(\frac{\mu m}{Mc}\right)$ X1000	(%)	(mm^3/Mc)	(mm^3/Mc)	(%)
CoCr	SS	57.65	52.87	20.157	18.486	9.041	1367.98	1263.31	8.29
CoCr	Ti64	47.92	42.00	38.351	33.613	14.095	2602.68	2297.07	13.30
CoCr	TMZF	43.10	36.46	34.493	29.179	18.212	2340.89	1994.08	17.39
SS	CoCr	59.42	52.87	20.776	18.486	12.389	1409.98	1263.31	11.61
Ti64	CoCr	56.98	42.00	45.602	33.613	35.667	3094.76	2297.07	34.73
TMZF	CoCr	44.37	36.46	35.510	29.179	21.695	2409.87	1994.08	20.85

coated cup with 100 µm coating thickness.

The main purpose of this study is to analyze the parameters affecting the contact pressure on metal-on-metal (MoM) implants using analytical and numerical methods as a part of the verification process for the contact pressure values. Moreover, to compare the effects of the parameters on contact pressure, the contact radius and the contact area values were calculated using Hertz contact theory analytically, while these results were also obtained using the numerical output of finite element method (FEM) numerically Additionally, the effects of different design parameters such as head diameters, bearing material combinations, coating materials and their thickness on contact pressure were analyzed. And these results were used in the calculation of linear and volumetric wear rates of MoM bearing couples.

Table 6 Contact pressure and linear and volumetric wear rates of three coating materials varying with different coating thickness.

Coating Thickness	SS	Ti64	TMZF	SS	Ti64	TMZF
	Contact Pressure			Max cycles to remove coating material		
(µm)	*(MPa)*			*(cycles)*		
100	53.6	53.0	49.3	5348	2359	2532
250	48.2	47.1	39.6	14793	6631	7886
500	44.8	43.5	39.5	31847	14368	15823

The contact pressure of ceramic-on-ceramic bearing components (9) had an error of 30% between the analytical and numerical solutions, while the metal-on-polyethylene bearing couple model (38) had an error of 27.5%. In our study, the percentage error was calculated as 4.9% under the same loading and boundary conditions and also the same geometrical dimensions in the literature (9,38). A similar situation was encountered in calculations of half contact angle; for example, while the error is about 26.7% in the clearance calculations, this is about 25% in head radius calculations. Although Hertz contact theory is frequently used in the design of hip implants for understanding contact mechanics [10]–[12],[19]–[23], the effects of cup or coating thickness on the contact pressure and predicting wear estimation have not been studied. Hertz contact theory is only based on the inferences of contacting surfaces (22,40). Similarly, there are many studies on the effect of head size using numerical and experimental methods in the literature (38,41–44). These studies conclude that the contact pressure increases with the decreasing head size and the volumetric wear increases with the decrease of the head size based on the Hertz contact theory. Keeping the head size constant with a thicker liner and the coating material corresponds to a lower peak contact stress and larger contact area. Increases in the contact area result in higher wear rates of bearing couples (41–44).

Our results are also in line with these results as demonstrated in the results section. When the MoM bearing components have a larger diameter, the volumetric wear rates of bearing surfaces are reduced (43,44). For the 36 mm head size model under 2500 N, the contact pressure and the contact area are 54.52 MPa and 76.25 mm^2 respectively, in the numeric model and 54.9 MPa and 77.16 mm^2 in the analytic model, respectively. In the literature, for 39 mm femoral head size, the contact pressure was calculated as 40 MPa with a contacting area of 74 mm^2(44). When the head size increases, the errors between the numeric and the analytic results increase. One of the most important reasons for these errors is that the prototypes with higher head sizes have a higher number of contact elements and higher moments of inertia. Therefore, the contact elements under the same loading conditions results in more fluctuations and penetration at the contact surfaces. However, these situations are not valid in analytical studies. Because Hertz contact theory, as analytical study, only considers the contact surfaces as a 2-dimensional geometry, while the numerical studies are performed in 3-dimensional geometry including the inertia, mass, moment, variables etc. (22,41).

In our study, the effects of cup thickness ranging from 1 to 10 mm were analyzed numerically and analytically. The pressure on the cup bearing surface decreased exponentially by increasing the cup thickness and continued up to 9 mm of the cup thickness. At 10 mm of the cup thickness parameter value, the cup thicknesses parameter had no effect on the output, and the difference between the numerical results and the analytical results decreased from 21.02 to 1.9 percent. In Hertz contact theory, the contact pressure is kept constant while changing the cup thickness, since this theory only focuses on the effect of contacting the bearing surface. However, this assumption cannot be valid for the numerical results, since in the numeric approach the mass and volume parameters are included using FEM.

The linear wear rates of CoCr-on-CoCr bearing couples were obtained at 2.5 µm/Mc (26). In another study in the literature, the predicted total linear wear was calculated as 1.28 µm/Mc and the maximum Hertzian contact radius as 3.94 mm, while the CoCr head diameter is 27.899 mm with a 79 µm clearance under applied loading of 2085 N (45). Another study shows that the linear wear rates ranged from 2.9 to 12.8 µm/Mc, with the femoral head radius of 14 mm (46). These results are consistent with our study. In our study, the linear wear was obtained as 2.98 µm/Mc in analytical methods and 2.98 µm/Mc in numerical methods, while the maximum contact radius was calculated as 3.945 mm in analytical methods and estimated as 4.13 mm in numeric methods.

The materials mostly used in THR application against CoCr material are also analyzed in numerical and analytical methods. These materials are SS, Ti6Al4V, and TMZF, respectively. The maximum contact pressure was 59.42 MPa for CoCr-CoCr bearing couple, while the minimum contact pressure value was 43.10 MPa for CoCr-TMZF bearing couple. It produced the same results about contact pressures and contact areas analytically whether the bearing pairs were made of CoCr (head)-SS (cup) or SS (head)-CoCr(cup). However, it produced different pressure and contact areas in numeric methods when the bearing couples changed. When the head material of CoCr and cup material of SS is selected, the contact pressure, the linear wear, and the volumetric wear rates were 57.65 MPa, 20157 µm/Mc, 1367.98 mm^3/Mc, respectively. The errors of linear and volumetric wear rates between the numeric and the analytic methods were 9.041% and 8.29%, respectively. When the head material of SS and cup material of CoCr was selected, the contact pressure, linear wear, and volumetric wear rates were 59.42 MPa, 20776 µm/Mc, 1409.98 mm^3/Mc, respectively. The errors of linear and volumetric wear rates between numeric and analytic methods were increased from 9.04 to 12.4% and from 8.29 to 11.61%, respectively. These differences were observed to have depended on the material combination of the bearing couple. Unfortunately, these results could not be compared to the data in the literature. Because there has not been any other study providing a comparison of changing bearing couples.

The effects of coating material and coating thickness on contact pressure, and linear and volumetric wear rates were also analyzed in our study. Three different coating thicknesses were modelled with three different coating materials. The coating thickness was chosen as 100µm, 250µm ve 500 µm, and the coating materials are SS, Ti6Al4V, and TMZF respectively. The maximum contact pressure was obtained as 53.6 MPa when coated with 100 µm coating thickness of SS, while the minimum contact pressure was obtained as 39.6 MPa with 500 µm coating thickness of TMZF. The coating thickness directly affected the contact pressure, the linear wear, and the volumetric wear rates. Also, the coating thickness of 500 µm for all the bearing couples had the lowest contact pressure and the linear and volumetric wear rates. It was observed that the metallic coating materials used in this study were insufficient considering higher wear rates for hip implants application. Our results are compared and considered to be consistent with the literature (47,48).

The analytical data is consistent with numerical data under the same loading and boundary conditions. To understand the effect of contact pressure on linear and volumetric wear depth, we calculated the wear rates over one million cycles. This study focuses on the primary results of contact pressure and then uses this information to compare the primary effects of contact pressure on wear rates. In our study, analytic and numeric models assumed smooth bearing surface and constant friction coefficients. Since Hertz contact theory is only valid on a non-adhesive and elastic contact on smooth surfaces (13,40). However, the bearing surfaces can form a rough surface and worn geometry depending on the wear depth (26,27). Also, the coefficient of friction in reality, is known to be changing and not constant (37). These problems will be addressed in future studies. Despite these limitations, this study provides useful information for implant designers while optimizing their products as they lead to low contact pressures. This study could open a new window into understanding the initial effects of geometrical parameters and material combination on lifespan of different THR implants while analyzing any other futuristic properties.

CONCLUSION

In this study, we demonstrated contact mechanics and wear rates of bearing couples using numeric and analytic methods. The effect of head size, cup thickness, material combination of bearing couple, coating material, and film thickness on contact pressure distribution and wear rates were investigated in detail. The cup thickness was observed to have a significant effect on the contact pressure, linear and volumetric wear rates of bearing couples. When the cup thickness was selected as 10 mm, the contact pressure and wear rates decreased by 16% approximately. Additionally, the error between the numeric and analytic results decreased from 21.02 to 1.9% for the contact pressure and from 20.18 to 1.19% for the volumetric wear rates. Similarly, optimum selection of the material combination of bearing couples decreased the contact pressure by 27%. Although the material combination had no positive effect on the wear rates of bearing surfaces, it could be minimizing the stress shielding effects of the bone underneath the hip implants. It is concluded when the film thickness increases from 100 to 500 µm, 18-20% decrease in the contact pressure and linear and volumetric wear rates were observed for all the coating materials, The methodology and the results used in this study, could be useful for implant designers during design optimization studies.

Acknowledgement

The study was supported by the TUBITAK 2232 Funding program under the name of ‘118C188 New Generation Implants for All’ project.

References

1. Merola M, Affatato S. Materials for hip prostheses: A review of wear and loading considerations. Materials. 2019;12(3).
2. Charnley J, Cupic Z. The Nine and Ten Year Results of the Low-

Friction Arthroplasty of the Hip. Clinical Orthopaedics and Related Research®. 1973;95.

3. McKee GK, Watson-Farrar J. REPLACEMENT OF ARTHRITIC HIPS BY THE McKEE-FARRAR PROSTHESIS. The Journal of Bone and Joint Surgery British volume [Internet]. 1966 May 1;48-B(2):245–59. Available from: https://doi.org/10.1302/0301-620X.48B2.245
4. Smith SL, Dowson D, Goldsmith AAJ. The lubrication of metal-on-metal total hip joints: A slide down the Stribeck curve. Proceedings of the Institution of Mechanical Engineers, Part J: Journal of Engineering Tribology [Internet]. 2001 May 1;215(5):483–93. Available from: https://doi.org/10.1243/1350650011543718
5. Learmonth ID, Gheduzzi S, Vail TP. Clinical experience with metal-on-metal total joint replacements: Indications and results. Proceedings of the Institution of Mechanical Engineers, Part H: Journal of Engineering in Medicine [Internet]. 2006 Feb 1;220(2):229–37. Available from: https://doi.org/10.1243/095441105X69123
6. Fisher J, Bell J, Barbour PSM, Tipper JL, Mattews JB, Besong AA, et al. A novel method for the prediction of functional biological activity of polyethylene wear debris. Proceedings of the Institution of Mechanical Engineers, Part H: Journal of Engineering in Medicine [Internet]. 2001 Feb 1;215(2):127–32. Available from: https://doi.org/10.1243/0954411011533599
7. National Joint Registry for England Wales Northern Ireland and the Isle of Man. 16th Annual Report 2019:National Joint Registry for England, Wales, Northern Ireland and the Isle of Man. NJR 16th Annual Report 2019 [Internet]. 2019;(December 2018):1–248. Available from: https://www.hqip.org.uk/wp-content/uploads/2018/11/NJR-15th-Annual-Report-2018.pdf
8. Mak MM, Jin ZM. Analysis of contact mechanics in ceramic-on-ceramic hip joint replacements. Proceedings of the Institution of Mechanical Engineers, Part H: Journal of Engineering in Medicine [Internet]. 2002 Apr 1;216(4):231–6. Available from: https://doi.org/10.1243/09544110260138718
9. Cilingir AC. Finite element analysis of the contact mechanics of ceramic-on-ceramic hip resurfacing prostheses. Journal of Bionic Engineering [Internet]. 2010;7(3):244–53. Available from: http://dx.doi.org/10.1016/S1672-6529(10)60247-8
10. Chethan KN, Shyamasunder Bhat N, Zuber M, Satish Shenoy B. Finite element analysis of hip implant with varying in taper neck lengths under static loading conditions. Computer Methods and Programs in Biomedicine [Internet]. 2021;208:106273. Available from: https://doi.org/10.1016/j.cmpb.2021.106273
11. K N C, Ogulcan G, Bhat N S, Zuber M, Shenoy B S. Wear estimation of trapezoidal and circular shaped hip implants along with varying taper trunnion radiuses using finite element method. Computer Methods and Programs in Biomedicine [Internet]. 2020;196:105597. Available from: https://doi.org/10.1016/j.cmpb.2020.105597
12. Pandiyarajan R, Starvin MS, Ganesh KC. Contact Stress Distribution of Large Diameter Ball Bearing Using Hertzian Elliptical Contact Theory. Procedia Engineering [Internet]. 2012;38:264–9. Available from: https://www.sciencedirect.com/science/article/pii/S1877705812019479
13. Wang QJ, Zhu D. Hertz Theory: Contact of Spherical Surfaces BT - Encyclopedia of Tribology. In: Wang QJ, Chung Y-W, editors. Boston, MA: Springer US; 2013. p. 1654–62. Available from: https://doi.org/10.1007/978-0-387-92897-5_492
14. Mihçin Ş, Ciklacandir S. TOWARDS INTEGRATION OF THE FINITE ELEMENT MODELING TECHNIQUE INTO BIOMEDICAL ENGINEERING EDUCATION. Biomedical Engineering: Applications, Basis and Communications [Internet]. 2021 Nov 3;2150054. Available from: https://doi.org/10.4015/S101623722150054X
15. Göktaş H, Subaşi E, Uzkut M, Kara M, Biçici H, Shirazi H, et al. Optimization of Hip Implant Designs Based on Its Mechanical Behaviour BT - Biomechanics in Medicine, Sport and Biology. In: Hadamus A, Piszczatowski S, Syczewska M, Błażkiewicz M, editors. Cham: Springer International Publishing; 2022. p. 37–43.
16. Celik E, Alemdar F, Bati M, Dasdemir MF, Buyukbayraktar OA, Chethan KN, et al. Mechanical Investigation for the Use of Polylactic Acid in Total Hip Arthroplasty Using FEM Analysis BT - Biomechanics in Medicine, Sport and Biology. In: Hadamus A, Piszczatowski S, Syczewska M, Błażkiewicz M, editors. Cham: Springer International Publishing; 2022. p. 17–23.
17. Mihcin S, Sahin AM, Yilmaz M, Alpkaya AT, Tuna M, Akdeniz S, et al. Database covering the prayer movements which were not available previously. Scientific Data [Internet]. 2023;10(1):276. Available from: https://doi.org/10.1038/s41597-023-02196-x
18. Hertz H. Ueber die Berührung fester elastischer Körper. Ueber die Berührung fester elastischer Körper [Internet]. 1882; Available from: https://www.degruyter.com/document/doi/10.1515/crll.1882.92.156/html
19. Alpkaya AT, Mihcin S. Dynamic computational wear model of PEEK-on-XLPE bearing couple in total hip replacements. Medical Engineering & Physics [Internet]. 2023;104006. Available from: https://www.sciencedirect.com/science/article/pii/S1350453323000619
20. Alpkaya AT, Mihçin Ş. The Computational Approach to Predicting Wear: Comparison of Wear Performance of CFR-PEEK and XLPE Liners in Total Hip Replacement. Tribology Transactions [Internet]. 2023;66(1):59–72. Available from: https://doi.org/10.1080/10402004.2022.2140727
21. Alpkaya AT, Yılmaz M, Şahin AM, Mihçin DŞ. Investigation of stair ascending and descending activities on the lifespan of hip implants. Medical Engineering and Physics. 2024;126.
22. Archard JF, Hirst W, Allibone TE. The wear of metals under unlubricated conditions. Proceedings of the Royal Society of London Series A Mathematical and Physical Sciences [Internet]. 1956 Aug 2;236(1206):397–410. Available from: https://doi.org/10.1098/rspa.1956.0144
23. Varady PA, Glitsch U, Augat P. Loads in the hip joint during physically demanding occupational tasks: A motion analysis study. Journal of Biomechanics [Internet]. 2015;48(12):3227–33. Available from: http://dx.doi.org/10.1016/j.jbiomech.2015.06.034
24. Bergmann G, Graichen F, Rohlmann A. Hip joint loading during walking and running, measured in two patients. Journal of Biomechanics. 1993;26(8):969–90.
25. Bergmann G, Bergmann G, Deuretzabacher G, Deuretzabacher G, Heller M, Heller M, et al. Hip forces and gait patterns from rountine activities. Journal of Biomechanics. 2001;34:859–71.
26. Uddin MS, Zhang LC. Predicting the wear of hard-on-hard hip joint prostheses. Wear [Internet]. 2013;301(1–2):192–200. Available from: http://dx.doi.org/10.1016/j.wear.2013.01.009
27. Nithyaprakash R, Shankar S, Uddin MS. Computational wear assessment of hard on hard hip implants subject to physically demanding tasks. Medical and Biological Engineering and Computing. 2018;56(5):899–910.
28. Strickland MA, Dressler MR, Taylor M. Predicting implant UHMWPE wear in-silico: A robust, adaptable computational-

numerical framework for future theoretical models. Wear [Internet]. 2012;274–275:100–8. Available from: http://dx.doi.org/10.1016/j.wear.2011.08.020

29. Ming Song ST, Ashkanfar A, English R, Rothwell G. Computational method for bearing surface wear prediction in total hip replacements. Journal of the Mechanical Behavior of Biomedical Materials. 2021 Jul 1;119.
30. Ruggiero A, Sicilia A. Lubrication modeling and wear calculation in artificial hip joint during the gait. Tribology International [Internet]. 2020;142(September 2019):105993. Available from: https://doi.org/10.1016/j.triboint.2019.105993
31. Bhatt H, Goswami T. Implant wear mechanisms - Basic approach. Biomedical Materials. 2008;3(4).
32. Güden M, Alpkaya AT, Hamat BA, Hızlı B, Taşdemirci A, Tanrıkulu AA, et al. The quasi-static crush response of electron-beam-melt Ti6Al4V body-centred-cubic lattices: The effect of the number of cells, strut diameter and face sheet. Strain. 2022;58(3):1–20.
33. Yang X, Hutchinson CR. Corrosion-wear of β-Ti alloy TMZF (Ti-12Mo-6Zr-2Fe) in simulated body fluid. Acta Biomaterialia [Internet]. 2016;42:429–39. Available from: http://dx.doi.org/10.1016/j.actbio.2016.07.008
34. Chen Y, Wu JM, Nie X, Yu S. Study on failure mechanisms of DLC coated Ti6Al4V and CoCr under cyclic high combined contact stress. Journal of Alloys and Compounds [Internet]. 2016;688:964–73. Available from: http://dx.doi.org/10.1016/j.jallcom.2016.07.254
35. Zhang T, Harrison NM, McDonnell PF, McHugh PE, Leen SB. A finite element methodology for wear-fatigue analysis for modular hip implants. Tribology International [Internet]. 2013;65:113–27. Available from: http://dx.doi.org/10.1016/j.triboint.2013.02.016
36. Heuberger R, Stöck C, Sahin J, Eschbach L. PEEK as a replacement for CoCrMo in knee prostheses: Pin-on-disc wear test of PEEK-on-polyethylene articulations. Biotribology. 2021 Sep 1;27.
37. Scholes SC, Unsworth A. Wear studies on the likely performance of CFR-PEEK/CoCrMo for use as artificial joint bearing materials. Journal of Materials Science: Materials in Medicine. 2009 Jan;20(1):163–70.
38. Askari E, Andersen MS. A closed-form formulation for the conformal articulation of metal-on-polyethylene hip prostheses: Contact mechanics and sliding distance. Proceedings of the Institution of Mechanical Engineers, Part H: Journal of Engineering in Medicine [Internet]. 2018 Nov 16;232(12):1196–208. Available from: https://doi.org/10.1177/0954411918810044
39. Meng Q, Liu F, Fisher J, Jin Z. Contact mechanics and lubrication analyses of ceramic-on-metal total hip replacements. Tribology International [Internet]. 2013;63:51–60. Available from: http://dx.doi.org/10.1016/j.triboint.2012.02.012
40. Baxter JW, Bumby JR, Johnson KL. One Hundred Years of Hertz Contact. Proceedings of the Institution of Mechanical Engineers [Internet]. 1982 Jun 1;196(1):363–78. Available from: https://doi.org/10.1243/PIME_PROC_1982_196_039_02
41. Li G, Peng Y, Zhou C, Jin Z, Bedair H. The effect of structural parameters of total hip arthroplasty on polyethylene liner wear behavior: A theoretical model analysis. Journal of Orthopaedic Research. 2020;38(7):1587–95.
42. Tarasevicius S, Robertsson O, Kesteris U, Kalesinskas RJ, Wingstrand H. Effect of femoral head size on polyethylene wear and synovitis after total hip arthroplasty: A sonographic and radiographic study of 39 patients. Acta Orthopaedica. 2008;79(4):489–93.
43. Masaoka T, Clarke IC, Yamamoto K, Tamura J, Williams PA, Good VD, et al. Validation of volumetric and linear wear-measurement in UHMWPE cups - A hip simulator analysis. Wear. 2003;254(5–6):391–8.
44. Fisher J. Bioengineering reasons for the failure of metal-on-metal hip prostheses. The Journal of Bone and Joint Surgery British volume. 2011;93-B(8):1001–4.
45. Medley JB, Chan FW, Krygier JJ, Bobyn D. Comparison of alloys and designs in a hip simulator study of metal on metal implants. Clinical Orthopaedics and Related Research. 1996;329(SUPPL.):148–59.
46. Reinisch G, Judmann KP, Lhotka C, Lintner F, Zweymüller KA. Retrieval study of uncemented metal-metal hip prostheses revised for early loosening. Biomaterials. 2003;24(6):1081–91.
47. Guu YY, Lin JF, Ai CF. The tribological characteristics of titanium nitride coatings part i. Coating thickness effects. Wear. 1996;194(1–2):12–21.
48. Lin J, Sproul WD, Moore JJ, Lee S, Myers S. High rate deposition of thick CrN and Cr2N coatings using modulated pulse power (MPP) magnetron sputtering. Surface and Coatings Technology [Internet]. 2011;205(10):3226–34. Available from: http://dx.doi.org/10.1016/j.surfcoat.2010.11.039

HITTITE JOURNAL OF SCIENCE AND ENGINEERING

e-ISSN: 2148-4171
Volume: 11 • Number: 2
June 2024

Analysis of the Effects of Infusion Drips on Flow Rate and Volume Determination in IV Systems

Halid Ceylan[1] | **Ogan Karabaş**[2*] | **K. Süleyman Yiğit**[2]
[1]Department of Mechanical Engineering, Graduate School of Natural and Applied Sciences, Kocaeli University, 41000, Kocaeli, Türkiye.
[2]Department of Mechanical Engineering, Faculty of Engineering, Kocaeli University, 41000, Kocaeli, Türkiye.

Corresponding Author

Ogan Karabaş
E-mail: ogan.karabas@kocaeli.edu.tr Phone: +90 505 221 74 19
RORID[1,2]: https://ror.org/0411seq30

Article Information

Article Type: Research Article
Doi: https://doi.org/10.17350/HJSE19030000333
Received: 05.03.2024
Accepted: 05.06.2024
Published: 30.06.2024

Cite As

Karabas O, et al. Analysis of the Effects of Infusion Drips on Flow Rate and Volume Determination in IV Systems. Hittite J Sci Eng. 2024;11(2):69-75.

Peer Review: Evaluated by independent reviewers working in at least two different institutions appointed by the field editor.
Ethical Statement: Not available.
Plagiarism Checks: Yes - iThenticate
Conflict of Interest: The authors declare that they have no known competing financial interests or personal relationships that could have appeared to influence the work reported in this paper.

CRediT Author Statement:
Halid Ceylan: Conceptualization, Methodology, Software, Validation, Writing- original draft. **Ogan Karabaş:** Data curation, Visualization, Investigation. **K.Süleyman Yiğit**Supervision, Writing- review and editing.

Analysis of the Effects of Infusion Drips on Flow Rate and Volume Determination in IV Systems

Halid Ceylan[1] | Ogan Karabas[2*] | K. Süleyman Yigit[2]

[1]Department of Mechanical Engineering, Graduate School of Natural and Applied Sciences, Kocaeli University, 41000, Kocaeli, Türkiye.
[2]Department of Mechanical Engineering, Faculty of Engineering, Kocaeli University, 41000, Kocaeli, Türkiye.

Abstract

In this study, drop form flow examinations, which form the basis of IV applications used for therapeutic purposes, were performed. Fluid Intravenous (IV) is the practice of administering fluids into a vein. In IV applications, flow must be monitored in order to follow and control the treatment process. For this purpose, the fluid can be converted into drop form with a simple mechanism and the flow rate and volume data can be calculated by the drop counting method. Examining drop form flow processes and analyzing microdrops correctly increases the accuracy in calculating flow data and, most importantly, increases the quality of treatment in IV applications. In the scope of this study, the formation processes of microdrops and the affecting parameters were analyzed. Along with microdrop analysis, error evaluation of the drop counting method and evaluation of measurement techniques were carried out to ensure a healthy and accurate measurement process. System tests and verification were carried out with optical systems, one of the measurement techniques. As a result, this study was carried out on the importance of monitoring systems and measurement parameters in IV applications.

Keywords: Intravenous (IV) system, Gravity-Effected flow, Microdrip methodology, Drop counting, Optical sensing

INTRODUCTION

The technique of administering fluids into a vein through a needle or catheter is called infusion or fluid intravenous (IV). Fluid intravenous was developed following the need for resuscitation, that is, supportive treatment. The IV procedure is frequently used by doctors, nurses, anesthetists, and caregivers in areas such as the operating room, intensive care, interventional radiology, or assistive procedure practices [1].

Modern IV systems consist of 5 basic components. Our first component, the reservoir, is the component that contains the fluid required for the IV process. Reservoirs usually consist of plastic bags or glass bottles. Our second component, the drip chamber, structurally resembles a thick needle. The drip chamber consists of a pipe with a curved end to allow the flow to occur and a transparent chamber to monitor the flow. The flow occurs in drop formation or continuously, depending on the flow rate in the pipe section of the drip chamber. It enters the reservoir and acts as a pathway for flow. In Figure 2.A, microdrop formation can be seen at the pipe tip when the flow rate is low. Factors affecting the formation of microdroplets are the pipe diameter, the surface tension of the liquid and the density of the liquid [2]. In Figure 2.B, it is seen that continuous flow occurs from the pipe end when the flow rate is high. Our 3rd component, the throttle valve, is used to control the flow. Basically, it works by crushing the pipe in which the fluid flows, that is, by reducing the diameter of the pipe. Due to the decrease in pipe diameter, resistance to flow is created and the flow rate decreases. Our 4th component, the catheter, is the component through which fluid is administered into the vein. A catheter is a needle with a hole in it or a thin tube with a sharpened tip. Catheters can be of different diameters depending on the vessel to be entered. Our 5th component, the pipe, is the component that connects our other 3 components to each other and in which the flow takes place (The drip chamber enters the reservoir directly thanks to its needle structure).

In IV procedures, flow begins from the reservoir and ends in a catheter designed to be placed in peripheral veins or tissue vessels outside the heart or in a central vein.

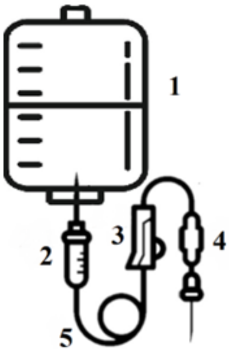

Figure 1 IV Set Components

Figure 2 A) Flow in Drop Form, B) Flow in Continious Form

In order for flow to occur, the reservoir pressure must be higher than the intravascular pressure. Reservoir pressure is affected by the pressure of the vessel to which the catheter is connected and gravity. In order for high pressure and flow due to this pressure to occur; the reservoir must be placed higher than the catheter connection point. Thus, gravity-based flow is achieved [3].

According to Kim et al., there are many situations where you can cause errors in clothing-based infusion systems. Pressure and other effects on droplet formations outside of human components vary widely. Microinfusion and macroinfusion systems were compared. In this mixture, the distinctions between systems, the infusion system dead volume and its distribution over drug delivery are emphasized [1].

According to Flack et al., the most important factors of drop formation in the drip chamber are surface tension, density and the inner environment of the drip chamber tube where the drops form. When the flow rate is increased, the drop diameter decreases due to these factors [2].

According to Stoneham, if infusion systems are based on gravity, it is unnecessary to constantly adjust the bag height to control the pressure and adjust the drop size. By adding a pressure regulator to the system, the system pressure can be kept stable and the flow rate can remain constant [3].

According to Singh et al., the Poiseuille equation cannot adequately describe the relationships between system variables in a perfusion model. Subtle changes in IV set length or design can have unexpectedly significant effects on flow. Non-Newtonian fluids and shear in the flow were cited as the reasons why the equation did not hold in these flows [4].

According to Tolman et al., Gibbs thermodynamics is applied by the theory of capillarity, the effect of droplet tension on the surface tension in droplet formation is found by the tension radius. He considers the process to play a prominent role in surface tension, especially in the formation of small droplets. Even reductions of up to 30% in droplet radii are recorded, it becomes clear that the Gibbs atmosphere is unreliable for these processes. Instead, he found the interconnection of tight mechanics and the measure of forces exerted by individual molecules more satisfactorily [5].

According to La Cour, the structure of the drop tube affects drop formation and drop diameter. He determined the correlation and error rates between drop diameter change and drop tube diameter. The fineness of the drip tube linearity caused a 10% change in the drop size and that this error rate increased exponentially to 40% depending on the flow rate [6].

According to Hillman, the change in drop diameter is related to the structure of the drop tube, the structure of the glass and PVC bag used as a reservoir, and the different viscosity of the liquids. The change in drop diameter with the formation and break-up time of the drop in the tube and determined that the speed-dependent diameter change was more dominant than viscosity [7].

According to MurphY et al., it is necessary to add the length of the pipe through which the flow occurs and the resistances arising from the drop chamber to the flow calculations created using the Poiseuille equation. For flow to occur, not only the pressure created by the reservoir is important, but also it is related to the venous pressure to which the catheter is connected and the drip chamber outlet pressure [8].

According to Pierce et al., as volume requirements change in infusion applications, the flow of fluid changes significantly. In a gravity-powered infusion system, the drop diameter gradually decreases as the flow rate increases in the flow realized with the microdrop set. Although the flow rate depends on the reservoir height, it defines a function depending on the size of the IV drip chamber, the length of the tube through which the flow occurs, and the size of the IV catheter [9].

According to Ogawa et al., in infusion applications, drop lengths after drop fall and drop rate increase linearly from 50 drops/min. to 1000 drops/min. IV administrations must be monitored by drip counter systems because infusion pumps are sensitive but expensive. The best alternative in monitoring systems is to perform measurement with a sensor type that uses electrical impedance difference, since infrared systems cannot detect continuous flow [10].

According to Bhavasaar et al., it has studied IV monitoring system with load cell sensor and vibration sensor in IV treatments. The system creates flow and volume data by measuring the weight of the reservoir with the load cell. In addition, measurements are made with the vibration sensor against the possibility of embolism, that is, air entering the vein [11].

According to Arfan et al., stake-holder feedback on the major issues while using IV drip set gives the following statistics. As per their survey, there is 70.60% need to keep track of the IV fluid that is being administered; the accuracy of the drip rate is 44.10% whereas clotting at sight of administration is 55.90% and blood backflow is 38.30% [12].

According to Kamble et al., both drop counting and drop diameter can be measured with the optical systems used in IV monitoring systems. Thus, cost-effective flow control can be achieved with a small number of components [13].

According to Tanwar et al., a combination of IV monitoring systems, optical and ultrasonic systems should be created. In his study, he performed pressure and volume control with ultrasonic sensors. In addition, it tried to minimize the risk of embolism by controlling air bubbles with the optical system. Remote monitoring and control of the system was provided by data communication via Wi-Fi [14].

According to Cahyanurani et al., if optical tracking systems are operated based on drop time, error rates remain below 1%. It has been observed that drop stability gives more accurate results in flows provided by pumped systems [15].

In liquid intravenous (IV) infusion applications, the flow rate is calculated by the drop counting method if the system is not connected to an electromechanical system. IV set manufacturers indicate how many mL one drop equals in the drip chambers they produce. Sets of 20 drops/mL are mainly used in the market. Additionally, sets up to 60 drops/mL are also available. In the drop counting method, for a set of 20 calculations, the time during which 20 drops have passed is counted. The ratio of the found time to hours gives us the approximate flow rate in mL that will pass in 1 hour. In this way, the practitioner performs the flow rate calculation at certain intervals depending on the suitability and criticality of the treatment. If deemed necessary, it adjusts with the throttle valve. Another reason for these controls is that situations such as stopping of intravenous flow and arm closure, which we describe as other factors, prevent the flow, and also the necessity of monitoring whether the fluid is administered properly.

In this study, we examined the effects and results of pressure changes on infusion sets as the main flow rate factor, excluding other factors. Unlike other studies in the literature, an electronic monitoring system that works with the drop counting method was created. In the system, based on optical principles, photodiodes, which are semiconductor elements that change the current flowing through them depending on the intensity of the light falling on them, were used as sensors. Functions were defined depending on the reduction in drop diameter in gradual flow rate ranges (Stage-1: 0-100 mL/h, Stage-2: 100-1000 mL/h). In the system where drop counting was performed with photodiodes, functions were processed depending on the flow rate and error correction was provided.

MATERIAL AND METHODS

Poiseuille equation; describes the relationship between fluid viscosity, pressure, pipe diameter, and flow. Flow rate (Q) passing through a pipe according to Equation (1).

$$Q = \frac{\Delta \mathrm{P}\pi \mathrm{r}4}{8\mu \mathrm{L}} \ (\mathrm{m}^3/s) \qquad (1)$$

It is inversely proportional to the pipe length (L) and fluid viscosity (μ), and directly proportional to the pressure drop along the pipe (ΔP) and pipe radius (r).

Poiseuille's equations are valid for non-turbulent flow and non-slip boundary ranges. The flow chart of Newtonian fluids independently satisfies the Poiseuille equations. It was stated that the Poiseuille equation, the research at the University of Wisconsin (UW), caused errors in flow rate programming in IV treatments. The reason for this is that in non-Newtonian fluids, negative effects occur due to changes in pipe diameter, liquid viscosity, drop chamber size and bag pressure in the system [4].

In non-Newtonian fluids, the diameter of liquid droplets is not constant. Droplet sizes; According to Equation (2), in these types of fluids, the surface tension changes depending on the molecular properties of the additives and especially the temperature [1].

$$r = \sqrt[3]{\frac{3\gamma d_t}{4\rho g}} \ (m) \qquad (2)$$

In IV applications, the drop counting method works by simplifying the system. In the drop counting method, negative effects may be observed in the treatment due to the accuracy of the linearity in the flow and volume graphs. In order to eliminate these negative effects, it is necessary to switch to electromechanical or purely electronic systems.

Monitoring systems are used for flow monitoring in electromechanical systems or electronic systems. Flow monitoring systems mainly control the flow status in electromechanical systems. Flow monitoring system is used to create flow and volume data in electronic systems. Although there are different systems such as obtaining data with weight difference by using load cells as sensors in flow monitoring systems or obtaining data with drop detection based on electromagnetic field change, systems built on optical foundations are mostly used. Photodiodes are preferred as sensors in optical systems due to their fast response times and stable operation. Photodiodes are sensors that allow current to flow depending on the intensity of light. The current flowing can be detected with the help of an added resistor in photodiode circuits. Depending on the value of the resistor, the system sensitivity can be adjusted. Light intensity can be determined using microprocessors from the voltage difference caused by the current flowing through the resistor. Figure 3 shows the optical detection device. In the device, an electromagnetic source, that is, an LED as a light source, is placed around the transparent chamber of the drop chamber, facing the photodiode. Thus, the lens effect of the drop passing through the chamber was also utilized. Due to this effect, droplets could be counted with varying light intensity.

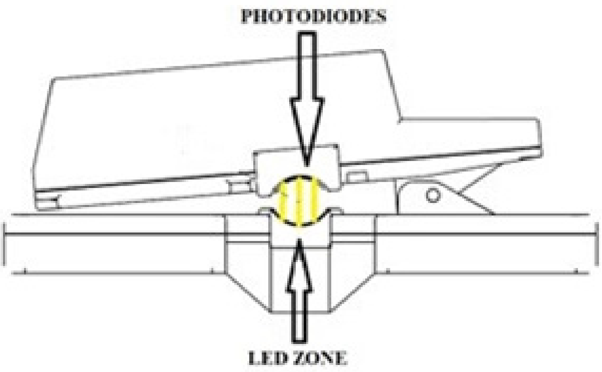

Figure 3 Optical Detection Device

Figure 4.A shows that there are 2 photodiodes in the device. During the drop passage in the system, a delay time occurs regardless of the time between the photodiodes placed on the vertical axis (Figure 4.B). While the drop counting process is carried out with these delays, the system's internal verification process is also carried out with its 2 sensors structure.

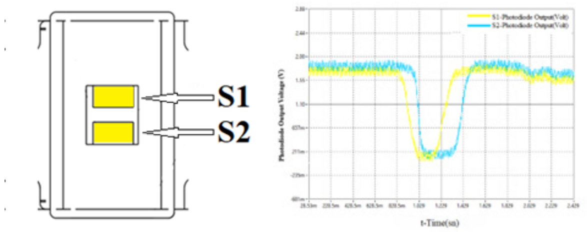

Figure 4 A) Photodiodes B) Flow to Vertical Axis Photodiodes Output Signals

With the drop counting process, volume data can be obtained regardless of time. The drip chamber has a capacity of 1/20 mL/drop. The volume of each drop was accepted as 1/20 mL. The derivative of the obtained volume data with respect to time creates flow data. A syringe pump was used to obtain gravity-induced pressure in the system. The purpose of this is to provide pressure change without changing the height of the reservoir. Syringe pumps are sensitive devices that can provide constant flow rate. In our system, liquid flow was provided to the infusion set at different speeds with the HARVARD APPARATUS brand 70200 model syringe pump. The fluid limitation device of the IV set on the fluid path in the system was opened completely and the device was rendered dysfunctional. In the system, fluid was transferred from the pump to the set via a 3-way valve. The sets used in the system are 20 drops/mL sets and different sets from different manufacturers were used.

With this study, differences in flow rate due to these changes caused by in-pipe shifts in droplet formation in the serum set were observed.

Flow at a constant flow rate and a certain volume was obtained with the syringe pump shown in Figure 5.A, which was used to obtain flow in the experiments. Reference Flow Rate (mL/h) and Reference Volume (mL) specified in Table 1 and Table 2 are the data of the syringe pump. The flow was transmitted to the drop chamber to which the measuring device in Figure 5.B was connected, using the standard drop counting method, with the help of pipes, thus the drops formed in the chamber were counted with the measuring device and flow rate and passing volume data were obtained with the system in Figure 6.

Figure 5 A) Syringe Pump B) Placement of the Measuring Device in the Drop Chamber

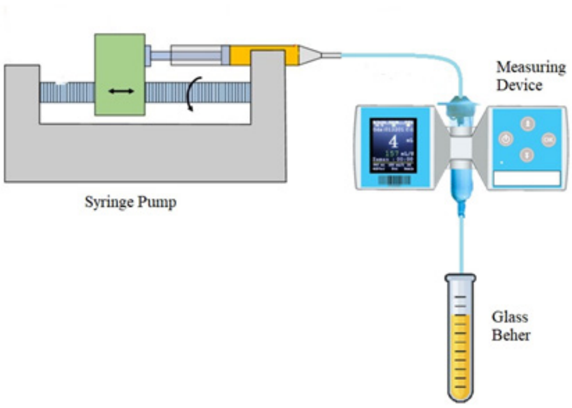

Figure 6 Schematic experimental setup

RESULTS AND DISCUSSION

In IV treatments, the speed of the fluid and the passing volume, directly affect the treatment. In the tests performed, changes in the diameter of the micro drops were detected depending on the increase or decrease in the flow rate. It has been observed that there are differences in flow rate and passing volume caused by these changes.

As seen in Table 1, resistances due to shear stresses occurring on the flow can be examined at 2 different flow rates. Since the flow rate is low in flows up to 0-100mL/h, results are produced in accordance with the Poiseuille equations. The reason for this is that due to the low flow rate, shear stress resistance remains low and its effect on the system remains low. At speeds above 100mL/h, reductions in drop diameter begin to appear significantly. In this flow rate range, the resistance due to shear stress reveals a linear graph. This linearity continues up to 100-1000mL/h flow rate.

Measured Flow Rate (Q_o) calculated according to Equation 3 and Measured Volume (V_o) calculated according to Equation 4 are the data obtained by the standard drop counting method. Measured Flow Rate (Q_o) was found by dividing the time 20 drops passed to 1 hour according to Equation (3), finding $\Delta q_{(drop/h)}$ and dividing it to the serum set constant $C_{(drop/mL)}$. Measured Volume (V_o) was found by counting the total passing drop $\Delta q_{(OD)}$ according to Equation (4) and proportioning it to the serum set constant $C_{(drop/mL)}$.

$$C_{drop/mL} = 20\ (drop/mL) \qquad (3)$$

$$Q_O = \frac{\Delta q_{drop/h}}{C_{drop/mL}}\ (mL/h) \qquad (4)$$

Isotonic solution, electrolyte solution and dye added solution were used as fluid in the experiments. Isotonic solutions are solutions in which salt is dissolved in certain percentages. Their properties are equal to osmotic pressure and they are the most used liquid in the healthcare system. The isotonic solutions used contain 0.45% and 0.9% sodium chloride. Electrolyte solution can also be referred to as sugar serum. It is a solution administered intravenously and used to meet calorie needs, especially in cases of nutritional problems. The electrolyte solutions used contained 5%, 10% and 20% dextrose in the content stream. Dye solutions, chemotherapy solutions used in infusion treatments, solutions containing amino acids, etc. For solutions, it is the solution obtained by mixing baticon (povidone-iodine) in isotonic solution. The study of situations where the lens effect of the drop does not occur through dye solutions has been examined.

Table 1 Flow Rates Results

Reference Flow Rates (mL/h)	Measured Flow Rates (mL/h)	Error Rate (%)
25	26	4,0
50	51	2,0
100	101	1,0
200	193	3,6
250	244	2,4
500	474	5,4
750	694	8,0
1000	878	13,8
1250	1110	12,6

When we look at the volume comparisons in the results in Table 2, the same results are obtained depending on the flow rate. The change in volume is as noticeable as the change in flow rate. According to these results, the error rate in non-Newtonian liquids confirmed the inaccuracy of the single function method in the drop counting method.

Table 2 Measured Volume Results

Reference Flow Rates (mL/h)	Reference Volume (mL)	Measured Volume (mL)	Error Rates (%)
25	50	51	2,0
50	50	50	0
100	50	50	0
200	50	48	4,1
250	50	47	6,3
500	50	45	11,1
750	50	43	16,2
1000	50	41	21,9
1250	50	39	28,2

In optically constructed systems, even though the most accurate method is to create flow rate and volume data starting from drop volume measurement, as in KAMBLE et al.'s study, by specifying the gradual flow range (Stage-1: 0-100 mL/h, Stage-2: 100-1000 mL/h), flow and volume data can be measured with high accuracy by the 2-function drop counting method.

CONCLUSION

In this study, it is seen that measurements should be made with mechanical pump systems or electronically controlled volume measurement systems. Especially in low-flow applications, critical situations may occur as a result of people consciously or unconsciously tampering with the serum speed. In order to prevent these situations, it is important that the system is monitored correctly and the measurement is accurate. As seen in the Table 3, it is necessary to think about the advantages and disadvantages of the systems and to use the right system at the right time.

Table 3 Infusion Types Comparison Charts [1]

	Gratity-Based Flow	Peristaltik/Casette Type Pump- Syringe Pump
Infusion Category	Macroinfusion	Macroinfusion/ Microinfusion- Microinfusion
Ease of Use	Basic Set/ No External Components	Use of External Components is Mandatory / Having to Adjust at Every Startup
Costing	Low Cost	High Cost- Mid Cost
Flow Sensitivity	Low	High- Very High
Volume Sensitivity	Low	High- Very High

Gravity-based flow infusion systems are the simplest systems in terms of ease of use and accessibility. Using gravity-based infusion systems configured to increase sensitivity will be suitable for both the patient and the administering team. Although there are many alternatives for configuration, optical monitoring systems are cost-effective and accessible due to their non-contact measurement ability and reusable feature. Thus, a technology that can be used by everyone who needs treatment is created.

In IV applications, adding RF (WiFi, SubGhz, etc.) communication systems to the architecture for data transfer and recording of the transferred data in systems aimed at monitoring the operations performed with optical or other types of detection, both for verifying the information by the patient and for detecting negative situations on the practitioner's side, results in more functional products. Thanks to this method, both patient rights and practitioner rights will be protected legally.

References

1. Kim, U. R., Peterfreund, R. A., Lovich, M. A. Drug infusion systems: Technologies, performance and pitfalls in Anesthesia and Analgesia. Lippincott Williams and Wilkins. 2017;124(5):1493–1505.
2. Flack, F. C., Whyte, T. D. Variations of drop size in disposable administration sets used for intravenous infusion. J. Clin. Path. 1975;28:510-512.
3. Stoneham, M. D. An evaluation of methods of increasing the flow rate of i.v. fluid administration. British Journal of Anesthesia. 1995;75(3):361–365.
4. Singh, S., Randle, L. V., Callaghan, P. T., Watson, C. J. E., Callaghan, C. J. Beyond Poiseuille: Preservation Fluid Flow in an Experimental Model. Journal of Transplantation. 2013;1:1-6.
5. Tolman, R. C. The effect of droplet size on surface tension. The Journal of Chemical Physics. 1949;17(3): 333–337.
6. La Cour D. Drop size in disposable sets for intravenous infusion. Acta Anesthesiol Scand. 1965;9:145-154.

7. Hillman, M. R. The prediction of drop size from intravenous infusion controllers. Journal of Medical Engineering & Technology. 1989;13(3):166-176.
8. Murphy, R. S., Wilcox, S. J. High risk infusions - Accuracy compromised by changes in patient venous pressure. Journal of Medical Engineering and Technology. 2009;33(6):470–474.
9. Pierce, E. T., Kumar, V., Zheng, H., Peterfreund, R. A. Medication and volume delivery by gravity-driven micro-drip intravenous infusion: Potential variations during "wide-open" flow. Anesthesia and Analgesia. 2013;116(3):614–618.
10. Ogawa, H., Maki, H., Tsukomoto, S., Yonezawa, Y., Amano, H., Caldwell, W. M. A New Drip İnfusion System with A Free-Flow Detection. IEEE Staff, & IEEE Staff. 32nd Annual International Conference of the IEEE Engineering in Medicine and Biology Society. 2010;1:1214-1217.
11. Bhavasar, M. K., Nithya, M., Praveena R., Bhuvaneswari, N. S., Kalaiselvi, T. Automated Intravenous Fluid Monitoring and Alerting System. IEEE International Conference on Technological Innovations in ICT for Agriculture and Rural Development. 2016;1:77-80.
12. Arfan, M., Lavanya, R. Intravenous (IV) Drip Rate Controlling and Monitoring for Risk-Free IV Delivery. International Journal of Engineering Research & Technology (IJERT). 2020;9(9):967–971.
13. Kamble, Vidyadhar V., Pandey, Prem C., Gadgil, Chandrashekar P., Choudhary, Dinesh S. Monitoring of Intravenous Drip Rate. Proceedings of ICBME. 2001;1:51-55.
14. Tanwar, S., Maniktalia, R., Billa, R. IoT Based Drip Infusion Monitoring System. International Journal of Science and Research. 2021;10(12):752-757.
15. Cahyanurani, A., Hadiyoso, S., Aulia, S., Faqih, M. Design and development of a monitoring and controlling system for multi-intravenous infusion. International Journal of Engineering Research & Technology (IJERT). 2019;9(9):967-971.

HITTITE JOURNAL OF SCIENCE AND ENGINEERING

e-ISSN: 2148-4171
Volume: 11 • Number: 2
June 2024

Investigation of Barrier Effectiveness and Comfort Properties of Biodegradable PLA Nonwoven Fabrics Coated with Unmodified Lignin/Water-Borne Polyurethane Composite Coatings

Gülçin Baysal
Research-Development, Technology Management and Innovation Unit, Eskisehir Technical University, 26555, Eskisehir, Türkiye

Corresponding Author

Gülçin Baysal
E-mail: g_baysal@eskisehir.edu.tr Phone: +90 507 552 5508
RORID: https://ror.org/00gcgqv39

Article Information

Article Type: Research Article
Doi: https://doi.org/10.17350/HJSE19030000334
Received: 21.03.2024
Accepted: 23.05.2024
Published: 30.06.2024

Cite As

Baysal G. Investigation of Barrier Effectiveness and Comfort Properties of Biodegradable PLA Nonwoven Fabrics Coated with Unmodified Lignin/Water-Borne Polyurethane Composite Coatings. Hittite J Sci Eng. 2024;11(2):77-88.

Peer Review: Evaluated by independent reviewers working in at least two different institutions appointed by the field editor.
Ethical Statement: Not available.
Plagiarism Checks: Yes - iThenticate
Conflict of Interest: The author declares that there is no conflicts of interest concerning the content of this article

CRediT Author Statement:
Gülçin Baysal: Conceptualization, Methodology, Analysis, Investigation, Writing-review and Editing

Investigation of Barrier Effectiveness and Comfort Properties of Biodegradable PLA Nonwoven Fabrics Coated with Unmodified Lignin/Water-Borne Polyurethane Composite Coatings

Gülçin Baysal

Research-Development, Technology Management and Innovation Unit, Eskisehir Technical University, 26555, Eskisehir, Türkiye

Abstract

In this study, the main aim is to prepare unmodified lignin/water-based polyurethane (WPU) composite coatings with varying lignin concentrations and apply them to polylactic acid (PLA) spunlace nonwoven fabrics (PNFs). The effects of lignin concentrations were investigated in terms of color values, hydrophobicity, air permeability, and antibacterial properties of PNFs. The analysis of chemical groups in the structures of lignin/WPU composite films after curing was performed using Fourier Transform-Infrared (FTIR) spectroscopy, and their thermal properties were analyzed by Differential Scanning Calorimetry (DSC) and Thermogravimetric Analysis (TGA). The coatings applied to the fabrics were examined by scanning electron microscopy (SEM) through surface images. The fabric coated with the X4 formulation, containing 4% concentration of lignin, displayed the highest water contact angle recorded at 93.6º. As the lignin concentration increased, the air permeability of the fabrics decreased. Regarding color measurements, the PNF sample coated with the X4 formulation showed the highest K/S value of 7.45. In antibacterial activity tests, no inactivation was observed against E.coli bacteria. However, inhibition zone measurements against S. aureus bacteria were 12±1.41 mm and 16.05±0.7 mm on fabrics coated with X3 and X4 formulations having lignin concentration 2% and 4%, respectively. The results indicated that an increase in lignin concentration effectively contributed to the inactivation against S. aureus bacteria. In this respect, this study represents the potential usability of unmodified lignin/WPU coatings providing barrier and comfort properties on biodegradable PNFs.

Keywords: Polylactic acid, Biodegradable, Nonwoven fabric, Composite coatings, Water-borne polyurethane, lignin.

INTRODUCTION

The contemporary textile landscape is witnessing a growing demand for innovative fabrics that prioritize health and well-being, aligning with advancements in material innovation, emerging technologies, and fashion trends (1). While traditional textiles have successfully met primary quality criteria such as biocompatibility, flexibility, and strength, there is a growing demand for textiles with specific functions. Textiles inherently harbor bacteria and fungi, necessitating measures to control their growth. Barrier textiles play a crucial role in environments with a high risk of contamination from infectious or toxic materials, particularly in surgical procedures. Their protective function is achieved through the design and construction of fabrics that shield users from fine particulate matter or liquids. Key qualities include the filtration of medically relevant substances like blood, sweat, and urine. Medical laminates, comprising porous membranes, tissues, and absorbers, limit fluid exchange through capillary flow. Microfiber textiles have proven effective for reusable protective clothing, with nonporous membranes offering the highest level of protection. However, a practical compromise must be struck between barrier function and wearer comfort (2). With the rapid developments in the technical textile sector in recent years, interest in functional textiles has increased. Given the growing importance of sustainability, there is a focus on examining the applicability of natural and biodegradable finishing/coating systems to impart functional effects to textile materials (3,4). During the Covid-19 epidemic, research has been concentrated on the production of bio-based or compostable medical masks, gowns, covers, etc. In addition to these products, there is a focus on developing clothes suitable for daily life. These items are designed to have protective, bactericidal, and virucidal effects (5).

Nonwoven fabrics are utilized in various industrial sectors, including healthcare, agriculture, construction, automotive, aerospace, and more (6). The raw materials commonly used in the medical textile field for nonwoven fabrics are synthetic polymers, such as polypropylene (PP) and polyethylene (PE). Fabrics made from these polymers are not biodegradable in the natural environment, causing environmental issues worldwide (7). The development of nonwoven fabrics is crucial for the production of biodegradable, hygienic, and environmentally friendly sustainable products. Biodegradable polymers play a significant role in this regard, offering a solution to reduce the synthetic waste generated by the textile industry. In recent years, polylactic acid (PLA) has emerged as a natural, biodegradable, and sustainable polymer (5,8) Accordingly, researchers are ongoing with studies on the applicability of hydrophobic and antibacterial finishing/coating on biodegradable PLA nonwoven fabrics. However, the development and application of these functional and protective coatings pose difficulties due to the poor mechanical performance of such natural fabrics (6).

In this way, the possibility of using lignin in functional textiles as an antimicrobial agent has been the subject of research. The lignin polymer exhibits antibacterial activity thanks to the functional phenolic hydroxyl groups in its structure. During this antimicrobial activity, chemical groups inhibit growth by damaging the cell membrane of bacteria, causing hydrolysis and subsequent release of cell contents (9).

Edible films and coatings consist of proteins and polysaccharides present several advantages, including biodegradability, edibility, biocompatibility, aesthetic appeal, effective barrier properties, non-toxicity, environmental friendliness, and cost-effectiveness, as opposed to those derived from synthetic polymers(10–12) Composite films, incorporating both lipid and hydrocolloid components, have also been formulated. Coating technologies relying on aqueous systems, foam coating, hot melt, or warm melt systems are gaining prominence over older solvent coating processes due to their reduced environmental impact. The development of microporous and hydrophilic polyurethane coatings, along with lamination techniques, has enabled the creation of waterproof and 'breathable' fabrics. The current surge in interest in nano-science and nanotechnology has sparked considerable excitement around nanocoating (10).

Polyurethane (PU) stands out as one of the most versatile polymers in the industry, finding applications in various products like coatings, flexible foams, and elastomers. Polyurethanes (PUs) are highly versatile synthetic polymers widely employed in medical, automotive, and industrial applications. They serve various purposes in furniture, coatings, adhesives, construction materials, fibers, padding, paints, elastomers, and synthetic skins, with a notable presence in the coating industry. PU resins exhibit excellent properties, including abrasion resistance, adhesion, corrosion resistance, weather resistance, low-temperature flexibility, toughness, and superior mechanical strength (13). In the coatings industry, PUs are an important class of polymers due to their good mechanical, chemical, and physical properties. In recent years, there has been significant growth in the development of environmentally friendly water-based polyurethane dispersion (WPUD) products with low toxic properties. These can be used instead of solvent-based PUs containing volatile organic compounds (VOCs) that are harmful to the environment and human health. These environmentally friendly PU systems are employed in paint and pigment systems, drug carrier systems, anti-corrosion, antibacterial, and mechanically resistant coatings, making them important sustainable and environmentally friendly systems in the textile industry. WPUDs exhibit good flexibility, tensile and impact strength. In some studies in the literature, it is reported that various fillers can be added to polymers to enhance the thermophysical and mechanical properties of WPUs, and desired functional properties can be incorporated into the structure (14). Recently, lignin has attracted considerable research interest as a natural polymeric antioxidant and a key ingredient for sustainable materials. Its biodegradability, renewability, wide availability, and remarkable stability have led to extensive study. Researchers are actively exploring lignin's potential in various applications, aiming to utilize its properties for advancing eco-friendly materials and technologies (15,16). The functional groups in the lignin structure can form hydrogen bonds with the urethane groups in PU. By incorporating lignin or lignin-derived natural materials, the mechanical properties of water-based polyurethanes (WPUs) can be improved. This enhancement enables the utilization of PU-based film/coating systems in a wide range of applications that demand durable functional materials, including biomedical, food packaging, automotive interiors, and outdoor applications (16,17). Lignin has high potential for use in lignin-based coating systems where thermal properties and stability are desired, and its usability has been investigated in various fields such as textiles, wood products, non-woven fabric, and packaging systems (18). Lignin, a lignocellulosic material, has been used as a filler to enhance the mechanical and functional properties of polymers (19). The chromophoric, phenolic, ketone, and auxochromic structures in lignin provide effective antimicrobial activity against bacteria and fungi (18,20). The antimicrobial mechanism that lignin can provide is not adequate due to the uneven distribution of the macromolecular size of lignin and the basic monomers of p-coumaryl alcohol, coniferyl alcohol, and sinapyl alcohol in the structure. On the other hand, the coniferyl alcohol and sinapyl alcohol structures, which are basic monomers, have inhibitory properties against microbes (21). Typically, coatings containing lignin exhibit water contact angles (WCAs) of approximately 80°, with 90° commonly regarded as the threshold for defining a surface as hydrophobic (22). Despite its considerable potential to improve the hydrophobicity, antibacterial activity, and breathability of textiles, there is a scarcity of research on the application of water-based WPU binders, including lignin, as coating/finishing materials (16,19,23).

In one study, the aim was to develop waterproof and breathable fabrics by applying isophorone diisocyanate (IPDI) and a water-based polyurethane (WPU) coating paste containing lignin as an antioxidant material to polyester fabrics using the direct knife coating technique (15). In a separate study, Li et al. employed lignin as a substitute raw material instead of polyhydroxyl components in synthesizing PU macromolecules (24). Zimniewska et al. conducted research on developing nonwoven fabrics that offer functional effects by using nano-lignin-containing coatings (25). They prepared formulations using binding materials, such as kraft lignin-containing silicone emulsion or acrylic dispersion, through an ultrasonic process and applied them to the fabrics. The study revealed that the coating was effective in enhancing the UV protection, antistatic, and antibacterial properties of the fabrics (25,26). Sunthornvarabhas and his colleagues have researched the antimicrobial effects on nonwoven fabrics using lignin obtained from sugarcane. They found that solutions containing lignin transferred onto nonwoven fabrics reduced bacterial colonies on the fabrics due to the increasing concentration of lignin (27). In addition, in another study by this research group, it was reported that a lignin-based coating is more economical for antibacterial activity than coatings using inorganic particles, and lignin is a material with high potential for antimicrobial, antioxidant, ultraviolet protection, and flame-retardant properties. Although it has been accepted that lignin is a natural, biodegradable antioxidant material that can provide antimicrobial and UV protective effects, the potential production of lignin-coated or finished fabrics has not been widely accepted, and scientific reports on this subject are insufficient. This may be due to the fact that lignin is not recognized as a natural antimicrobial agent by both consumers and manufacturers, attributed to its natural dark brown color (21).

In the existing literature, there are limited research on lignin/WPU composite coatings and their utilization in textile applications. In the previous research, the effect of modified lignin concentration in lignin/WPU composite formulations on the mechanical properties as well as the UV attributes of nonwoven fabrics was studied. The earlier research utilized three-chloro-2-hydroxypropyltrimethylammonium chloride (CHPTMAC), a compound that introduces a positively charged quaternary ammonium group$(NR_4)^+$ into the lignin structure, thereby augmenting its solubility in water (28). This research presents the initial exploration into employing unmodified lignin as functional biopolymer with WPU on coating of PNF and evaluating the antibacterial activity, barrier performance, and comfort properties of textiles. To achieve this objective, various lignin/WPU formulations with differing concentrations of unmodified alkali lignin were prepared. These formulations were subsequently applied onto PNF using a film applicator, followed by thermal curing, and their suitability for PNF was assessed. The characterization studies of lignin/WPU films were conducted through FTIR spectroscopy, TGA, and DSC analyses. Surface analysis of lignin/WPU-coated fabrics was conducted via SEM analysis to examine lignin distribution.

MATERIAL AND METHODS

In this study the base nonwoven fabric type and materials used for preparing WPU/lignin formulations were given in Table 1.

Preparation of WPU Coating Formulations

Water-borne composite coating pastes (solid content: 45%), including WPU binder, unmodified alkali lignin with four different concentrations (1.0%, 1.5%, 2% and 4%) and other additives, e.g. wetting agent, defoamer, thickener and ammonia solution, were prepared as reported in previous study (28). Materials amounts used in this study were given in Table 2. These coating formulations were applied to fabrics using a film applicator (BGD 206/4, Hedef Kimya, Türkiye), which provides homogeneous and adequate coverage on the fabric surface (Fig. 1). Coated fabrics were cured thermally at 135 ºC for 5 minutes. In this study, the curing time in which the fabric form is preserved, and the fixing process is most appropriate was determined as 5 minutes by preliminary studies and was applied for all formulations.

Table 1 Nonwoven fabric type and materials used for preparing lignin/WPU formulations.

Materials	Product name and supplier
PLA spunlace nonwoven (fabric weight of 50 g/m²)	Mogul Tekstil, Türkiye
Aliphatic polyether anionic waterborne polyurethane dispersion, 60% solid content	Witcobond® 358-90, Lanxess, Germany
Lignin alkali, UV absorber biopolymer	Merck, Germany
Nonionic waterborne blocked isocyanate crosslinker	RUCO®-COAT FX 8041, Rudolf Duraner, Bursa, Türkiye
Wetting agent	NC WET 1200, NC İstanbul Kimyevi Ürünler, Türkiye
Thickener	Pigmacolor Pigmapol PF, Kemiteks, Türkiye
Defoamer	Pigmacolor HC, Kemiteks, Türkiye
Ammonium hydroxide solution	NH_4OH, Kimetsan, Türkiye
Distilled water	

Fourier Transform Infrared (FTIR) Spectroscopy

Various formulations were created, each with different concentrations of lignin, and films approximately 120 µm thick were applied onto glass plates sized 3x120x120 mm using a film applicator. Following this, the films underwent thermal curing at 135°C for 5 minutes. The chemical composition of the films, extracted from the glass plates, was then examined using FTIR spectroscopy (VERTEX 70v Bruker, Germany). FTIR spectroscopy scans were performed across the wavelength range of 400-4000 cm^{-1} with a resolution of 4 cm^{-1} to analyze the thermally cured films.

Differential Scanning Calorimetry (DSC)

The thermal characteristics of cured films were assessed in a nitrogen atmosphere using DSC device (Q20, TA Instruments). Fabric samples weighing approximately 4-5 mg were prepared and housed in aluminum pans for analysis. DSC analysis was conducted in the range of 25°C to 500°C at a heating and cooling rate of 10°C/min. Throughout the analysis, DSC thermograms of the fabric samples were generated. Initially, the sample was heated from 25°C to 500°C at a rate of 10°C/min and maintained at this temperature for 3 minutes

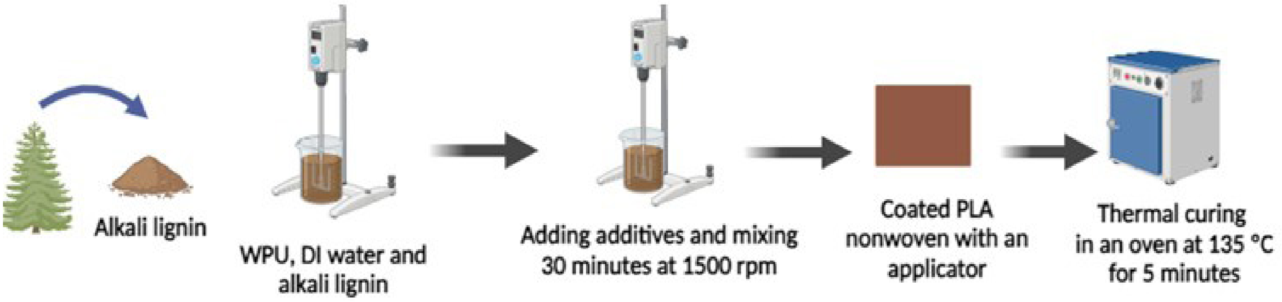

Figure 1 Preparation stage of lignin/WPU composite coating formulations and coating process of PNF.

Table 2 Water-based coating formulations

Code	DI Water	WPU binder	Unmodified lignin	Blocked Isocyanate	Thickener	Dispersing Agent	Defoamer	Ammonia Solution
X	18.61	75	0	2	2.63	0.75	0.46	0.55
X1	18.61	75	1	2	2.63	0.75	0.46	0.55
X2	18.61	75	1.5	2	2.63	0.75	0.46	0.55
X3	18.61	75	2.0	2	2.63	0.75	0.46	0.55
X4	18.61	75	4.0	2	2.63	0.75	0.46	0.55

to eliminate any thermal or mechanical transition traces in the fabric material. Subsequently, the sample was cooled to 25°C at a cooling rate of 10°C/min, concluding the analysis. This procedure was repeated to acquire DSC thermograms for all fabric samples.

Thermogravimetric Analysis (TGA)

The thermal resilience of the films was examined using a TGA apparatus (Exstar SII TG/DTA7300) under a nitrogen atmosphere. The assessment was carried out at a flow rate of 50 ml/min and a heating rate of 10 ºC/min across the temperature span of 25 to 800 °C (29).

Scanning Electron Microscopy (SEM)

The SEM images of uncoated and coated fabrics were captured utilizing SEM device (FE-SEM, Hitachi, Regulus 8230) operating at 10.0 kV with a magnification of x100. Before observation, a thin layer of gold was deposited onto the fabric's surface to provide the electrical conductivity of the fabric samples.

Color Measurements

To assess the photometric attributes of the thermally treated PLA nonwoven fabric samples after coating, the CIE Lab* color values were acquired using a spectrophotometer (X-Rite, CI7800, Switzerland). The CIE L*a*b* color space has a lightness/darkness component (L*), a* component (green-red axis), and b* component (blue-yellow axis). Values of the L* component can be obtained in the range from 0 to 100 (0-black, 100-white). C* (chroma) refers to the saturation of the color at a certain L* value, and h° (hue) refers to the shade of the color. The ratio between absorption coefficient (K) and scattering (S) is known as color yield and is calculated with the following equation (1)(30).

$$\frac{K}{S} = \frac{(1-R)^2}{2R} \tag{1}$$

Surface Wettability Measurements

The surface wettability of the different samples was characterized via measuring water contact angle (WCA), which is a quantitative measure of the wetting of a solid with a liquid. The device of choice for measuring contact angles and dynamic contact angles is an optical tensiometer(31). The contact angle is an indicator that provides an understanding of the wettability properties of the materials and therefore is effective in determining the waterproof properties of the materials(32). The hydrophobic character of PNF fabrics was determined by an optical tensiometer device (Attension Theta Flex, Biolin Scientific, Sweden). The fabric specimens were sectioned as 2 cm^2 and affixed to the glass surface using double-sided tape. Subsequently, a droplet of 5 µL distilled deionized water was dispensed onto the fabric from a micro-syringe, and images were taken to quantify the angle established at the interface between the liquid and solid phases. The CA left and right measurements was conducted after the drop release (CA-T$_{0\text{-}10}$ sec) and mean CA values were calculated. Each sample was measured on five different points and the average values were calculated.

Air Permeability Measurements

The air permeability properties of PNFs were evaluated using an air testing apparatus (MO21A, SDL ATLAS, Switzerland) according to the specifications outlined in TS 391 EN ISO 9237 "Determination of air permeability of textile fabrics." This procedure entails measuring the volume of air passing through 1 m^2 of fabric per minute under a water pressure head of 10 mm. Air permeability tests were applied to 20 cm^2 uncoated and coated fabric samples with 100 Pa pressure increase and recorded in l/m^2/s (33).

Antibacterial Activity

The effect of lignin concentration on the antibacterial activity of WPU/lignin coated PNFs was investigated against gram-positive (Staphylococcus aureus: ATCC 25923) and gram-negative (Escherichia coli: ATCC 25922) bacteria using agar disc diffusion method according to test standard of PN-EN ISO 20645:2006 (34). The susceptibility of bacteria to antibiotics was determined on MH (Mueller Hinton) agar by Kirby–Bauer disk diffusion technique. Sterile loops were employed to retrieve samples from the bacterial colonies that had developed as distinct entities on the culture plates. These samples were then introduced into MH broth and allowed to incubate for a period of 1-2 hours at 37ºC. Once turbidity became evident, a standardized level of turbidity was achieved by calibrating to McFarland 0.5 (equivalent to 108 microorganisms/ml). This resulting suspension was subsequently used for broad-spectrum cultivation on MH agar medium using a sterile swab. WPU/lignin coated fabrics prepared as 1 cm2 were placed in the medium with sterile forceps. Gentamisin was used as a positive control. After incubation of petri dishes at 35-37ºC for 18-24 hours, inhibition zone diameters were measured.

RESULTS AND DISCUSSIONS

Fourier Transform Infrared (FTIR) Spectroscopy

The presence of chemical groups in the FTIR spectra of the clear WPU film (formulation X) and lignin/WPU polymeric films (formulations X1 and X4, with 1% and 4% lignin concentrations, respectively) was identified by absorption peaks (Fig. 2). Examination of the FTIR spectra of films prepared at different lignin concentrations revealed the original functional groups of WPUs. C-O-C stretching absorption peaks at 1236 cm^{-1} were observed, as expected. In the X4 formulation with a high lignin concentration, the intensity of these peaks slightly increased in the spectrum due to interactions between lignin and WPU (35). The stretching vibration peak, which represents the ester group, occurred at 1720 cm^{-1} peak in all polymeric films (29). During FTIR analysis, a higher transmittance percentage at a specific wave number in the spectra obtained from the cured film sample indicates a limited presence of functional bonds within the polymer material structure. These bonds absorb light emitted from the device to the sample. Thus, the reduction in transmittance percentage is associated with the formation of a cross-linked polymer structure due to thermal curing (36).

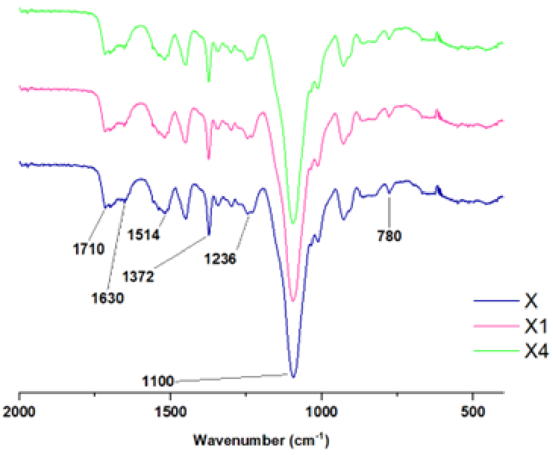

Figure 2 FTIR spectra of thermally cured films.

Differential Scanning Calorimetry (DSC)

DSC analysis results of thermally cured films were given in Table 3. In Table 3, DSC analysis results of X, X1 and X4 films prepared with %0, 1.0 % and 4.% lignin concentrations, respectively were given. According to the results, the glass transition temperatures (Tg) and melting temperatures (Tm) of the films obtained with the X1 and X4 formulations prepared at 1% and 4% lignin concentrations, respectively, were higher than the Tg and Tm values of the films prepared with the lignin-free X formulation. The results show that more energy is required to break the interaction between lignin and WPU in lignin/WPU composite films prepared at high lignin concentration, and Tg and Tm values increase accordingly (29). DSC thermograms of X4 and X films were shown in Fig. 3.

Table 3 Thermal analysis results of cured unmodified lignin/WPU films.

Sample Code	T_g (°C)	$\triangle H_{mTg}$ (J/g)	T_m (°C)	$\triangle H_{mTm}$ (J/g)
X	323.53	26.43	396.02	56.50
X1	358.49	16.56	411.35	57.24
X2	359.30	17.56	412.24	67.30
X3	361.25	17.97	411.38	71.50
X4	365.42	18.43	413.82	80.53

Thermogravimetric Analysis (TGA)

TGA analyses were conducted to assess the impact of lignin concentration on the thermal stability of lignin/WPU composite films, with results presented in Table 4. The thermal degradation of lignin typically occurs in three stages. The initial step involves the separation of the ether bond, followed by dealkylation and cleavage of the C-C bond in the second stage. The final step entails carbonization demethylation. As the ether bonds break, carbonaceous structures undergo rearrangement to form more conjugated structures, leading to a high degree of graphitization through various cross-linking reactions (9). Lignin/WPU composite film prepared with X4 formulation containing 2% lignin exhibited better thermal stability than the film prepared with lignin-free X formulation and X1 film prepared with the formulation including 0.5% lignin. Initial decomposition and maximum decomposition temperatures were obtained as 305.15 °C and 419.13 °C for the X film, 312.12 °C and 428.73 °C for the X1 film, 341.33 °C and 446.51 °C for the X4 film. The increase in the initial degradation temperature seen in the composite film that incorporates lignin and WPU can be ascribed to the greater energy requirement needed to disrupt the molecular linkage between the lignin and WPU chains (29,37). According to the results obtained from the X4 film, the initial decomposition temperature of the film obtained from the lignin-free X formulation was 12% and maximum decomposition temperature increased by 6.5%. TGA curves of X4 and X films were shown in Fig. 4.

Table 4 TGA results of cured films.

Sample code	T_{onset}(°C)	T_{max} (°C)	Weight loss (%)
X	305.15	419.13	97.68
X1	312.12	428.73	96.33
X2	326.30	434.56	96.21
X3	336.56	444.22	93.50
X4	341.33	446.51	89.80

As seen in Table 4, as a result of using higher lignin concentration, the maximum decomposition temperature for the film prepared with X4 formulation was obtained as 446.51 °C and which is higher about ~27 °C than the maximum decomposition temperature of the X film (419.13 °C). Within the films crafted using the X, X1, and X4 formulations, weight losses of 97.68%, 96.33%, and 89.80% were observed, respectively. The incorporation of lignin enhanced the thermal resistance of these formulations and improved their stability, yielding an 8% decrease in weight loss for the X4 formulation when contrasted with the X formulation.

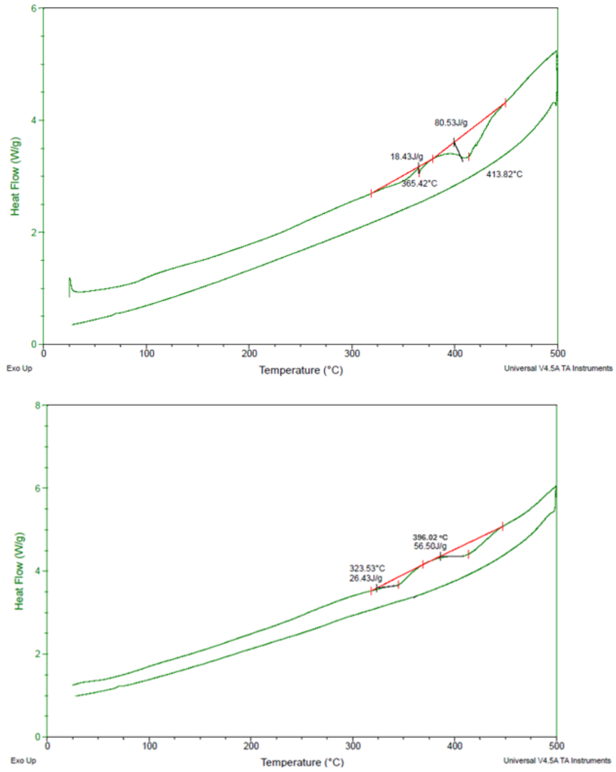

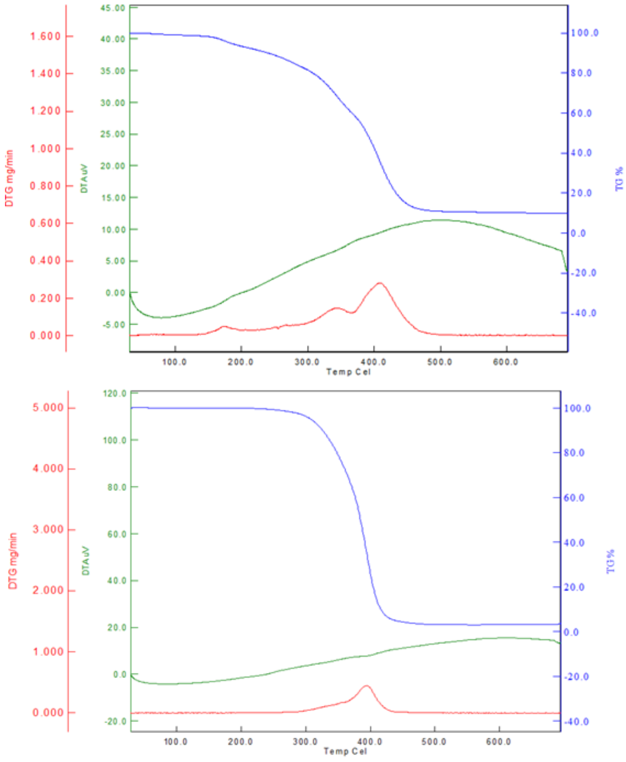

Figure 4 TGA curves of a) X4 and b) X films.

Scanning Electron Microscopy (SEM)

FE-SEM images of thermally cured PNFs prepared with formulations X, X1 and X4 containing lignin at different concentrations were given in Fig. 5.

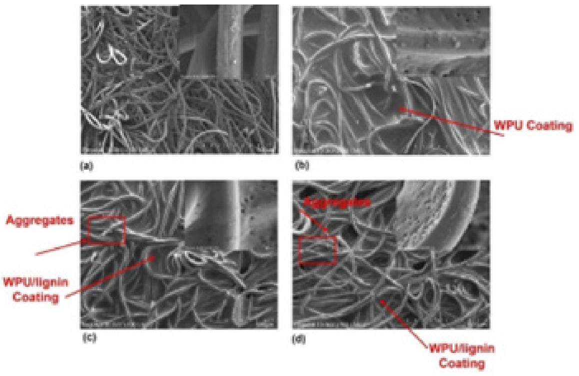

Figure 5 FE-SEM micrographs of (a) uncoated fabric, (b) X (WPU), (c) X1 (L/WPU 1%), (d) X4 (L/WPU 4%).

SEM images of coated and thermally cured PNFs were compared with the image of pure PNF. When the FE-SEM images are examined, it is seen in Fig. 5(a) that the uncoated nonwoven fabric structure has a porous network structure and has a rough, uneven surface due to the entanglement of the fibers. In Fig. 5(b), it was observed in the surface image of the PNF, coating formulation filled the spaces between the fibers and the surface had a more homogeneous structure. The surface appearance of fabrics coated with formulations X1 and X4 containing 1% and 4% lignin, respectively, were given in Fig. 5(c) and Fig 5(d). The gaps between the fibers in the fabric structure are filled with coating material to a large extent. The function of the fillers used in hybrid coatings prepared with the combination of different materials depends on the uniform distribution of these materials in the polymer(38). Therefore, the distribution of WPU-based coatings containing different concentrations of lignin on the fabric surface was evaluated with FE-SEM images. As a result of the application of WPU/lignin coatings and pure WPU coating paste to the fabric surface, the surface images were examined comparatively (Fig. 5(c)–(d)). It can be seen from Fig. 5 (b) that the surface of the pure WPU coated and thermally cured PNF fabric is more homogeneous and the gaps between the fibers are filled with coating paste. Some differences were observed in the appearance of the coating applied to the fabric with the incorporation of lignin particles into the WPU dispersion. A restricted number of white dots, highlighted by red rectangles in the images, became evident on the surface of the PNFs coated with WPU/lignin coating (Fig. 5(c)-(d)). As can be seen, the lignin particles were almost evenly dispersed in the WPU dispersion, only minor agglomerations were observed in some parts. The lignin included in the formulation filled the space between the fibers to reduce surface porosity. At the meantime lignin can expose the hydrophobic surface to resist moisture(39). The homogeneous coating formed on the fabric surface with the increase in lignin concentration, given the surface a hydrophobic feature, also supported this by the WCA measurement results. The lignin added to the WPU dispersion increased the adhesion between the fiber and the binder, therefore strengthened the interaction between the layers forming the multilayered networks. Aggregations formed by the addition of lignin to the WPU dispersion can be associated with the density of hydroxyl groups in the medium due to the increased lignin content(40). In Fig. 5(c) and Fig.

5(d), it can be observed that the lignin particles are evenly dispersed in the WPU. This homogeneous dispersion may result from a balanced adjustment of the mixing speed and time of WPU/lignin dispersion(41). It can be seen from Fig. 5(d) that the 4% by weight lignin in the coating paste appears to clump together in some areas. This is due to the fact that the high concentration of lignin flocculates to form large particles during mixing in the WPU. There is an obvious phase interface between the lignin particles and the WPU resin. The low lignin content WPU/lignin coating and WPU coating are very homogeneous and the agglomerated lignin particles are very few in the 1% lignin content coating, indicating a homogeneous structure of the WPU coating(42).

Color Properties of Coated PNFs

The results of CIEL*a*b* color values were given in Table 5. One of the problems encountered with the application of lignin in WPU materials is the dark color of lignin due to its natural structure, which can limit some applications such as coatings(43). Lignosulfonate staining results in color alteration during the dyeing procedure, and managing this staining is challenging. Sulfonated kraft or alkali lignin obtained from pulping processes tend to contain a higher concentration of chromophores, leading to a deeper coloration(18).

Table 5 CIEL*a*b* color value results of coated PNFS.

Sample code	L^*	a^*	b^*	C^*	h°	K/S
X1	81.09	7.57	37.66	38.41	78.64	2.78
X2	77.03	10.21	39.25	41.36	72.26	6.7
X3	63.29	16.73	44.38	47.43	69.34	7.12
X4	49.14	19.88	30.13	36.10	56.59	7.45

In its natural state within wood, lignin appears nearly colorless; however, industrial variations like alkali lignin or lignosulfonate exhibit a deeper hue. The creation of chromophores is a consequence of both the extraction of lignin and the pulping processes; however, the precise mechanism behind their development remains uncertain. Several recognized chromophore configurations encompass: (1) aromatic rings with conjugated carbon-carbon double bonds; (2) quinone methides and quinones; (3) chalcone structures; (4) unpaired electrons (free radicals); (5) metal complexes featuring catechol structures. The contents of the quinone methide and quinone structures are in low amount but contribute most of the lignin color. The deep hue exhibited by industrial lignin is also regarded as a limitation in the advancement and widespread adoption of products derived from lignin (44). Nevertheless, the inherent dark hue of technical lignin remains an obstacle in realizing its potential for enhanced value in various applications, such as dyestuff dispersants. To encourage the utilization of high value-added lignin, the crucial step involves achieving an acceptable light tint for the lignin (45). As shown in Fig. 4 (b) in this study, the color of the WPU coated nonwoven fabric changed in the dark direction as the amount of lignin increased. In fabrics coated with composite formulations, the L* light-darkness value of the fabric decreased with the increase in the lignin concentration in the coating paste, that is, the fabric changed to a darker color from light brown to dark brown. As the lignin concentration increased, the redness values (a*) of the fabric increased, the yellowness (b*) values decreased, and the K/S color yield values increased. Color tone values (h°) were observed in the region with high redness (a*) between a+ and b+ axes and close to the x-axis.

Wettability Measurements of Coated PNFs

In WCA measurements, the wettability properties of uncoated PNF and thermally cured PNFs that were coated with WPU/lignin formulations containing different concentrations of lignin were tested and the WCA results given in Table 6. The water repellency of the coated PNF surfaces was assessed by calculating the water contact angle (WCA) through the application of a water droplet on the fabric surface. The images captured using an optical tensiometer device are depicted in Fig. 6. As a result of the wettability test, the WCAs of the fabrics were determined and the hydrophobic and hydrophilic properties of the surfaces were evaluated. According to the test results, while the raw PLA fabric had a WCA of 109.7° and was measured as 26.2° for the pure PU coated PNF. The WCA value of lignin-free WPU coated fabric decreased considerably. This low WCA indicates that the surface has a hydrophilic character. In contact angle measurements, the size of the contact angle formed between the water droplet and the surface gives information about the hydrophobicity of the surface(46).

Table 6 Surface wettability measurements of fabrics; SD, standard deviation.

Samples	WCA left [°]	WCA right [°]	WCA mean [°]
PNF	110.3	109.2	109.7
PNF (± SD)	9.57	2.40	5.06
X	23.2	29.2	26.2
X (± SD)	3.15	31.8	15.6
X1	58.6	57.1	57.8
X1 (± SD)	4.7	4.5	4.6
X2	61.6	61.9	61.7
X2 (± SD)	5.7	5.5	5.6
X3	78.6	77.1	77.8
X3 (± SD)	5.7	6.5	3.6
X4	91.9	95.3	93.6
X4 (± SD)	8.3	5.1	6.0

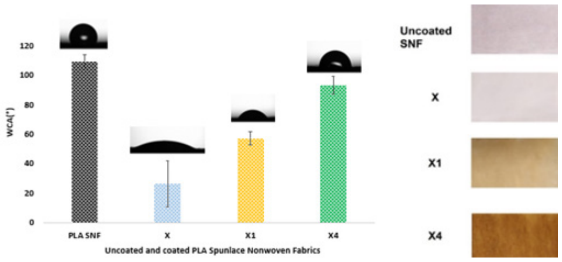

(a) (b)

Figure 6 (a) Water contact angles and (b) photographic images of fabrics.

The water absorption capacity and WCA at the surface are related to the energy of the surface and the pore size at the surface. The reduction in water absorption and the large degree of WCA behavior can be explained by the reduction of the pore size on the surface(47). In pure WPU coating, it can be said that the coating exhibits wettability due to the hydrophilic groups in the structure of WPU(48). It was observed that the hydrophobic properties of the coatings improved with the addition of lignin at increasing concentrations to the WPU-containing formulation. Upon integrating 1% lignin into the WPU formulation, a significant enhancement in the water contact angle (WCA) value on the lignin/WPU coated fabric surface was observed, reaching 57.8°. This value demonstrated a remarkable improvement of 95.5% compared to the WPU coating without lignin. The WCA of the coated fabric surface was measured as 93.6° when the lignin concentration was used at a low density such as 4% in formulation X4 which was the WCA is 64.7% higher than that of X1 formulation including 1% lignin. According to these results, the WCAs of lignin/WPU coatings increased gradually with the increase in lignin concentration and this improved the hydrophobic property of the pure WPU coatings. The formulation X4, containing 4% lignin concentration, achieved the highest WCA value of 93.6°. These findings indicate the effective hydrophobic capability of the lignin/WPU coatings, primarily owed to the inherent qualities of lignin within the WPU formulation(49,50). The water contact angles (WCAs) of coatings containing lignin typically range around 80°. A threshold of 90° is often used to categorize a surface as hydrophobic (22). Lignin can form a moisture resistant hydrophobic surface by capping the hydrophilic groups in WPU. It can be said that the uniform and dense coating formed with hydrophobic lignin particles dispersed in the WPU matrix on the PNF surface provides good barrier properties against water with a WCA value of 93.6° (39).

Air Permeability Measurements of Coated PNF

The results of air permeability properties for thermally cured fabrics were presented in Table 7. SEM images (see Fig. 5(a)) reveal that the PNF exhibits a porous and open structure.

Table 7 presents the air permeability results. The neat PLA nonwoven fabric, with its open porous structure, exhibits high air permeability, measured at 1287 l/m^2/s. Coating the fabric with lignin/WPU composite formulations yields varied air permeability: 290 l/m^2/s for the X1 formulation containing 1% lignin and 142 l/m^2/s for the X4 formulation containing 4% lignin. This coating facilitates the formation of a denser cross-linked structure between the PLA fibers and the lignin/WPU composite coating, effectively closing gaps between fibers (51). The comfort aspects of wearable devices are influenced by intricate interplays among fabric permeability, flexibility, climatic conditions, physiological responses, psychological factors, and design attributes. Clothing comfort can be influenced by a blend of variables, including temperature, humidity, air circulation, and analogous elements. Due to the desired protective feature of medical gowns used in the medical textile category, air permeability is the main determining feature for wearing comfort. In most cases, medical gowns designed for superior liquid barrier performance tend to exhibit low air permeability but are often uncomfortable due to their limited air permeability(52). A surgeon working at a moderate pace at 20 °C will feel comfortable in his/her surgical clothing, provided that the fabric has an air permeability of at least 100 l/m^2/min (53). The structure of the coating paste restricts air passage by closing available voids in the fabric structure, leading to decreased breathability values with increasing lignin concentration in PNFs coated with lignin/WPU composite formulations (54,55).

Antibacterial Activity Analysis of coated PNFs

In the antibacterial activity analysis, uncoated (control sample) and coated fabrics were tested against to E. coli and S. aureus. While PNF coated with lignin/WPU formulations did not show antibacterial activity against E. coli bacteria, the sample containing 2% and 4% lignin showed antibacterial activity against S. aureus bacteria. Diameters of inhibition zones were measured as 12±1.41 and 16,05±0.7 mm against S. aureus bacteria in PNF coated with X3 and X4 formulations, respectively (Fig. 7). The antibacterial potential of lignin arises from its phenolic structure, which also serves as the primary origin of its antioxidant capabilities. Typically, gram-negative bacteria exhibit greater resilience to lignin compared to gram-positive counterparts, although this tendency can be influenced by the specific structural attributes of lignin. However, the documented antibacterial efficacy of lignin generally falls short of that achieved by commercial antibiotics. Studies concerning the antifungal and antiviral effects of lignin are scarce. Consequently, further research is imperative to enhance and optimize lignin's antimicrobial properties (56).

Lignin has antioxidant properties to protect against possible risks of free radical species (ROS). It exhibits notable antimicrobial effectiveness against both bacteria and fungi. The varying degrees of responsiveness between Gram-positive and Gram-negative bacteria to antibacterial agents can be attributed primarily to the divergent cellular compositions of these bacteria. Gram-negative bacteria possess cell membranes composed of lipopolysaccharides, lipids, and proteins, caused in a more confined scope of inhibition. As a result, greater efficacy in terms of antimicrobial action can be observed against S. aureus, a Gram-positive bacterium, in comparison to E. coli (6).

Table 7 Air permeability values of thermally cured fabrics coated with lignin/WPU composite formulations.

Sample code	Uncoated PNF	X1	X1	X3	X4
Air permeability (l/m^2/s)	1287	290	265	238	142
CV (%)	3.6	10.0	8.0	11.0	10.1

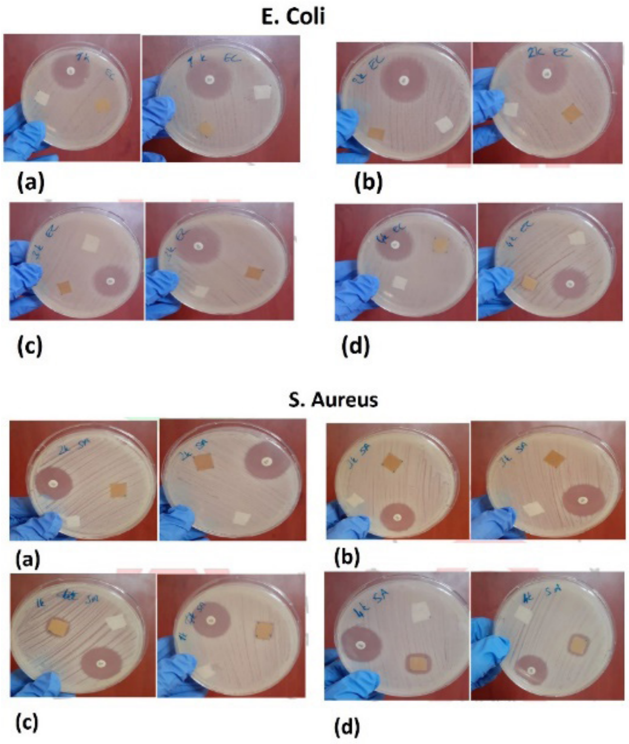

Figure 7 Diameters of inhibition zones of uncoated white PLA nonwoven fabrics (X) and light brown fabrics coated with a) X1, b) X2, c) X3 and d) X4 formulations against to E.coli and S. aureus bacteria.

CONCLUSION

This study involved the preparation and successful application of unmodified lignin/WPU composite coating formulations, featuring four distinct lignin concentrations, onto PNFs. According to color measurement results, it was observed that increasing lignin concentration in the lignin/WPU formulations led to higher redness values, decreased yellowness values, and increased K/S color yield values. The PNF sample coated with formulation X4, containing a lignin concentration of 4%, achieved the highest K/S value (7.45). When the wettability measurements results are evaluated according to the WCA values of the surfaces of coated and thermally cured PNFs, WCA values increased with the increasing lignin concentration in lignin/WPU composite coating pastes. The lowest WCA value of 26.2° was obtained with the lignin-free formulation X. On the other hand, the highest WCA value of 93.6° was obtained with the formulation X4 including 4% lignin. WCA values of the lignin/WPU coatings demonstrated a gradual increase as the concentration of lignin was elevated. Remarkably, the X coating without lignin also exhibited improved hydrophobic properties. These findings emphasize the noteworthy hydrophobic performance of the lignin/WPU coatings, largely stemming from the intrinsic qualities of lignin within the WPU formulation. SEM analysis revealed that the Lignin/WPU composite coating paste filled gaps between fibers on the PNF surface, resulting in a more uniform appearance. In the DSC analyzes, it was concluded that the use of lignin in varying concentrations in lignin/WPU composite formulations improved the thermal properties of the films compared to the film prepared with the lignin-free X formulation. According to the TGA analysis results in which the thermal stability of the composite formulations were analyzed; lignin/WPU films exhibited better thermal stability than the lignin-free X film. Initial decomposition and maximum decomposition temperatures of X4 film reached of 341.33°C and 446.51°C, respectively, and these values were obtained as 305.15°C and 419.13°C for the lignin-free X film. The increase in thermal stability is attributed to the cleavage of C–C bonds in the lignin structure and degradation of aromatic rings. Additionally, in TGA results, the weight loss for the X4 formulation decreased by 8% compared to the lignin-free X film. Comfort tests indicated that the air permeability of PNF, owing to its open porous structure, measured at 1287 l/m2/s. Coating with the X1 formulation yielded an air permeability of 290 l/m2/s, while the X4 formulation, containing 4% lignin, resulted in a measurement of 142 l/m2/s. The reduction in air permeability in fabrics coated with high lignin concentration formulations is attributed to the lignin/WPU structure filling the pores between fabric fibers, thus impeding air passage. Moreover, results of the antimicrobial activity demonstrated the efficacy of lignin/WPU coatings on PNFs against microorganisms such as S. aureus This study showed that lignin, a natural biodegradable polymer, can impart different functional properties to PNF fabrics. The findings of this study are anticipated to provide valuable insights into the development of sustainable and functional materials for various applications, contributing to the advancement of eco-friendly solutions in the textile industry.

Acknowledgement

The authors would like to express their gratitude to The Scientific and Technological Research Council of Türkiye (TUBITAK) for their financial support (project number 122M737). The author acknowledges the East Anatolia High Technology Application and Research Center of Atatürk University for FT-IR analysis and Water Contact Angles measurements, the Central Research Laboratory of Amasya University for conducting DSC and TGA analyses, and the Bursa Technology Coordination and R&D Center for air permeability measurements. Additionally, the author acknowledges to Central Research Laboratory Application and Research Center of Eskişehir Osmangazi University for SEM measurements.

References

1. Carfagna C, Persico P. Functional Textiles Based on Polymer Composites. Macromol Symp. 2006;245–246(1):355–62.
2. Wollina U, Heide M, Müller-Litz W, Obenauf D, Ash J. Functional Textiles in Prevention of Chronic Wounds, Wound Healing and Tissue Engineering. In: Textiles and the Skin. Basel: Karger; 2003. p. 82–97.
3. Gupta M, Sheikh J, Annu, Singh A. An eco-friendly route to develop cellulose-based multifunctional finished linen fabric using ZnO NPs and CS network. J Ind Eng Chem. 2021;97:383–9.
4. Muzaffar S, Abbas M, Siddiqua UH, Arshad M, Tufail A, Ahsan M, et al. Enhanced mechanical, UV protection and antimicrobial properties of cotton fabric employing nanochitosan and polyurethane based finishing. J Mater Res Technol. 2021;11:946–56.

5. Deng C, Seidi F, Yong Q, Jin X, Li C, Zhang X, et al. Antiviral/antibacterial biodegradable cellulose nonwovens as environmentally friendly and bioprotective materials with potential to minimize microplastic pollution. J Hazard Mater. 2022 Feb;424:127391.
6. Zhang Y, Li TT, Shiu BC, Sun F, Ren HT, Zhang X, et al. Eco-friendly versatile protective polyurethane/triclosan coated polylactic acid nonwovens for medical covers application. J Clean Prod. 2021;282:124455.
7. Pan LS, Yang Q, Xu N, Pang SJ, Wang SF. Preparation and characterization of biodegradable polylactic acid/polypropylene spun-bonded nonwoven fabric slices. Int Polym Process. 2018;33(5):634–41.
8. Chen T, Guo J, Xu H, Zhang J, Hu N, Liu H. One-step fabrication of biodegradable superhydrophobic PLA fabric for continuous oil/water separation. Appl Surf Sci. 2022 Feb;576:151766.
9. Raman A, Sankar A, Abhirami SD, Anilkumar A, Saritha A. Insights into the Sustainable Development of Lignin-Based Textiles for Functional Applications. Macromol Mater Eng. 2022;307(8):1–18.
10. Holme I. Innovative technologies for high performance textiles. Color Technol. 2007;123(2):59–73.
11. Morales-Jiménez M, Gouveia L, Yañez-Fernandez J, Castro-Muñoz J, Barragan-Huerta BE. Microalgae-Based Biopolymer as a Potential Bioactive Film. Coatings. 2020;10:120.
12. Dixit A, Sabnis A, Shetty A. Antimicrobial Edible Films and Coatings based on N,O-Carboxymethyl Chitosan incorporated with Ferula Asafoetida (Hing) and Adhatoda Vasica (Adulsa) extract. Adv Mater Process Technol. 2022;8(3):2699–715.
13. Dixit A, Sabnis A, Balgude D, Kale S, Gada A, Kudu B, et al. Synthesis and characterization of citric acid and itaconic acid-based two-pack polyurethane antimicrobial coatings. Polym Bull. 2023;80(2):2187–216.
14. Wang X, Zhang Y, Liang H, Zhou X, Fang C, Zhang C, et al. Synthesis and properties of castor oil-based waterborne polyurethane/sodium alginate composites with tunable properties. Carbohydr Polym. 2019 Mar; 208:391–7.
15. Zhang Y, Li TT, Lou CW, Lin JH. Facile method for tent fabrics with eco-friendly/durable properties using waterborne polyurethane/lignin: Preparation and evaluation. J Ind Text. 2022 Jun 13;51:4149S-4166S.
16. Wang H, Qiu X, Liu W, Fu F, Yang D. A novel Lignin/ZnO hybrid nanocomposite with excellent UVAbsorption ability and its application in transparent polyurethane coating. Ind Eng Chem Res. 2017;56(39):11133–41.
17. Hui Z, Haonan Z, Hao R, Huamin Z. Optimized preparation of spruce kraft lignin/ZnO composites and their performance analysis in polyurethane films. Int J Biol Macromol. 2022;209:1465–76.
18. Gaynor JG, Szlek DB, Kwon S, Tiller PS, Byington MS, Argyropoulos DS. Lignin use in nonwovens: A review. BioResources. 2022;17(2):3445–88.
19. Klapiszewski Ł, Grząbka-Zasadzińska A, Borysiak S, Jesionowski T. Preparation and characterization of polypropylene composites reinforced by functional ZnO/lignin hybrid materials. Polym Test. 2019;79:106058: 1-9.
20. Kaur R, Bhardwaj SK, Chandna S, Kim KH, Bhaumik J. Lignin-based metal oxide nanocomposites for UV protection applications: A review. J Clean Prod. 2021 Oct;317:128300.
21. Sunthornvarabhas J, Liengprayoon S, Lerksamran T. Utilization of Lignin Extracts from Sugarcane Bagasse as Bio-based Antimicrobial Fabrics. Sugar Tech. 2019;21(2):355–63.
22. Henn KA, Forsman N, Zou T, Österberg M. Colloidal Lignin Particles and Epoxies for Bio-Based, Durable, and Multiresistant Nanostructured Coatings. ACS Appl Mater Interfaces. 2021;13(29):34793–806.
23. Mishra RS, Mishra AK, Raju KVSN. Synthesis and property study of UV-curable hyperbranched polyurethane acrylate/ZnO hybrid coatings. Eur Polym J. 2009;45(3):960–66.
24. Li X, Chen X, Zhang S, Yin Y, Wang C. UV-resistant transparent lignin-based polyurethane elastomer with repeatable processing performance. Eur Polym J. 2021;159: 110763.
25. Zimniewska M, Kozłowski R, Batog J. Nanolignin Modified Linen Fabric as a Multifunctional Product. Mol Cryst Liq Cryst ISSN. 2008;1406(484):43/409-50/416.
26. Zimniewska M, Batog J, Bogacz E, Romanowska B. Functionalization of Natural Fibres Textiles by Improvement of Nanoparticles Fixation on Their Surface. J Fiber Bioeng Informatics Soc. 2012;5(3):321–39.
27. Sunthornvarabhas J, Liengprayoon S, Suwonsichon T. Industrial Crops & Products Antimicrobial kinetic activities of lignin from sugarcane bagasse for textile product. Ind Crop Prod. 2017 Dec;109:857–61.
28. Baysal G. Mechanical and UV protection performances of polylactic acid spunlace nonwoven fabrics coated by eco-friendly lignin / water-borne polyurethane composite coatings. J Text Inst. 2023;0(0):1–13.
29. Sun N, Di M, Liu Y. Lignin-containing polyurethane elastomers with enhanced mechanical properties via hydrogen bond interactions. Int J Biol Macromol. 2021 Aug;184:1–8.
30. Tian M, Hu X, Qu L, Zhu S, Sun Y, Han G. Versatile and ductile cotton fabric achieved via layer-by-layer self-assembly by consecutive adsorption of graphene doped PEDOT: PSS and chitosan. Carbon N Y. 2016;96:1166–74.
31. Shaban M, Mohamed F, Abdallah S. Production and Characterization of Superhydrophobic and Antibacterial Coated Fabrics Utilizing ZnO Nanocatalyst. Sci Rep. 2018;8(1):1–15.
32. Zhang H, Li K, Yao C, Gu J, Qin X. Preparation of zinc oxide loaded polyurethane/polysulfone composite nanofiber membrane and study on its waterproof and moisture permeability properties. Colloids Surfaces A Physicochem Eng Asp. 2021 Nov;629:127493.
33. Ye Z, Li S, Zhao S, Deng L, Zhang J, Dong A. Textile coatings configured by double-nanoparticles to optimally couple superhydrophobic and antibacterial properties. Chem Eng J. 2021;420(P2):127680.
34. Kudzin MH, Mrozińska Z. Biofunctionalization of Textile Materials. 2. Antimicrobial Modification of Poly(lactide) (PLA) Nonwoven Fabricsby Fosfomycin. Polymers (Basel). 2020 Apr 1;12(4):768.
35. Ng QY, Low JH, Pang MM, Idumah CI. Properties Enhancement of Waterborne Polyurethane Bio-composite Films with 3-aminopropyltriethoxy Silane Functionalized Lignin. J Polym Environ. 2022;688–97.

36. Li J, Wang B, Chen K, Tian X, Zeng J, Xu J, et al. The use of lignin as cross-linker for polyurethane foam for potential application in adsorbing materials. BioResources. 2017;12(4):8653–71.
37. Liu X, Gao C, Fu C, Xi Y, Fatehi P, Zhao JR, et al. Preparation and Performance of Lignin-Based Multifunctional Superhydrophobic Coating. Molecules. 2022;27(4):1440.
38. Šupová M, Martynková GS, Barabaszová K. Effect of nanofillers dispersion in polymer matrices: A review. Sci Adv Mater. 2011;3(1):1–25.
39. Wang W, Guo T, Sun K, Jin Y, Gu F, Xiao H. Lignin redistribution for enhancing barrier properties of cellulose-based materials. Polym. 2019;11(12):1929.
40. Ridho MR, Agustiany EA, Rahmi Dn M, Madyaratri EW, Ghozali M, Restu WK, et al. Lignin as Green Filler in Polymer Composites: Development Methods, Characteristics, and Potential Applications. Adv Mater Sci Eng. 2022 Apr; 363481.
41. Shankar S, Reddy JP, Rhim JW. Effect of lignin on water vapor barrier, mechanical, and structural properties of agar/lignin composite films. Int J Biol Macromol. 2015;81:267–73.
42. Lai Y, Qian Y, Yang D, Qiu X, Zhou M. Preparation and performance of lignin-based waterborne polyurethane emulsion. Ind. Cro. and Prod. 2021;170:113739.
43. Vieira FR, Magina S, Evtuguin D V., Barros-Timmons A. Lignin as a Renewable Building Block for Sustainable Polyurethanes. Materials (Basel). 2022 Sep 5;15(17):6182.
44. Zhang H, Fu S, Chen Y. Basic understanding of the color distinction of lignin and the proper selection of lignin in color-depended utilizations. Int J Biol Macromol. 2020;147:607–15.
45. Wang J, Deng, Y, Qian Y, Qiu X, Ren Y, Yang, D. Reduction of lignin color via one-step UV irradiation. Green Chem., 2016;18:695-99.
46. Leo CP, Cathie Lee WP, Ahmad AL, Mohammad AW. Polysulfone membranes blended with ZnO nanoparticles for reducing fouling by oleic acid. Sep Purif Technol. 2012;89:51–6.
47. Tyagi P, Gutierrez JN, Nathani V, Lucia LA, Rojas OJ, Hubbe MA, et al. Hydrothermal and mechanically generated hemp hurd nanofibers for sustainable barrier coatings/films. Ind Crops Prod. 2021 Sep;168:113582.
48. Pandya H, Mahanwar P. Fundamental insight into anionic aqueous polyurethane dispersions. Adv Ind Eng Polym Res. 2020;3(3):102–10.
49. Wu L, Liu S, Wang Q, Wang Y, Ji X, Yang G, et al. High strength and multifunctional polyurethane film incorporated with lignin nanoparticles. Ind Crops Prod. 2022;177:114526.
50. Zhang N, Liu P, Yi Y, Gibril ME, Wang S, Kong F. Application of polyvinyl acetate/lignin copolymer as bio-based coating material and its effects on paper properties. Coatings. 2021;11(2):1–12.
51. Lavrič G, Zamljen A, Grkman JJ, Jasiukaitytė-Grojzdek E, Grilc M, Likozar B, et al. Organosolv lignin barrier paper coatings from waste biomass resources. Polymers (Basel). 2021;13(24): 4443
52. Ng SF, Hui CL, Wong LF. Development of medical garments and apparel for the elderly and the disabled. Text Prog. 2011;43(4):235–85.
53. N. Gokarneshan, D.A. Rachel, V. Rajendran, B. Lavanya, A. Ghoshal, Surgical gowns - techno economic aspects and innovations, in: Emerging Research Trends in Medical Textiles. Springer, Singapore, 2015. p. 97–119.
54. Zhang Y, Li TT, Shiu BC, Sun F, Ren HT, Zhang XF, et al. Processing and characterizations of Short fluoroalkyl chain / polyurethane- polylactic acid/low melt polylactic acid Janus nonwoven Medical covers using spray coating. Prog Org Coat. 2020 May;147:105736.
55. Pakdel E, Daoud WA, Afrin T, Sun L, Wang X. Enhanced antimicrobial coating on cotton and its impact on UV protection and physical characteristics. Cellulose. 2017;24(9):4003–15.
56. Ullah I, Chen Z, Xie Y, Khan SS, Singh S, Yu C, et al. Recent advances in biological activities of lignin and emerging biomedical applications: A short review. Int J Biol Macromol. 2022 Mar;208:819–32.

HITTITE JOURNAL OF SCIENCE AND ENGINEERING

e-ISSN: 2148-4171
Volume: 11 • Number: 2
June 2024

Design of Image Processing-based System for Detection of Heat Transfer Direction in Thermoelectric Modules

Serkan Dişlitaş[1,*] | Özlem Altıok[2] | Murat Alparslan Güngör[2]

[1]Department of Computer Engineering, Hitit University, 19030, Çorum, Türkiye.
[2]Department of Electrical and Electronics Engineering, Hitit University, 19030, Çorum, Türkiye.

Corresponding Author

Serkan Dişlitaş
E-mail: serkandislitas@hitit.edu.tr Phone: +90 364 219 1200 Fax: +90 364 219 13 99
RORID[1,2]: https://ror.org/01x8m3269

Article Information

Article Type: Research Article
Doi: https://doi.org/10.17350/HJSE19030000335
Received: 08.09.2023
Accepted: 09.06.2024
Published: 30.06.2024

Cite As

Dişlitaş S, et al. Design of Image Processing-based System for Detection of Heat Transfer Direction in Thermoelectric Modules. Hittite J Sci Eng. 2024;11(2):89-94.

Peer Review: Evaluated by independent reviewers working in at least two different institutions appointed by the field editor.
Ethical Statement: Not available.
Plagiarism Checks: Yes - iThenticate
Conflict of Interest: Authors approve that to the best of their knowledge, there is not any conflict of interest or common interest with an institution/organization or a person that may affect the review process of the paper.

CRediT Author Statement:
Serkan Dişlitaş: Conceptualization, Software, Investigation, Writing - Review & Editing, Supervision. **Özlem Altıok:** Conceptualization, Investigation, Writing - Original Draft. **Murat Alparslan Güngör:** Conceptualization, Investigation, Writing - Review & Editing, Supervision.

Design of Image Processing-based System for Detection of Heat Transfer Direction in Thermoelectric Modules

Serkan Dişlitaş[1,*] |Özlem Altıok[2] |Murat Alparslan Güngör[2]

[1]Department of Computer Engineering, Hitit University, 19030, Çorum, Türkiye.
[2]Department of Electrical and Electronics Engineering, Hitit University, 19030, Çorum, Türkiye.

Abstract

It is extremely important for the performance and success of the system to know the cooling or heating surfaces of the thermoelectric modules (TEMs) as cooler or generator, according to the heat transfer direction, and to carry out their installation correctly, taking this into account. In TEMs, the direction of heat transfer between surfaces changes depending on the applied DC direction, and while one surface of the module cools, the other heats up. In this respect, the state of the positive and negative poles in the design and production of TEMs directly affects the heat transfer direction between the module surfaces. On the other hand, the contact direction of the surfaces of the TEMs used in a designed thermoelectric system (TES) is of great importance in order to perform the heat transfer correctly without loss of performance. In this study, a system is designed to detect the heat transfer direction of TEMs using image processing techniques. The basic principle of the system is to determine the positive and negative poles of the TEMs together with the ceramic plate, using the color-based image processing method, and to determine the heat transfer direction by utilizing their relative positions. With the designed system, the heat transfer direction of TEMs at different illuminance levels is tried to be determined and successful results were obtained. As a result, it is thought that the developed system will contribute to the automatic error control for the production and assembly of TEMs.

Keywords: Thermoelectric Module, Peltier Effect, Seebeck Effect, Heat Transfer, Image Processing, Software

INTRODUCTION

The popularity of thermoelectric modules (TEMs) is increasing, and their application areas are rapidly becoming widespread due to many advantages, such as being silent, vibration-free, long-lasting, and simple. Additionally, they have no moving parts, can operate in any direction, and require no maintenance (1). Various research efforts are underway to advance the design, production, testing, and application of TEMs in thermoelectric systems (2-6).

In general, it is desired that a thermoelectric system (TES) to be designed for cooling or power generation should have high heat transfer, low power consumption and at the same time economical. In practice, only a single TEM can be used according to the desired capacity in TES design, or several TEMs can be used by connecting each other in series, parallel or cascade. The number of TEMs needed and the connection type are determined by considering the electrical and thermal parameters of the TEMs used (1).

It is extremely important for the performance and success of the system to know the cooling or heating surfaces of the TEMs as coolers or generators according to the heat transfer direction, and to carry out their installation correctly considering this situation. Because, incorrect assembly of TEMs can cause TES to perform poorly or even to work completely incorrectly in cooling or electricity production, depending on the design purpose. Hence, it is very important not to make wrong placements and to correct them immediately. In this respect, first of all, it is necessary to determine the heating and cooling surfaces of the modules to be used in the design according to the DC polarization status.

In general, it is difficult to detect the heating and cooling surfaces of the TEMs due to their simple ceramic structure and the fact that both surfaces are exactly similar to each other. Incorrect surface use affects performance negatively, especially in systems where a large number of modules are used. Conventionally, the heating and cooling surfaces of a TEM are determined either by visually checking the status of the positive (red) and negative (black) poles or by controlling the temperature with DC voltage. In addition, some manufacturers indicate in writing on the heated surface of the TEM in the direct biasing. Detection procedures made in this way may prolong the process and cause errors.

Recently, computer vision applications have become widespread with the development of image processing algorithms and software technologies. Image processing systems are widely used in industrial areas for fast and accurate detection, tracking and classification of objects. Classification of objects based on image processing can be done using shape, motion, color and texture based methods (7). Color-based classification methods are widely used because of the high processing speed and success rate (8). Determining the position of an object detected in image processing algorithms on the image is based on the principle of finding the center of gravity (9).

In this study, a system is designed and the performance of the system is analyzed to determine the hot side, cold side and heat transfer direction of the TEMs, using color-based image processing techniques and based on the principle of finding the center of gravity.

MATERIAL AND METHODS

Heat Transfer in Thermoelectric Module

TEMs are devices consisting of N-type and P-type semiconductor thermocouples placed in a matrix array between two external plates, electrically connected to each other in series and thermally connected to each other in parallel. In addition, they can operate both in cooler mode according to the Peltier effect principle and in generator mode according to the Seebeck effect principle. Figure 1 shows a TEM general view and structure. TEMs operating on the DC principle have two connection terminals, one being the positive (red) pole and the other being the negative (black) pole (10, 11).

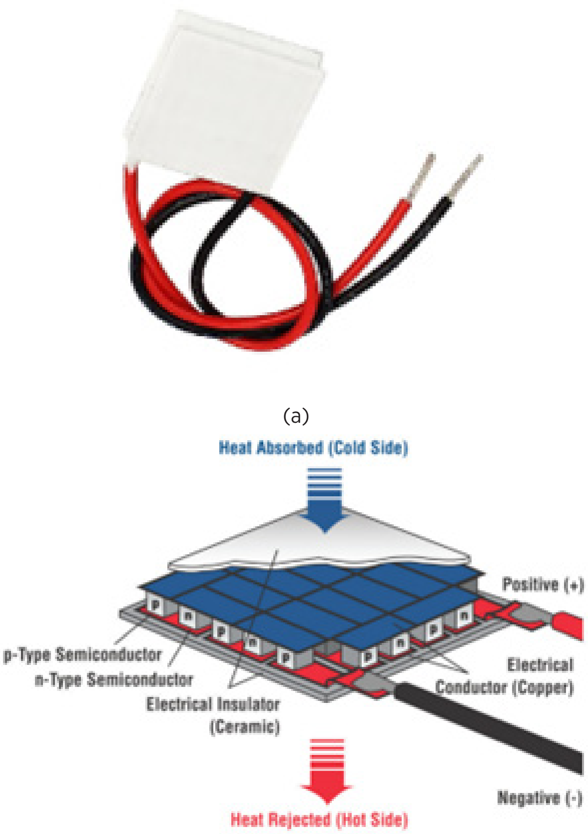

(a)

(b)

Figure 1 (a) General view and (b) structure of a TEM (11)

P-type and N-type thermoelectric semiconductors form the fundamental components of heat transfer within TEMs. Negative charge carriers (electrons) are the majority charge carriers in N-type semiconductors, and positive charge carriers (halls) in P-type semiconductors. Figure 2 shows the heat transfer direction for a TEM operating in cooling and generator mode. According to the Peltier effect principle, heat transfer occurs in the direction of electron flow and hall flow through charge carriers, depending on the DC current intensity and polarization applied in TEM. As a result of the heat transfer caused by the Peltier effect, one of the sides cools and the other heats up. In other words, with the Peltier effect, heat is transferred from the cold side to the hot side, and no heat is produced. On the other hand, according to the Seebeck effect principle, a DC current is produced by the charge carriers depending on the direction of the heat transfer that occurs as a result of the temperature difference created between the surfaces in the TEM (6, 12).

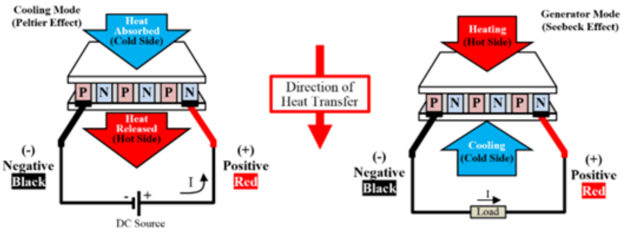

Figure 2 Direction of heat transfer in TEM

The direction of heat transfer in a TEM according to the direct and reverse biasing conditions is shown in Figure 3. TEMs generally has two connection terminals, positive (Red) and negative (black). The heat transfer direction changes depending on the positions of the positive and negative connection terminals relative to each other along with the ceramic body of the TEM. When the TEM is under direct biasing, with the positive (red) terminal positioned to the left and the negative (black) terminal to the right relative to the ceramic layer, heat transfer occurs from the lower side to the upper side. In this case, as the lower side cools, the upper side concurrently heats up. Conversely, when the TEM is direct biasing with the positive (red) terminal on the right and the negative (black) terminal on the left, the heat transfer direction reverses, flowing from the upper side to the lower side. In this scenario, while the upper side cools down, the lower side heats up. In the case of reverse biasing, heat transfer occurs opposite to that of direct biasing.

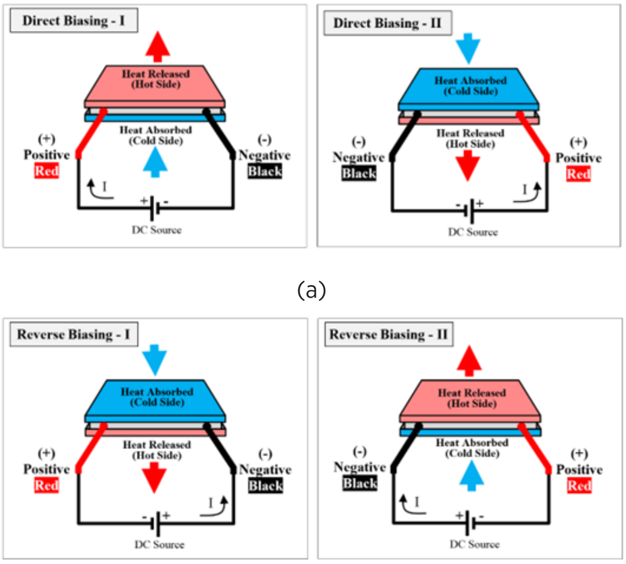

(a)

(b)

Figure 3 Direction of heat transfer in a TEM. (a) Direct biasing (b) Reverse biasing

Developed Software

The user interface of the image processing-based software developed for determining the TEM heat transfer direction is shown in Figure 4. The interface software for the operation of the system is coded in Python language and the OpenCV (Open Source Computer Vision Library) library is used for image processing, object detection and coordinate determination (9, 13).

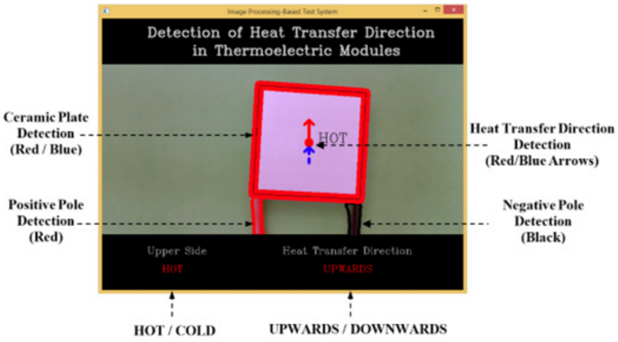

Figure 4 General overview of the software GUI

Figure 5 illustrates the 2-axis view and coordinate of a TEM. In terms of appearance, a TEM typically features a ceramic plate and two terminals distinguished by positive (red) and negative (black) poles. The points C(X,Y), P(X,Y) and N(X,Y) located in the XY plane with the origin point O(0,0) represent the centroids of the ceramic plate, the positive pole tip and the negative pole tip, respectively.

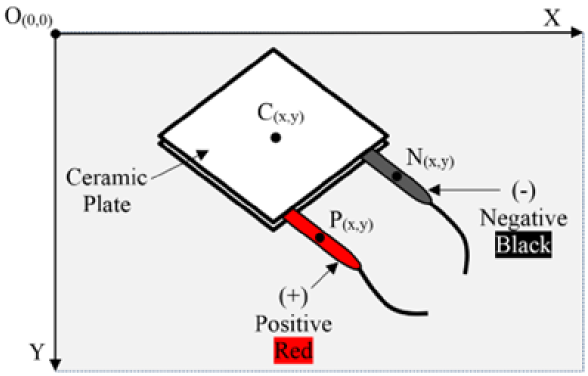

Figure 5 2-axis view and coordinate of a TEM

The flowchart for finding the hot surface, cold surface and heat transfer direction using color-based image processing in a TEM is shown in Figure 6. First of all, the positions of the positive and negative poles are determined together with the ceramic plate that forms the TEM, and the centroids C(x,y), P(x,y) and N(x,y) are determined. Mathematically, these calculations are made by calculating the zeroth and first moments from Equation 1 and the centroid from Equation 2 (14). In the next step, the position of the TEM is determined by substituting these centroids in Equation 3 and the hot side, cold side and heat transfer direction are determined.

$$M_{00} = \sum_x \sum_y I(x,y) \qquad M_{10} = \sum_x \sum_y x.I(x,y) \qquad M_{10} = \sum_x \sum_y y.I(x,y) \tag{1}$$

$$x_c = \frac{M_{10}}{M_{00}} \qquad y_c = \frac{M_{01}}{M_{00}} \tag{2}$$

$$(N_X \neq P_X) \Rightarrow \{ \begin{matrix} ((N_X - P_X) * ((N_Y + P_Y)/2 - C_Y)) < 0, & "COLD" \\ \text{otherwise,} & "HOT" \end{matrix}$$

$$(N_X = P_X) \Rightarrow \{ \begin{matrix} ((N_Y - P_Y) * ((N_X + P_X)/2 - C_X)) < 0, & "COLD" \\ \text{otherwise,} & "HOT" \end{matrix} \tag{3}$$

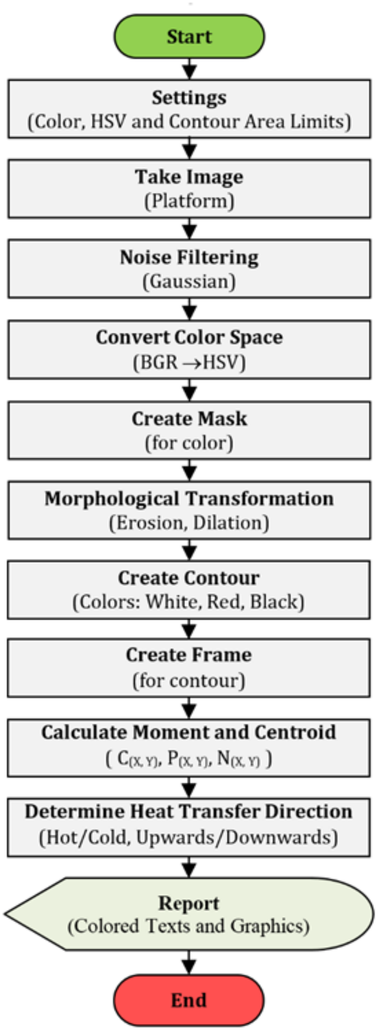

Figure 6 Flowchart for finding the heat transfer direction in TEM

When the algorithm is run, firstly colors, Hue - Saturation - Value (HSV) color space lower and upper limit values and minimum area size settings for detection are made (15, 16). HSV color space model lower and upper limit ranges for TEM colors used in the designed system are shown in Table 1. After the initial settings, an image is taken with the help of the camera and immediately Gaussian Blur filtering with size 11x11 is performed to eliminate details and noise in the image. In OpenCV image processing applications, instead of the RGB color format, the BGR (Blue-Green-Red) color format is used (9). However, since it gives better results for the detection of colored objects in image processing applications, the image is converted from BGR color space to HSV color space (17). Masking is done depending on the defined colors and their ranges. In the Morphological Transform stage, the image is rearranged by edge erosion and dilation to remove noise from the image. In this stage, a 3x3 rectangular structuring element is used by applying the erosion and dilation operating two times consecutively. A contour is created to increase the distinguishability of the detected colored regions. For each contour that provides the minimum area size for detection, a frame is first drawn and with the help of moment calculations, the centroids are found and the C(X,Y), P(X,Y) and N(X,Y) coordinates for the 2-axis are determined. In the last stage of the algorithm, the heat transfer direction is determined by using these centroids. Colorful representations with written and graphic support are made in the GUI for the results obtained. The heat transfer direction is stated in writing as Upwards/Downwards and is also shown with an arrow sign. In addition, the upper side of the TEM is colored as Blue for cold and Red for hot.

Table 1 Color ranges of the HSV color space model for TEM colors in the designed system

Reference Color	Lower Limit (H, S, V)	Upper Limit (H, S, V)
Black	(0, 0, 0)	(179, 255, 90)
White	(0, 0, 200)	(172, 111, 255)
Red	(160, 100, 100)	(179, 255, 255)

RESULTS AND DISCUSSION

In order to determine the performance of the developed software, an experimental setup is designed (Figure 7). Here, the LX-1330B model digital luxmeter is used to externally measure the illuminance level for the platform. In the experimental study, in order to obtain the colors properly, the illumination is made with white light. Within the scope of the study, the system is covered with a black fabric cover in order to eliminate the effects of the external environment.

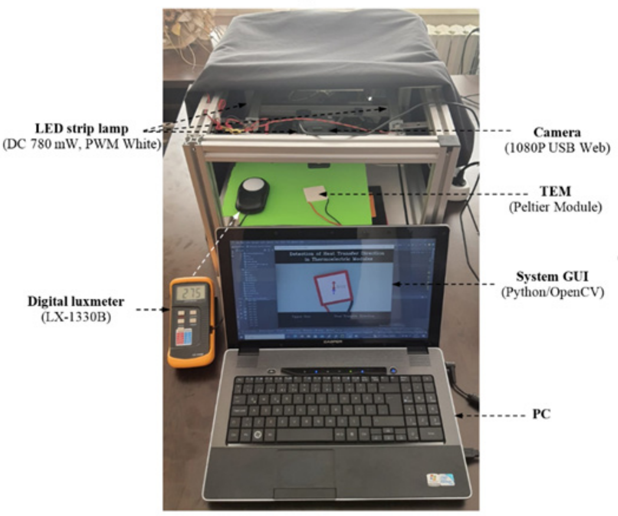

Figure 7 General view of the experimental setup

The performance of the image processing-based software developed in the study is examined at different illuminance levels. For this purpose, computer-controlled Pulse Width Modulation (PWM) based LED lighting is used in the setup to obtain illuminance levels in the range of 0-100 lx in the environment. First of all, the minimum illuminance levels required for different colors in TEM for color-based image processing in the system are investigated. The Minimum Illuminance (E_{min}) values required for successful color-based image processing for TEM in the system are determined as 13 lx for red color, 26 lx for white color and 40 lx for black color (Figure 8).

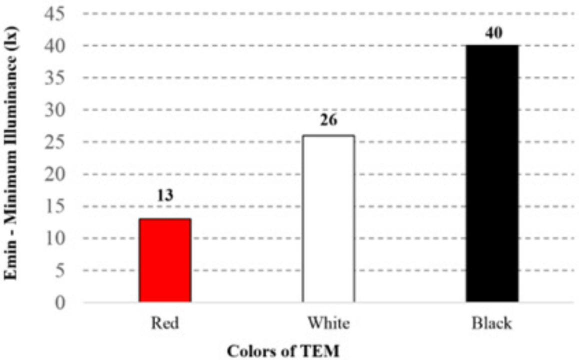

Figure 8 Minimum illumination levels required for different colors in TEM for color-based image processing

The graph given in Figure 9 shows the change in the success rate depending on the ambient illumination level in determining the heat transfer direction in TEM based on image processing. According to the results obtained, it is observed that heat transfer detection in the system is performed successfully when the illuminance level was above 40 lx, but could not be performed below 10 lx. Partially successful results are obtained at illumination levels between 10 lx and 40 lx. Figure 10 shows different GUI screenshots for successful and unsuccessful efforts to determine the heat transfer direction in the system. As can be seen from Figure 9 and Figure 10, when sufficient illumination level is provided, the system TEM can successfully detect the heat transfer direction.

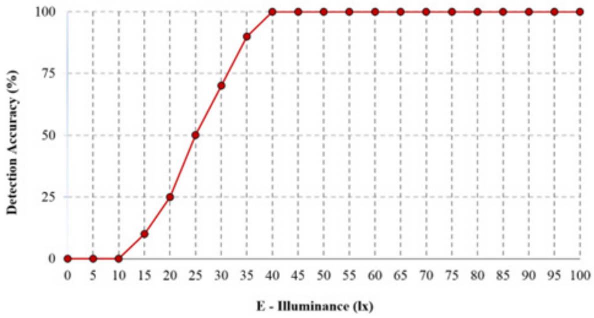

Figure 9 Change in detection accuracy according to ambient brightness level in determining the heat transfer direction based on image processing in TEM

CONCLUSION

In this study, a software-based system is designed to automatically detect the hot side, cold side and heat transfer direction of TEMs in the correct polarization, using color-based image processing techniques and based on the principle of finding the center of gravity. With the developed system, the direction of TEM heat transfer can be successfully determined even at low light levels, except when there is no object within the HSV color ranges of the TEM's ceramic surface or cables in the camera's field of view. In conclusion, it is thought that the developed system will contribute to automatic error control for the production and assembly of TEMs.

In future studies, the thermal and electrical performance of

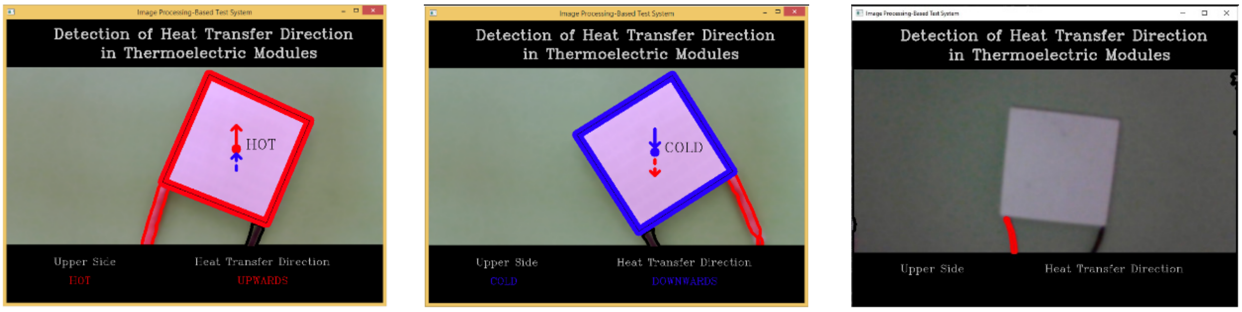

(a) (b) (b)

Figure 10 Different GUI screenshots for studies on determining the heat transfer direction in the system (a) detection successful: upwards (b) detection successful: downwards (c) detection unsuccessful

the TE system can be calculated instantly by determining the serial or parallel placement of thermoelectric modules by image processing method and taking into account basic parametric values.

Acknowledgment

The author received no financial support for the research, authorship, and/or publication of this article.

References

1. Ahıska R, Dişlitaş S. Computer controlled test system for measuring the parameters of the real thermoelectric module. Energy Conversion and Management 2011; 52: 27-36.
2. Harman TC. Special techniques for measurement of thermoelectric properties. J. Appl. Phys. 1958; 29:1373-1379.
3. Rowe DM, Marlow R, Burke E. CRC handbooks of thermoelectrics. Boca Raton; 1995.
4. Riffat SB, Ma X. Thermoelectrics: a review of present and potential applications. Appl. Thermal Eng. 2003; 23:913-935.
5. Dişlitaş S, Ahıska R. Üç ayrık ölçüme dayalı parabol algoritması ile termoelektrik modülün Imax, Vmax ve Emax parametrelerinin belirlenmesi. Gazi Üniversitesi Mühendislik Mimarlık Fakültesi Dergisi 2016; 31(4):1063-1072.
6. Dişlitaş S, Ömer G, Ahıska R. Microcontroller-based test system for determining the P-N type and Seebeck coefficient of the thermoelectric Semiconductors. Measurement 2019; 139:361-369.
7. Tiwari M, Singhai R. A Review of Detection and Tracking of Object from Image and Video Sequences. International Journal of Computational Intelligence Research 2017; 13(5):745-765.
8. Fan L, Wang Z, Cail B, Tao C. A Survey on Multiple Object Tracking Algorithm. Proceedings of the IEEE International Conference on Information and Automation 2016; 1855-1862.
9. Minichino J, Howse J. Learning OpenCV 3 Computer Vision with Python (Second Edition), Packt Publishing, Birmingham-Mumbai; 2015.
10. Rowe D (Ed.). Thermoelectrics Handbook: Macro to Nano (third ed.), CRC Press; 2006.
11. Laird Thermal Systems. Thermoelectric Modules. (https://lairdthermal.com/products/thermoelectric-cooler-modules. Last Retrieved March 12, 2023).
12. Pollock DD. Thermoelectric Phenomena, Editor: D.M. Rowe, CRC handbook of thermoelectrics, FL, USA: CRC Press; 1995:21-31.
13. OpenCV Reference Guide. (https://docs.opencv.org/4.7.0/, Last Retrieved: Feb 15, 2023).
14. Salhi A, Jammoussi AY. Object tracking system using Camshift, Meanshift and Kalman Filter. World Academy of Science, Engineering and Technology 2012; 6 (4):1-6.
15. Hema D, Kannan S. Interactive Color Image Segmentation using HSV Color Space. Science and Technology Journal 2019;7(1):37-41.
16. Manipriya S, Mala C, Mathew S. Performance Analysis of Spatial Color Information for Object Detection Using Background Subtraction. IERI Procedia 2014; 10:63-69.
17. Chena Y, Xiaoa X, Liub H, Fenga P. Dynamic color image resolution compensation under low light. Optik 2015;126:603-608.

HİTİT
UNIVERSITY
PRESS